CHAPTER 3

Computational Modelling of MOF Mechanics: From Elastic Behaviour to Phase Transformations

SVEN M. J. ROGGE*[a]

[a]Center for Molecular Modeling, Ghent University, Technologiepark-Zwijnaarde 46, 9052 Zwijnaarde, Belgium
*E-mail: Sven.Rogge@UGent.be

3.1 Introduction

The structure of metal–organic frameworks (MOFs) is governed by an intricate interplay of disparate interactions, from weak dispersion forces to strong covalent bonds, and from isotropic to strongly directional interactions. This gives rise to several attractive but often poorly understood mechanical phenomena in these 'soft' solid-state materials, including negative linear compressibility (NLC),[1] negative thermal expansion (NTE),[2] extreme anisotropy that may even lead to a negative Poisson's ratio or auxetic behaviour (Chapter 2), and a wide variety of both displacive and reconstructive phase transitions induced by mechanical stress or other external stimuli including gas sorption and temperature, among others.[3,4] Furthermore, the experimentally observed macroscopic response of MOFs to external stimuli is not only defined by this intrinsic interplay of interactions at the atomic, microscopic level, but is also impacted by effects occurring on larger length scales that

Inorganic Materials Series No. 12
Mechanical Behaviour of Metal–Organic Framework Materials
Edited by Jin-Chong Tan

Published by the Royal Society of Chemistry, www.rsc.org

may supersede this intrinsic response. Examples of such long-range effects include the interplay between different types of structural disorder,[4,5] the impact of crystallite size and morphology,[6] interactions occurring between different MOF crystals present in a macroscopic sample, and interactions between the MOF and the experimental probe interrogating its mechanical behaviour.[7] Therefore, isolating and understanding the salient features that define the macroscopic mechanical behaviour of a MOF is not only inspired by a fundamental scientific curiosity, but is also vital to enable the design of MOFs with predefined macroscopic functionalities not encountered in other materials.

Computational MOF research plays an important role in this respect, especially when adopted in close feedback with experimental research. Given the relative compliance of MOFs to external stimuli, the aforementioned complexity in different interactions at the microscopic level, and the hierarchical and multiscale nature of interactions from the unit cell level to the macroscopic MOF material, it is clear that the applicability of any given modelling tool strongly depends on the specific question at hand. Furthermore, since anomalous mechanical behaviour is encountered much more frequently in MOFs than in other solid-state materials, modelling techniques that are deemed firmly established in solid-state computational research may be too inaccurate to be used in MOF research. As a result, the advent of MOFs also necessitated – and continues to necessitate – the development of fundamentally new *in silico* techniques, as well as the adaptation of established techniques, to account for their soft behaviour. In this respect, computational MOF research is located at the exciting intersection where newly developed modelling tools are put to a stringent test to reproduce the mechanical behaviour of experimentally characterised MOFs on the one hand, and where newly observed anomalous behaviour in MOFs (Chapter 2) forms an impetus to develop new computational techniques on the other.

In Chapter 3, we shall critically review the computational tools that are being developed and used to model MOF mechanics. An extensive list of literature examples is provided to discuss each of these methods, focussing on the computational parameters affecting their accuracy, their scope of applicability and limitations, and how they compare to alternative techniques. This discussion is divided into techniques that probe the equilibrium or elastic behaviour of MOFs in Section 3.4 and techniques that model phase transitions or the plastic behaviour of MOFs, discussed in Sections 3.5 and 3.6 for single-crystal-to-single-crystal transitions and single-crystal-to-amorphous transitions, respectively. While these sections also briefly summarise the theoretical cornerstones on which these techniques are built, a more elaborate theoretical underpinning of how to model the mechanical behaviour of MOFs, which transcends the specific techniques discussed in the second half of this chapter, is provided in Sections 3.2 and 3.3. Section 3.2 focuses on how to identify mechanical properties, which are mostly taught from a macroscopic continuum point of view, with an atomistic view of MOFs. Section 3.3 discusses the ingredients needed to extract mechanical properties from computational MOF simulations as accurately as possible. The chapter

closes in Section 3.7 with a personal outlook on the critical challenges that computational MOF research needs to overcome to further advance the research field, and provide a holistic and multiscale approach to predict the mechanical performance of MOFs.

3.2 From a Continuum to an Atomic Description of Stress and Strain

Variables such as the Cauchy stress or constitutive relations such as Hooke's law are ubiquitously used in computational MOF research, although they find their origin in continuum theory.[8] In continuum mechanics, a macroscopic body is regarded as an assembly of continuum particles or voxels such that the state variables that define the mechanics of this body – such as stress and strain – vary smoothly over adjacent particles and are governed by macroscopic continuum field equations.[8] While continuum particles need to be infinitesimally small from a macroscopic point of view, the state variables associated with such a continuum particle are still derived from a finite microscopic region surrounding the location of the particle to ensure this smoothness.[8] This contrasts with the typical atomistic viewpoint of materials adopted in computational MOF research, in which for instance the mass density fluctuates wildly between nonzero values for locations where nuclei are present and zero values elsewhere. To reconcile these two points of view, the length scale of continuum particles – and hence the length scale on which state variables such as Cauchy stress are defined – should be much smaller than the length scale on which variations in the continuum fields occur and, simultaneously, much larger than typical atomic length scales to ensure the smooth behaviour over adjacent continuum particles.[8]

While continuum mechanics does not make any assumptions on the underlying atomistic framework of the material, one may ask how these phenomenological continuum equations are governed by the particles constituting the material and their interactions. This would allow one not only to define these phenomenological parameters, such as the stiffness tensor or the point at which a material deforms irreversibly, from a quantum mechanical point of view, but also to draw casual relations between the atomic structure of a MOF and its mechanical properties and hence accelerate the discovery of exciting anomalous behaviour in tuneable functional materials such as MOFs.

Such a statistical mechanics picture of continuum theory was pioneered by Irving and Kirkwood in 1950, when they proposed atomic expressions for continuum properties including the stress tensor and the heat current density.[9] In order for these properties to be true atomistic descriptions of the material consistent with the continuum variables defined earlier, these so-defined point functions should satisfy two requirements:

1. When properly averaged over space (over the continuum particle length scale defined earlier on) and time, the atomistic definitions should coincide with the continuum definitions;

2. The atomistic definitions should satisfy the same hydrodynamical equations – continuity equation, equation of motion, and equation of energy transport – as the continuum variables. This also implies that, for instance, an elasticity tensor defined at the atomic scale can be interpreted as a local equivalent of an elasticity tensor defined for a macroscopic body, forming a bridge between atomic and continuum theories.

In this section, this consistent approach will be adopted to derive atomic-level definitions of strain and stress. While one could, alternatively, simply postulate these definitions, this explicit derivation will help the further discussion in two ways. First, it will unveil the different approximations when defining stress and strain at the atomic level and hence help to understand under which inherent limitations the mechanical properties of MOFs can be simulated. Second, this discussion provides the ingredients necessary to computationally simulate MOFs under constant pressure or stress in Section 3.3.3.

Let us begin by considering a conservative atomic system of N particles and a right-handed Cartesian frame of reference with basis vectors $(\boldsymbol{e}_1,\boldsymbol{e}_2,\boldsymbol{e}_3)$, as depicted in Figure 3.1. With respect to this reference frame, the system is defined by the positions of its N particles $\boldsymbol{r}_i = x_i\boldsymbol{e}_1 + y_i\boldsymbol{e}_2 + z_i\boldsymbol{e}_3$, $i \in [1,N]$ and their momenta $\boldsymbol{p}_i$. To simplify the notation, define the $3N$-component vectors $\boldsymbol{r}^N = (x_1,y_1,z_1,x_2,y_2,z_2,\ldots,x_N,y_N,z_N)$ and $\boldsymbol{p}^N = (p_{1x},p_{1y},p_{1z},p_{2x},p_{2y},p_{2z},\ldots,p_{Nx},p_{Ny},p_{Nz})$. An alternative way to describe the positions of these atoms is by defining them with respect to a right-handed set of vectors $(\boldsymbol{a}_1,\boldsymbol{a}_2,\boldsymbol{a}_3)$ that forms a parallelepiped $\left(\boldsymbol{a}_i = \sum a_{ij}\boldsymbol{e}_j\right)$. Note that, in contrast to the basis vectors defined before, the vectors $\boldsymbol{a}_i$ do not need to be orthogonal nor normalised, although

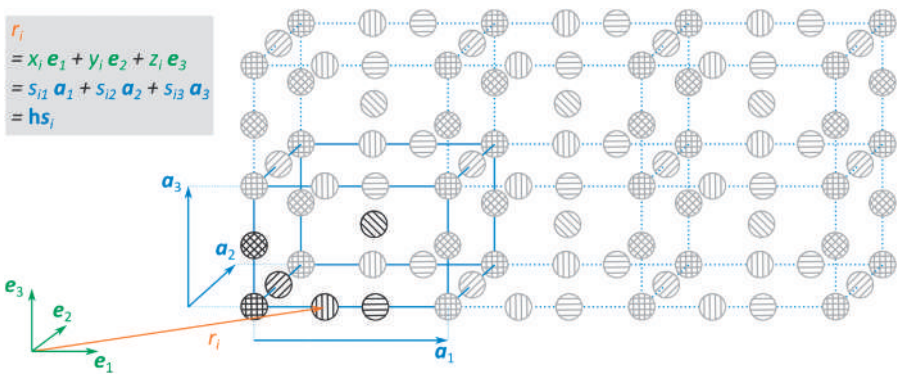

Figure 3.1 Schematic illustration of a crystalline material for which a unit cell $\mathbf{h} = [\boldsymbol{a}_1\ \boldsymbol{a}_2\ \boldsymbol{a}_3]$ (blue parallelepiped) containing six atoms can be defined. The material can then be described by a periodic repetition of this unit cell (five additional repetitions are shown in grey). Each atom can be defined either with respect to a Cartesian basis (in green) or in fractional coordinates, with respect to the unit cell vectors (in blue).

they do need to form a linearly independent set. These vectors can be collected in the 3 × 3 matrix **h** in which these vectors appear as the columns (observe that **h** is *not* a tensor):

$$\mathbf{h} = \begin{bmatrix} \boldsymbol{a}_1 & \boldsymbol{a}_2 & \boldsymbol{a}_3 \end{bmatrix} = \begin{bmatrix} a_{11} & a_{21} & a_{31} \\ a_{12} & a_{22} & a_{32} \\ a_{13} & a_{23} & a_{33} \end{bmatrix}. \tag{3.1}$$

Note that both matrices and tensors of rank two or higher will be denoted by bold-faced upright symbols. For (nearly) crystalline materials such as MOFs, the vectors $\boldsymbol{a}_i$ are often defined such that **h** defines the simulation cell matrix which is periodically repeated in space to mimic bulk conditions, as shown in Figure 3.1 and as discussed more extensively in Section 3.3.1. However, one could also define them based on the external surfaces of finite MOF crystallites in nonperiodic simulations. With respect to **h**, the atomic positions can be defined in fractional coordinates $\boldsymbol{s}_i$, such that $\boldsymbol{r}_i = s_{i1}\boldsymbol{a}_1 + s_{i2}\boldsymbol{a}_2 + s_{i3}\boldsymbol{a}_3$, $i \in [1,N]$ or, in matrix notation, $\boldsymbol{r}_i = \mathbf{h}\boldsymbol{s}_i$. Furthermore, we will assume that the atoms interact with one another through a potential energy function that only depends on the positions of these atoms: $\mathcal{V} = \mathcal{V}(\boldsymbol{r}^N)$. This potential energy forms a surface in the $3N$-dimensional configuration space, the construction of which will be further discussed in Section 3.3.2. Equipped with these definitions, it is now possible to proceed to atomistic definitions of strain and stress.

3.2.1 The Atomic Definition of Deformation Gradient and Strain

As in the continuum definition, atomic-level strain requires a reference or undeformed state against which a deformation is defined. Herein, properties of this reference state will be denoted by a subscript '0' symbol. Hence, the positions, fractional coordinates, and cell matrix of the reference state will be indicated by $\boldsymbol{r}_0^N$, $\boldsymbol{s}_0^N$, and $\mathbf{h}_0$, respectively, as illustrated in Figure 3.2(a).

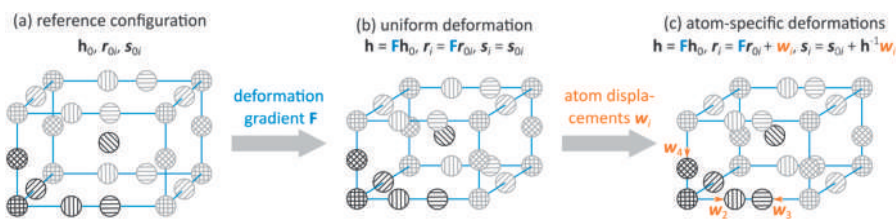

Figure 3.2 A general deformation of a crystal with respect to a reference configuration (a) can be divided into a uniform deformation (b), defined by the deformation gradient (in blue), and atom-specific deformations (c, in orange).

Following Cauchy and Born,[10–12] suppose that the material under study deforms to the state defined by $\boldsymbol{r}^N$, $\boldsymbol{s}^N$, and $\mathbf{h}$, shown in Figure 3.2(c). If the atoms would be deformed uniformly, as shown in Figure 3.2(b), the fractional coordinates in the deformed configuration would remain unchanged with respect to their values in the reference state, $\boldsymbol{s}_{0i} = \mathbf{h}_0^{-1}\boldsymbol{r}_{0i}$, where $\mathbf{h}^{-1}$ is the matrix inverse of $\mathbf{h}$. Hence, under a uniform deformation, the positions of the particle are given by $\boldsymbol{r}_i = \mathbf{h}\mathbf{h}_0^{-1}\boldsymbol{r}_{0i}$. This motivates the identification of $\mathbf{h}\mathbf{h}_0^{-1}$ as the atomic definition of the continuum deformation gradient $\mathbf{F}$:

$$\mathbf{F} = \mathbf{h}\mathbf{h}_0^{-1}. \tag{3.2}$$

Note that this definition ensures that $\mathbf{F}$ is a second-rank tensor, even though $\mathbf{h}$ is not.

A general deformation will not be completely uniform over the cell matrix. For quasi-uniform deformations, this departure from a uniform deformation is defined by the atomic displacement vectors $\boldsymbol{w}_i$, such that $\boldsymbol{r}_i = \mathbf{F}\boldsymbol{r}_{0i} + \boldsymbol{w}_i = \mathbf{h}\mathbf{h}_0^{-1}\boldsymbol{r}_{0i} + \boldsymbol{w}_i$, as shown in Figure 3.2(c).[8] When following the system through time, for instance in a molecular dynamics simulation, this property is time dependent:

$$\boldsymbol{r}_i(t) = \mathbf{F}(t)\boldsymbol{r}_{0i} + \boldsymbol{w}_i(t) = \mathbf{h}(t)\mathbf{h}_0^{-1}\boldsymbol{r}_{0i} + \boldsymbol{w}_i(t). \tag{3.3}$$

This so-called Cauchy–Born rule was originally derived to relate the mean positions of a deformed lattice to its undeformed reference state under a homogeneous deformation; but it has since been extended to also describe noncrystalline structures. Importantly, in the formulation given above, a quasiuniform deformation of $\mathbf{h}_0$ is assumed, which limits the field of applicability of eqn (3.3) to a region around the undeformed state, the extent of which is, inconveniently, *a priori* unknown.[8] As a result, the Cauchy–Born rule has been shown to no longer hold under phase transformations, either displacive or reconstructive, among other limitations.[13] When studying large-amplitude responses in MOFs, care should therefore be exerted to establish a proper reference state to define the deformation gradient of eqn (3.3). Taking MIL-53(Al) as a textbook example,[14] it cannot be expected that both the large-pore (lp) and closed-pore (cp) states of this material can be described by the same reference cell. When discussing a simulation protocol to probe MOFs under a constant external stress in Section 3.3.3, this statement will be further refined through the introduction of an adaptive modelling scheme. For a more in-depth discussion on the limitations and extensions of this approach, the interested reader is referred to Section 11.2 in ref. 8 and references therein.

From the atomic definition of the deformation gradient in eqn (3.1), one can define the Lagrangian strain $\boldsymbol{\eta}$, in the same fashion as in continuum mechanics:

$$\boldsymbol{\eta} = \frac{1}{2}\left(\mathbf{F}^T\mathbf{F} - \mathbf{I}\right) = \frac{1}{2}\left(\mathbf{h}_0^{-T}\mathbf{h}^T\mathbf{h}\mathbf{h}_0^{-1} - \mathbf{I}\right), \tag{3.4}$$

which coincides with the definition by Ray and Rahman.[15] Herein, **I** is the second-rank unit tensor, and $\mathbf{a}^{-T} = (\mathbf{a}^{-1})^T = (\mathbf{a}^T)^{-1}$, with T denoting a matrix transposition. Similarly, the Eulerian strain,[†] $\boldsymbol{\varepsilon}^{\text{eul}}$, is given by

$$\boldsymbol{\varepsilon}^{\text{eul}} = \frac{1}{2}\left(\mathbf{I} - \mathbf{F}^{-T}\mathbf{F}^{-1}\right) = \frac{1}{2}\left(\mathbf{I} - \mathbf{h}^{-T}\mathbf{h}_0^T\mathbf{h}_0\mathbf{h}^{-1}\right). \tag{3.5}$$

3.2.2 The Atomic Definition of Stress

Deriving an atomic equivalent to the continuum stress tensors is slightly more intricate. An intuitive derivation, based on ref. 8, starts from the thermodynamic observation that an N-atom system strained by a deformation gradient **F** and under temperature and stress control is described by the Gibbs free energy (or free enthalpy) G:[16]

$$G(N, \mathbf{P}, T; \mathbf{F}) = F(N, T; \mathbf{F}) - V_0\mathbf{P}{:}\mathbf{F}. \tag{3.6}$$

In this expression, T is the absolute temperature, $V_0 = \det(\mathbf{h}_0)$ is the volume of the cell matrix $\mathbf{h}_0$ describing the undeformed system, **P** is the first Piola–Kirchhoff stress tensor, and F is the Helmholtz free energy that describes the system under constant deformation and temperature. Furthermore, **P**:**F** denotes the tensor contraction of the two second-rank tensors **P** and **F**, such that $\mathbf{P} : \mathbf{F} = \sum_{i=1}^{3}\sum_{j=1}^{3} P_{ij}F_{ij}$.[‡] The Gibbs free energy reveals the (meta)stable states of the system under temperature and stress control as those states for which the derivative of the Gibbs free energy with respect to the deformation gradient vanishes:

$$\frac{\partial G(N,\mathbf{P},T;\mathbf{F})}{\partial \mathbf{F}} = \mathbf{0} \Leftrightarrow \frac{\partial F(N,T;\mathbf{F})}{\partial \mathbf{F}} - \mathbf{P}V_0 = \mathbf{0} \Leftrightarrow \mathbf{P}(T;\mathbf{F}) = \frac{1}{V_0}\frac{\partial F(N,T;\mathbf{F})}{\partial \mathbf{F}}. \tag{3.7}$$

Note that eqn (3.7) defines a tensor equality, which needs to hold for all nine components of **F**. Obtaining an atomic definition of the stress tensor

[†]These two different definitions for the same 'strain' property find their origin in the different ways one can look at continuum deformations: the material or the spatial perspective. In the materials perspective, properties are assigned to a material point, which moves through space upon deforming the material. In the spatial perspective, properties are assigned to a fixed point in space, irrespective of the material deformation. These two points of view give rise to the Lagrangian and the Eulerian strains as defined in eqn (3.4) and (3.5) respectively. Herein, we will adopt the material point of view when discussing materials properties and hence use the Lagrangian strain as the correct strain descriptor.

[‡]A similar description for the Gibbs free energy can be obtained by considering the finite Lagrangian strain **η**, defined in eqn (3.4), as independent variable in eqn (3.6) instead of the deformation gradient **F**. In that case, the second term in the right-hand side of eqn (3.6) equals $-V_0\mathbf{S}{:}\boldsymbol{\eta}$ instead of $-V_0\mathbf{P}{:}\mathbf{F}$, with **S** being the second Piola–Kirchhoff stress tensor, also denoted (the negative of) the thermodynamic tension.[15] In addition, it should be noted that the existence of a Gibbs free energy as a thermodynamic potential under a general deformation has been questioned, in contrast to the universally accepted definition of free energy under a hydrostatic pressure.[253]

P near equilibrium thus boils down to finding an atomic definition of the Helmholtz free energy F, which is possible through the partition function Z of this system:

$$F(N,T;\mathbf{F}) = -k_\mathrm{B}T\ln Z_{N\mathbf{F}T} = -k_\mathrm{B}T\ln\left[\frac{1}{N!h^{3N}}\int_{\Gamma(\mathbf{F})}\exp\left(\frac{-\mathcal{H}\left(\boldsymbol{r}^N,\boldsymbol{p}^N\right)}{k_\mathrm{B}T}\right)\mathrm{d}\boldsymbol{r}^N\mathrm{d}\boldsymbol{p}^N\right]. \tag{3.8}$$

Herein, k_B is Boltzmann's constant, h is Planck's constant,

$$\mathcal{H}\left(\boldsymbol{r}^N,\boldsymbol{p}^N\right) = \sum_{i=1}^{N}\frac{\boldsymbol{p}_i\cdot\boldsymbol{p}_i}{2m_i} + \mathcal{V}\left(\boldsymbol{r}^N\right) \tag{3.9}$$

is the Hamiltonian describing the system, $\Gamma(\mathbf{F})$ describes the subregion of the $6N$-dimensional phase space spanned by $\boldsymbol{r}^N$ and $\boldsymbol{p}^N$ that is accessible under the given deformation gradient, and m_i is the mass of particle i. In this equation, $\boldsymbol{p}_i\cdot\boldsymbol{p}_i$ denotes the scalar product of two vectors: $\boldsymbol{a}\cdot\boldsymbol{b} = \sum_{i=1}^{3}a_ib_i$. The **F**-dependence in the integration boundaries of eqn (3.8) arises as the deformation gradient is defined based on the matrix **h** and hence restricts the positions where the atoms can be located. However, its presence complicates taking the derivative of eqn (3.8) with respect to **F**. To move the **F**-dependence of eqn (3.8) to the integrand of the partition function, Ray and Rahman proposed a canonical transformation of the Hamiltonian using the generating function[15]

$$G\left(\boldsymbol{p}^N,\boldsymbol{r}_0^N\right) = -\sum_{i=1}^{N}\boldsymbol{p}_i\cdot\left(\mathbf{F}\boldsymbol{r}_{i,0}\right), \tag{3.10}$$

in which the subscript '0', as usual, indicates properties of the system in its undeformed configuration. Eqn (3.10) generates the canonical transformation

$$\boldsymbol{r}_i = \mathbf{F}\boldsymbol{r}_{i,0}\;\boldsymbol{p}_{i,0} = \mathbf{F}^T\boldsymbol{p}_i \tag{3.11}$$

and leaves the form of the Hamiltonian invariant, such that

$$\mathcal{H}_0\left(\boldsymbol{r}_0^N,\boldsymbol{p}_0^N,\mathbf{F}\right) = \mathcal{H}\left(\boldsymbol{r}^N\left(\boldsymbol{r}_0^N,\mathbf{F}\right),\boldsymbol{p}^N\left(\boldsymbol{p}_0^N,\mathbf{F}\right)\right) = \sum_{i=1}^{N}\frac{\left(\mathbf{F}^{-T}\boldsymbol{p}_{i,0}\right)\cdot\left(\mathbf{F}^{-T}\boldsymbol{p}_{i,0}\right)}{2m_i} + \mathcal{V}\left(\mathbf{F}\boldsymbol{r}_0^N\right). \tag{3.12}$$

Importantly, this transforms the Helmholtz free energy of eqn (3.8) in such a way that the deformation gradient no longer appears in the integration limits but in the integrand instead:

$$F(N,T;\mathbf{F}) = -k_\mathrm{B}T\ln\left[\frac{1}{N!h^{3N}}\int_{\Gamma_0}\exp\left(\frac{-\mathcal{H}_0\left(\boldsymbol{r}_0^N,\boldsymbol{p}_0^N,\mathbf{F}\right)}{k_\mathrm{B}T}\right)\mathrm{d}\boldsymbol{r}_0^N\mathrm{d}\boldsymbol{p}_0^N\right]. \tag{3.13}$$

As a result, the first Piola–Kirchhoff tensor from eqn (3.6) can be evaluated as follows:

$$P(T;\mathbf{F}) = \frac{1}{V_0}\frac{\partial F(N,T;\mathbf{F})}{\partial \mathbf{F}} = -\frac{k_B T}{V_0}\frac{1}{Z_{N\mathbf{F}T}}\frac{\partial Z_{N\mathbf{F}T}}{\partial \mathbf{F}} = \frac{1}{V_0}\left\langle \frac{\partial \mathcal{H}_0\left(\boldsymbol{r}_0^N, \boldsymbol{p}_0^N, \mathbf{F}\right)}{\partial \mathbf{F}} \right\rangle, \quad (3.14)$$

or, after some lengthy calculus:

$$\mathbf{P}(T;\mathbf{F}) = -\frac{1}{V_0}\sum_{i=1}^{N}\left\langle \frac{\boldsymbol{p}_i \otimes \left(\mathbf{F}^{-1}\boldsymbol{p}_i\right)}{m_i} - \frac{\partial \mathcal{V}}{\partial \boldsymbol{r}_i} \otimes \boldsymbol{r}_{i,0} \right\rangle, \quad (3.15)$$

where $\otimes$ denotes the dyadic product of two vectors, $(\boldsymbol{a}\otimes\boldsymbol{b})_{ij} = a_i b_j$, yielding a second-rank tensor. Both in eqn (3.14) and (3.15), $\langle\cdot\rangle$ indicates an ensemble average, although an instantaneous stress $\mathbf{P}^{\text{inst}}$ can be defined by omitting this average in eqn (3.15), such that $\langle \mathbf{P}^{\text{inst}} \rangle = \mathbf{P}$. Similar to the definition of an instantaneous temperature, however, it is important to recognise that only the ensemble-averaged definition of the Piola–Kirchhoff tensor enters thermodynamic relations.

From this definition of the first Piola–Kirchhoff tensor $\mathbf{P}$ and following the continuum relations between this tensor and the second Piola–Kirchhoff stress tensor $\mathbf{S}$ and Cauchy stress tensor $\boldsymbol{\sigma}$,[8] one obtains:

$$\mathbf{S}(T;\mathbf{F}) = \mathbf{F}^{-1}\mathbf{P}(T;\mathbf{F}) = -\frac{1}{V_0}\sum_{i=1}^{N}\left\langle \frac{\left(\mathbf{F}^{-1}\boldsymbol{p}_i\right)\otimes\left(\mathbf{F}^{-1}\boldsymbol{p}_i\right)}{m_i} - \left(\mathbf{F}^{-1}\frac{\partial \mathcal{V}}{\partial \boldsymbol{r}_i}\right)\otimes \boldsymbol{r}_{i,0} \right\rangle; \quad (3.16)$$

$$\boldsymbol{\sigma}(T;\mathbf{F}) = \frac{1}{\det \mathbf{F}}\mathbf{P}(T;\mathbf{F})\mathbf{F}^T = -\frac{1}{V}\sum_{i=1}^{N}\left\langle \frac{\boldsymbol{p}_i \otimes \boldsymbol{p}_i}{m_i} - \frac{\partial \mathcal{V}}{\partial \boldsymbol{r}_i}\otimes \boldsymbol{r}_i \right\rangle. \quad (3.17)$$

The Cauchy stress tensor of eqn (3.17) is the stress tensor most often calculated during each integration step of a molecular simulation to obtain a measure for the internal stress. From the above definition, one can also determine the pressure of the system as (the negative of) the trace (Tr) of the above expression:

$$P(T;\mathbf{F}) = -\frac{1}{3}\mathrm{Tr}\left\{\boldsymbol{\sigma}(T;\mathbf{F})\right\} = \frac{1}{3V}\sum_{i=1}^{N}\left\langle \frac{p_i^2}{m_i} - \frac{\partial \mathcal{V}}{\partial \boldsymbol{r}_i}\cdot \boldsymbol{r}_i \right\rangle, \quad (3.18)$$

although it is more straightforward to obtain an atomic definition of the pressure by realising that the appropriate Gibbs free energy expression for a system under pressure and temperature control is given by

$$G(N, P, T; V) = F(N, T; V) + PV, \quad (3.19)$$

which should be minimised with respect to the volume V to obtain an atomic expression for the pressure. This alternative procedure yields the same results as eqn (3.18).

Eqn (3.4) and (3.5) for the strain and eqn (3.15)–(3.18) for the stress define the sought-after connection between the continuum stress and strain and the atomic properties of a system: the masses m_i, positions $\boldsymbol{r}_i$, and momenta $\boldsymbol{p}_i$ of each of the atoms, as well as interactions $\mathcal{V}$ acting between the atoms and the deformation gradient $\mathbf{F}$ defining the current cell configuration $\mathbf{h}$ compared to the reference cell $\mathbf{h}_0$.

3.3 Ingredients Necessary to Atomically Model MOF Mechanics

Computational modelling is a bottom-up approach in which the macroscopic behaviour of a material is determined starting from knowledge about the positions of its constituents – electrons and nuclei – and the interactions between them. The common goal of any computational modelling endeavour is to understand how interactions at the atomic scale give rise to macroscopically observed properties and to adopt this information to design materials with predesigned functionalities (*e.g.*, susceptible to phase transitions, NLC, NTE). In order to achieve this ambitious target, the following three main questions need to be considered, irrespective of the details of the problem at hand:

1. How can the experimental, macroscopic material consisting of an immense number of atoms be represented by a much smaller number of particles, varying from a few thousands to a few million atoms depending on the available computational power and the choice of model to approximate the interatomic interactions and external conditions (see points 2 and 3)?
2. How can the interatomic interactions, which are inherently many-body and quantum mechanical in nature, be approximated to an extent that they can be used to computationally model the phenomena under study while allowing both for sufficiently large structural models (see point 1) and for a sufficient similarity to the real materials behaviour under the given external conditions (see point 3)?
3. How can, for a given structural model (see point 1) and approximation of the interatomic interactions (see point 2), the material be simulated in such a way that properly averaging the atomic properties over the computer simulation allows for a direct comparison with experimental results?

In this section, these three fundamental questions will be discussed separately. The importance of each of these key aspects in order to obtain reliable results that can further our understanding and design capabilities of the mechanical behaviour of MOFs will be provided, although much of this discussion can be readily generalised to other materials and other properties.

3.3.1 Generating an Accurate Structural Model of the Material

The size of the largest atomic MOF models to date remains limited to a few tens of thousands of atoms and a few tens of nanometres in diameter,[7,17–23] save for a very recent study of a 1 million atom model of MIL-53(Al).[24] Despite this recent increase in computationally accessible length scales, atomic models remain substantially smaller than experimental MOF crystallites at the moment. Therefore, the majority of computational MOF research nowadays starts from the assumption that the properties of a macroscopic MOF material can be approximated well by considering a smaller simulation cell that is repeated *ad infinitum* along the three cell vectors $\boldsymbol{a}_1$, $\boldsymbol{a}_2$, and $\boldsymbol{a}_3$, which define the cell matrix $\mathbf{h}$ of eqn (3.1) (see Figure 3.1). By construction, periodic boundary conditions cannot be adopted to model surface effects in finite MOF crystals. Nevertheless, this periodic ansatz is being used extensively to approximate bulk properties.

The increasing realisation that MOFs come in various degrees of crystallinity[4,25,26] – from almost perfectly crystalline MOFs, over MOFs with local defects or mesopores locally deviating from crystallinity,[5,27–34] to amorphous or glassy MOFs that lack any long-range spatial order[35–41] – has made it increasingly difficult to define accurate structural MOF models. First, the lack of (perfect) order is straining the ansatz of periodic boundary conditions as a *passe-partout* in computational MOF research. Several recent studies have sought to limit the effect of these spurious long-range correlations in MOF simulation cells by considering increasingly larger cells, giving rise to exciting new phenomena not accessible in smaller simulation cells (*vide infra*). However, for glassy or amorphous MOFs, without any long-range order, or when interested in surface effects, even these larger simulation cells cannot be expected to yield accurate predictions, and new and finite MOF crystallite models need to be constructed. Second, even when making abstraction of the validity of periodic boundary conditions to mimic MOF properties, it is not straightforward to come up with appropriate atomic simulation cells for disordered MOFs in the first place. As argued recently,[17,42] this requires a concerted effort from experimentalists and theoreticians to interrogate the MOF structure from the atomic to the macroscopic scale with a varied toolbox of high-resolution techniques and high-throughput automated computational screenings of potential (disordered) MOF structures.[17,42–44] Until such a toolbox has been developed and becomes mainstream accessible, disorder in MOFs can only be treated in an *ad hoc* fashion (*vide infra*), in which the comparison between theoretically predicted and experimentally measured properties quantifies the validity of those approximations – thereby limiting the predictive power of computational research. In what follows, three common pitfalls associated with defining an accurate structural model will be discussed, demonstrating the impact of (i) including disorder at the atomic scale in the periodic simulation cell, (ii) choosing sufficiently large simulation cells, and (iii) going beyond the periodic simulation cell for surface-dominated effects.

A first potential pitfall when modelling MOFs is neglecting the impact of local defects – with a spatial extent of only a few nanometres – on the macroscopic MOF properties. The most prominent example in this category is UiO-66(Zr).[45] Perceived as an exceptionally stable material, a result of its relatively strong zirconium–oxygen coordination bonds and the up to twelvefold coordination of its inorganic building blocks,[45–47] it has been the protagonist in many experimental and computational studies. Thanks to the rather straightforward synthesis of large UiO-66 crystals, it was also one of the first MOFs for which spatial disorder could be characterised extensively, revealing a variety of deviations from periodicity: from local inorganic node and linker vacancies to the formation of correlated nanodomains in which these local vacancies tend to cluster together.[5,29,32] Various works have tried to incorporate, to a different extent, these deviations from perfect crystallinity while still adopting periodic boundary conditions. In 2016, Thornton *et al.* calculated the *ab initio* elastic constants and elastic moduli for a variety of defect-containing UiO-66 simulation cells with a unit cell length of around 2.1 nm, which was sufficiently large to incorporate isolated linker and node vacancies.[48] As visualised in Figure 3.3(a), an appreciable increase in mechanical anisotropy and a decrease in the Young's and shear moduli were observed upon increasing linker vacancy concentration. In a force-field based study on a similar-sized simulation cell, Rogge *et al.* demonstrated that the bulk modulus and the mechanical stability of UiO-66 are also strongly impacted by linker vacancies.[49] Importantly, the extent to which the mechanical behaviour is impacted is dictated not only by the concentration of defects, but also by their distribution throughout the framework.[49] They illustrated that incorporating a realistic amount of defects is necessary to correctly predict the amorphisation pressure of ~1.4 GPa obtained from high-pressure mercury intrusion experiments.[50] Failing to take these defects

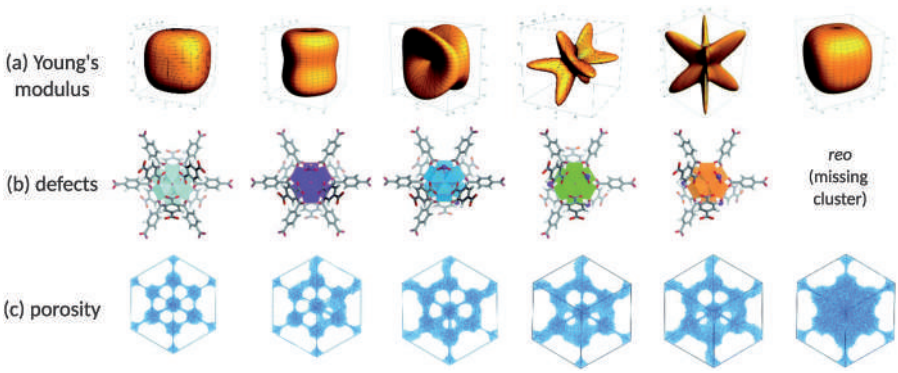

Figure 3.3 (a) Spatially-dependent Young's modulus, (b) visualisation of defects as observed from the perspective of a single cluster and (c) porosity available for adsorption of a 3 Å-diameter probe. Each cluster is coloured according to its coordination number. Adapted from ref. 48 with permission from the Royal Society of Chemistry.

into account overestimates this experimental value by ~0.4 GPa.[49] A similar pitfall also manifests itself for defect-free MOFs in which high-symmetric lattice points can be decorated by building blocks that have a lower symmetry. For instance, Ehrling *et al.* demonstrated that the response of DUT-8(Ni) on gas adsorption depends on the configuration of the nonlinear linkers present in this framework, the configuration of which can be guided during synthesis.[44] This opens up the possibility to design these MOFs,[51] by deriving relations between the local symmetry and structure of the MOF on the one hand, and the macroscopic material behaviour on the other. However, a *conditio sine qua non* for such structure–property relationships is the proper inclusion of these local deviations from crystallinity in the atomistic model.

A second pitfall is underestimating the required size of the atomic model, which leads to spurious effects in the simulation. This pitfall is very easily recognised when studying the stimuli-induced switching behaviour of flexible MOFs or soft porous crystals (SPCs),[52] such as MIL-53(Al)[14] and DMOF-1(Cu).[53,54] Both materials have been experimentally demonstrated to 'breathe' between a large-pore (lp) and a closed-pore (cp) form, and the ability of atomic simulations to reproduce such phase transformations was one of the early successes of MOF modelling.[55,56] However, when adopting periodic boundary conditions, the mechanism through which the phase transition takes place is forced to be a cooperative one, in which all periodic images of the simulation cell undergo the same transition at the same time. By systematically increasing the simulation size in these materials and by removing the periodic boundary conditions,[18,19] it was recently suggested that this cooperative mechanism is artificially imposed by the periodic ansatz, as phase transformations in larger crystals occur gradually instead. In this way, the transition from one phase to another can nucleate locally in the MOF, then propagate and grow through the material *via* a layer-by-layer mechanism.[18,19] The extra degrees of freedom present in the larger simulation cells lead to the proposition of a gradual transition mechanism that is energetically favoured over the cooperative mechanism assumed before, leading to stimuli-induced spatial disorder under the form of phase coexistence.[19] The latter was recently also confirmed experimentally for DUT-8(Ni),[57] a different SPC, through Raman spectroscopy.[58]

Finally, a third pitfall occurs when neglecting the surface of the MOF crystal, which becomes more prominent as the MOF crystallite becomes smaller, given its larger surface-to-volume ratio. For surface-dominated properties, accurate atomistic models need to explicitly account for the MOF surface by removing the periodic boundary conditions along at least one of the directions (or, equivalently, introducing a MOF slab model with a large vacuum region) and properly terminating the interface. Simulating finite MOF crystallites remains to date a largely unexplored area, as the much smaller scale of computational MOF crystallites compared to experimental crystals implies a much larger surface-to-volume ratio and an overestimation of surface effects. However, such finite crystal simulations do provide qualitatively interesting observations, such as the mechanism through which phase transformations

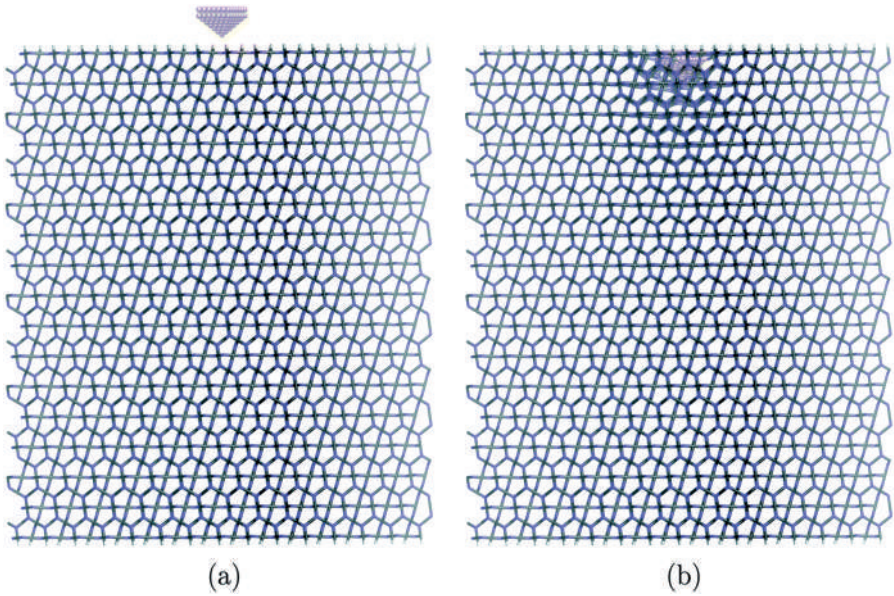

Figure 3.4 Penetration of an atomistic indenter 'tip' into the [111] surface of a coarse grained slab model of HKUST-1 (5 × 5 × 6 supercell), where (a) shows the initial and (b) the final state (colour scheme: black: inorganic moiety; blue: linker; white: terminal CH_3 bead; brown: tungsten atoms). Reproduced from ref. 7 with permission from the Royal Society of Chemistry.

develop in finite DMOF-1 particles.[18] Similarly, mechanical properties that are probed at the surface of the material – such as nanoindentation studies that probe the hardness of the material (see Sections 1.4 and 1.8.1 of Chapter 1) – require a proper termination of the MOF surface. A first step in this direction was set in 2016, when Dürholt *et al.* computationally determined the energy needed to penetrate the [111] surface of HKUST-1 with a tungsten tip, schematically depicted in Figure 3.4.[7] They demonstrated that converged results for the penetration energy could only be reached when both properly terminating the surface and when ensuring that the lateral surface dimensions, which are still treated periodically, are sufficiently large to avoid spurious interactions, thereby connecting to the second pitfall mentioned above.

3.3.2 Approximating the Interactions in a Material: the Level of Theory

As a bottom-up technique, molecular modelling requires an accurate description of the interactions between the nuclei and electrons that make up MOFs to predict macroscopic properties. Many different approaches exist to model these interactions, starting from a fundamental quantum mechanical or *ab initio* treatment, over classical potentials used in force fields, to

coarse-grained (CG) and continuum descriptions. In this order, these models become computationally less expensive – often at the cost of an appreciable loss in accuracy – which opens up the possibility to treat much larger atomic models (see Section 3.3.1) on much longer time scales. Although studies are emerging in which the mechanical behaviour at longer time and length scales becomes accessible *via* CG techniques[7,59,60] or through finite-elements modelling (FEM),[61,62] the mechanical behaviour of MOFs is nowadays mostly characterised using either *ab initio* or atomistic force field approaches.[63] Therefore, these methods and their application to MOF research will be briefly outlined below, with appropriate references to more in-depth reviews.

As the interactions between electrons and nuclei in MOFs are quantum-mechanical in nature, completely characterising the (micro)state of a MOF requires knowledge of the positions (and possibly intrinsic spin coordinates) of all its nuclei and the positions and intrinsic spin coordinates of all its electrons, collected in the many-body wavefunction $|\Psi\rangle$, and this for every time instance of interest.[§] In the absence of time-dependent external fields, the stationary many-body wavefunction $|\psi_n\rangle$ can be obtained by solving the time-independent Schrödinger equation:[64]

$$\hat{H}|\psi_n\rangle = E_n|\psi_n\rangle, \tag{3.20}$$

in which E_n and $|\psi_n\rangle$ are the eigenvalues and eigenstates, respectively, of the Hamiltonian $\hat{H}$ that describes the interactions in the system. The quantum label n is used to differentiate between the different states. Under the assumption that the $N^{(e)}$ electrons and N nuclei in the system only interact through Coulomb interactions, this Hamiltonian can be written as

$$\hat{H} = \hat{T}_N + \hat{T}_e + \hat{\mathcal{V}}_{NN} + \hat{\mathcal{V}}_{ee} + \hat{\mathcal{V}}_{Ne}. \tag{3.21}$$

Herein,

$$\hat{T}_N = \sum_{i=1}^{N} \frac{\boldsymbol{p}_i \cdot \boldsymbol{p}_i}{2m_i} \quad \text{and} \quad \hat{T}_e = \sum_{i=1}^{N^{(e)}} \frac{\boldsymbol{p}_i^{(e)} \cdot \boldsymbol{p}_i^{(e)}}{2m_i^{(e)}} \tag{3.22}$$

are the kinetic energy operators associated with the nuclei and the electrons, respectively,

$$\hat{\mathcal{V}}_{NN} = \frac{1}{4\pi\varepsilon_0} \sum_{i=1}^{N} \sum_{j=i+1}^{N} \frac{Z_i Z_j}{\left|\boldsymbol{r}_i - \boldsymbol{r}_j\right|} \quad \text{and} \quad \hat{\mathcal{V}}_{ee} = \frac{1}{4\pi\varepsilon_0} \sum_{i=1}^{N^{(e)}} \sum_{j=i+1}^{N^{(e)}} \frac{1}{\left|\boldsymbol{r}_i^{(e)} - \boldsymbol{r}_j^{(e)}\right|} \tag{3.23}$$

are the potential energy operators associated with the repulsive Coulomb interactions between each pair of nuclei and each pair of electrons, respectively, and

$$\hat{\mathcal{V}}_{Ne} = -\frac{1}{4\pi\varepsilon_0} \sum_{i=1}^{N} \sum_{j=1}^{N^{(e)}} \frac{Z_i}{\left|\boldsymbol{r}_i - \boldsymbol{r}_j^{(e)}\right|} \tag{3.24}$$

[§]Of course within the limitations set out by the Heisenberg uncertainty principle.

is the potential energy operator associated with the attractive Coulomb interaction between each nucleus–electron pair. In these expressions, $m_i^{(e)}$, $\boldsymbol{r}_i^{(e)}$, and $\boldsymbol{p}_i^{(e)}$ are the mass, position, and momentum of the ith electron, Z_i is the nuclear charge of the ith nucleus, and ε_0 is the permittivity of the vacuum.

If our computational model (see Section 3.3.1) consists of N nuclei and $N^{(e)}$ electrons and if we can neglect the spin of the nuclei, the wavefunctions $|\psi_n\rangle$ depend on $3N + 4N^{(e)}$ degrees of freedom. For typical MOF unit cells, which contain about 100 to 10 000 nuclei and about one order of magnitude more electrons, it would be an extraordinary task to fully determine this wavefunction. Therefore, different approximations exist to determine the eigenenergies E_n, and especially the ground-state energy E_0, of eqn (3.20).

A first approximation, the Born–Oppenheimer (BO) approximation, starts from the realisation that electrons are much lighter than nuclei, and will therefore equilibrate on a much shorter timescale under typical conditions.[65] From the perspective of the electrons, the nuclei can be assumed as 'clamped'. If the excited electronic states are furthermore much higher in energy than the ground state so that nuclear excitations cannot induce electronic excitations (the so-called adiabatic approximation), the stationary Schrödinger equation (eqn (3.20)) can be separated into an electronic and a nuclear eigenvalue problem. The former reads

$$\hat{H}_\mathrm{e} \left|\psi_n^{(e)}\right\rangle = \left(\hat{T}_e + \hat{\mathcal{V}}_{NN} + \hat{\mathcal{V}}_{ee} + \hat{\mathcal{V}}_{Ne}\right)\left|\psi_n^{(e)}\right\rangle = \mathcal{V}_n^\mathrm{BO}\left|\psi_n^{(e)}\right\rangle, \tag{3.25}$$

in which the stationary electronic wavefunctions $|\psi_n^{(e)}\rangle$ (with $4N^{(e)}$ degrees of freedom) and associated eigenenergies $\mathcal{V}_n^\mathrm{BO}$ are determined from the electronic Hamiltonian $\hat{H}_\mathrm{e}$. Importantly, although the nuclear coordinates still enter the electronic Hamiltonian through the terms $\hat{\mathcal{V}}_{NN}$ and $\hat{\mathcal{V}}_{Ne}$, they do so not as degrees of freedom but as fixed parameters because of the clamped nuclei approximation. By varying the nuclear coordinates and again solving eqn (3.25), the eigenenergies $\mathcal{V}_n^\mathrm{BO}$ can be determined as a function of the $3N$ nuclear coordinates. These hypersurfaces are known as the Born–Oppenheimer surfaces or potential energy surfaces (PES) of the system on which the nuclei move. Knowledge of these surfaces then allows one to solve the nuclear eigenvalue problem, the eigenstates of which describe the vibrations and rotations of the nuclei.

While the Born–Oppenheimer approximation decouples the electronic and the nuclear eigenvalue problem, the number of degrees of freedom remains formidable, especially for the electronic eigenvalue problem in eqn (3.25). As a result, approaches aiming to immediately determine the electronic wavefunctions – so-called wavefunction-based techniques such as Hartree–Fock – are computationally very expensive and are only seldomly used in MOF research. When they are used, first a small finite cluster is cut out of the MOF material to limit the number of electrons in the simulation model, as outlined in more detail in ref. 66.

A much more popular quantum-mechanical method to solve the electronic eigenvalue problem for solid-state materials (such as MOFs) was pioneered by

Hohenberg and Kohn, whose theorems form the basis of density functional theory (DFT).[67] These theorems state that the ground state energy $\mathcal{V}_0^{\mathrm{BO}}$ of eqn (3.25) is a unique functional of the ground state electron density, which can be found variationally as the density that minimises this (unknown) functional.[68] Hence, instead of solving eqn (3.25) for the highly multidimensional wavefunction, the Hohenberg–Kohn theorems allow one to solve for the three-dimensional ground state electron density instead, and to obtain all relevant ground state properties from this density. In the traditionally used Kohn–Sham formalism, this problem is hugely simplified by considering a fictitious system of non-interacting electrons moving in an effective potential, which is chosen such that the system has the same ground-state electron density as the actual interacting system.[69] In this way, the variational principle gives rise to single-particle equations, the so-called Kohn–Sham equations, the solutions of which yield the ground-state electron density. While this method is formally exact up to this point, it features unknown contributions to the effective potential, arising from the unknown exchange-correlation functional. Hence, to actually find the ground-state electron density, one needs to postulate an appropriate form of this exchange-correlation functional. A vast number of different functionals have been proposed to this end, which strongly vary in computational cost and accuracy. However, as DFT is in general much faster than wavefunction-based approaches, it has been used extensively in MOF research. For a thorough discussion of the applications and limitations of DFT in modelling MOFs, the recent review by Mancuso *et al.* forms an excellent starting point.[70]

The atomic interactions in MOFs can also be modelled classically. The aim of classical interaction potentials, also called force fields, is to approximate the ground-state Born–Oppenheimer surface $\mathcal{V}_0^{\mathrm{BO}}$ of eqn (3.25), which depends on all nuclear coordinates, by a sum of analytical functions that each depend on a limited number of nuclear coordinates (typically two, three, or four) and on a limited number of fitting parameters. Force fields can typically be divided into bonded and nonbonded interaction terms. The former are often simple functions of the internal coordinates of covalently bonded nuclei, such as bonds, bends, and torsion terms, while the latter describe interactions also between nonbonded nuclei, such as Coulomb and van der Waals interactions. Thanks to their analytical form, these classical potentials can be used to efficiently calculate the forces on each of the nuclei without the need to resort to expensive electronic structure methods. However, most force fields preclude the description of bond reorganisation, which limits their applicability. Different force fields differ not only in the form of the analytical functions they contain – some do inherently account for anharmonic interaction potentials, for instance – but also in the way the fitting parameters are determined. MOF force fields are often parametrised based on data obtained from electronic structure methods. For instance, in the first flexible MOF force field, derived by Greathouse *et al.*, an appropriate parametrisation of terms associated with the inorganic node in MOF-5 was obtained from preceding DFT calculations.[71] Recently, more systematic

parametrisation approaches have been developed, in which the force field (FF) parameters are determined based on the *ab initio* optimised structure and the local shape of the PES around this optimised structure. Examples include MOF-FF,[72,73] BTW-FF,[74] QuickFF,[75,76] and VMOF.[77] In the context of this work, also the approach introduced by Heinen *et al.*, in which a force field was derived by fitting to the *ab initio* elastic constants,[78] is noteworthy to mention. For a more in-depth discussion of force fields for MOFs, the reader is referred to ref. 76 and 79.

3.3.3 Exploring the Potential Energy Surface for a System under Stress Control

When experimentally extracting the mechanical behaviour of a MOF material, the MOF sample is often held under temperature control, while simultaneously controlling either the pressure (or, more generally, stress) or the strain. To obtain comparable properties from a molecular simulation, it is necessary to impose the same control conditions while the system samples the PES constructed in Section 3.3.2, *i.e.*, to ensure that the system samples every region of the PES with a probability dictated by the experimental conditions. One way to trace such a representative trajectory on the PES is by performing a molecular dynamics (MD) simulation, in which the nuclear structure of the MOF is followed through time.[80,¶] In an MD simulation, temperature or stress control means that the Hamiltonian equations of motion following from eqn (3.9), which are simply the Newton equations for the nonrelativistic nuclei, need to be adapted. While temperature and pressure control is well developed, general stress control in MD simulations is substantially less straightforward as different subtleties arise for soft anisotropic materials such as MOFs, as shown below.

Central in the discussion of temperature and stress control of systems *in thermodynamic equilibrium* is the ensemble concept. An ensemble denotes the collection of microstates (here the positions and momenta of each of the N nuclei of the MOF and, if present, its simulation cell matrix $\mathbf{h}$) that are accessible under the given macroscopic conditions (here typically the temperature T and stress $\boldsymbol{\sigma}$ under which the experiment takes place). Ensembles are labelled based on the macroscopic variables that are controlled. These control variables come in conjugate pairs, including temperature T *vs.* entropy S (which also determines the energy E), pressure P *vs.* volume V, and chemical potential μ *vs.* number of particles N. An ensemble is fully defined by choosing one out of each pair of conjugate control variables, in which one needs to ensure that at least one of the variables scales with the size of the sample (either the entropy/energy, volume, or particle number). For gases

¶A very popular and versatile alternative to MD are Monte Carlo (MC) simulations,[309] which are very often used to study adsorption in MOFs. However, MC routines are typically less suited to describe collective structural framework deformations discussed here, as the associated MC trial moves are only seldomly accepted.

and liquids, the most often used ensembles are the microcanonical or *NVE* ensemble, the canonical or *NVT* ensemble, the isothermal–isobaric or *NPT* ensemble, and the grand canonical or μVT ensemble.[80]

For typical (Newtonian) fluids, the pressure P is the only stress state the material can withstand, and the volume forms an appropriate variable to describe the response of such a system to pressure control. For solids, however, this situation differs. Given that a solid is typically anisotropic, the volume alone does not suffice to describe the simulation cell, and instead the six independent components of the simulation cell matrix $\mathbf{h}$ introduced in eqn (3.1) need to be specified.[81,82,‖] In addition, for anisotropic solids, it also makes sense to probe their response to anisotropic stresses $\boldsymbol{\sigma}$, as defined by the deviatoric Cauchy stress tensor $\boldsymbol{\sigma}_a$ that remains after subtracting the hydrostatic pressure from the Cauchy stress:**

$$\boldsymbol{\sigma}_a = \boldsymbol{\sigma} + P\mathbf{I}. \tag{3.26}$$

As a result, for anisotropic solids, instead of simply choosing between the scalar variables P and V as conjugate variables, one needs to choose between the matrix variables $\boldsymbol{\sigma}$ and $\mathbf{h}$, the latter of which defines the Lagrangian strain through eqn (3.4). However, $\boldsymbol{\sigma}$ and $\mathbf{h}$ do not form a pair of conjugate variables, which makes the definition of constant-stress ensembles substantially less straightforward (*vide infra*). While this distinction between ensembles for fluids and anisotropic solids was already recognised in 1984,[15] the nomenclature used in computational research can often obscure the exact ensemble – and hence the exact control variables – used during the simulation. For instance, the label '$N\boldsymbol{\sigma}T$ ensemble' has been used both to denote an ensemble in which the full stress $\boldsymbol{\sigma}$ is controlled (in addition to the number of particles and the temperature) and to denote an ensemble in which only the pressure P is controlled but in which the cell matrix $\mathbf{h}$ could change anisotropically (which is a more restrictive ensemble than the previous one).[83] Therefore, a more appropriate ensemble classification to study MOFs and other anisotropic solids has been proposed in ref. 83, which can be found in Table 3.1 and which will be used in this chapter.

Given the above discussion, it may come as no surprise that stress control or barostat algorithms were initially derived to control only the pressure, while allowing only for isotropic volume deformations. The first such barostat algorithm was proposed by Andersen.[84] Andersen recognised that pressure control could be achieved by describing the system as a function of the volume and the fractional coordinates defined in Section 3.2 and by

‖Although the cell matrix contains nine components, three of them define the cell orientation with respect to the frame of reference and hence carry no intrinsic physical meaning. Therefore, the cell matrix is often assumed to be either symmetrised or upper triangular to fix these three degrees of freedom.

**Note that the pressure was defined in eqn (3.18) as *the negative* of the trace of the stress tensor. If this minus sign is not used, the plus sign in eqn (3.26) should also be replaced by a minus sign.

Table 3.1 Overview of the different thermodynamic ensembles considered for MOFs at a constant number of particles N according to the unified notation proposed in ref. 83, where crosses indicate which variables are controlled. Next to the number of particles, the ensemble is defined by controlling the volume V or the pressure P, the cell shape matrix $\mathbf{h}_0$ or the deviatoric stress $\boldsymbol{\sigma}_a$, and the energy/enthalpy (E or H) or temperature T. The last column indicates the notation used in popular software packages such as DL_POLY,[312] LAMMPS,[313] and CP2K/QUICKSTEP,[314] which may lead to confusion in some cases due to making no distinction between constant-pressure and constant-stress ensembles. Adapted from ref. 83 with permission from American Chemical Society, Copyright 2015.

Ensemble	N	V	$\mathbf{h}_0$	P	$\boldsymbol{\sigma}_a$	E or H	T	Other notations
$(N,V,\mathbf{h}_0,E)$	×	×	×			×		*NVE*
$(N,V,\mathbf{h}_0,T)$	×	×	×				×	*NVT*
$(N,V,\boldsymbol{\sigma}_a,H)$	×	×			×	×		
$(N,V,\boldsymbol{\sigma}_a,T)$	×	×			×		×	
$(N,P,\mathbf{h}_0,H)$	×		×	×		×		*NPH*, NPE_I
$(N,P,\mathbf{h}_0,T)$	×		×	×			×	*NPT*, NPT_I
$(N,P,\boldsymbol{\sigma}_a,H)$	×			×	×	×		*NPH*
$(N,P,\boldsymbol{\sigma}_a,T)$	×			×	×		×	*NPT*
$(N,V,\boldsymbol{\sigma}_a=\mathbf{0},H)$	×	×			$\boldsymbol{\sigma}_a=\mathbf{0}$	×		
$(N,V,\boldsymbol{\sigma}_a=\mathbf{0},T)$	×	×			$\boldsymbol{\sigma}_a=\mathbf{0}$		×	
$(N,P,\boldsymbol{\sigma}_a=\mathbf{0},H)$	×			×	$\boldsymbol{\sigma}_a=\mathbf{0}$	×		$N\boldsymbol{\sigma}H$, NPE_F
$(N,P,\boldsymbol{\sigma}_a=\mathbf{0},T)$	×			×	$\boldsymbol{\sigma}_a=\mathbf{0}$		×	$N\boldsymbol{\sigma}T$, NPT_F

extending the system's Hamiltonian of eqn (3.9) with two terms describing the kinetic energy and the (elastic) potential energy of a piston acting on the system's volume. This 'extended Hamiltonian' approach was generalised by Parrinello and Rahman by letting the piston define not only the volume of the simulation cell, but all components of the simulation cell matrix $\mathbf{h}$ instead (while still only accepting isotropic pressure as a control variable).[85] In 1981, Parrinello and Rahman extended this approach to allow imposing the whole stress tensor $\boldsymbol{\sigma}$,[86] which was later further refined to allow for simultaneous temperature control and cast in a true Hamiltonian form by Ray and Rahman.[15,87,88] In this latter formulation, which is implemented in many MD codes as the Parrinello–Rahman (PR) barostat, the system's Hamiltonian of eqn (3.9) is extended to read[††]

$$\mathcal{H}^{\mathrm{PR}}\left(\boldsymbol{s}^N,\boldsymbol{\pi}^N,\mathbf{h},\mathbf{p}_g\right)=\sum_{i=1}^{N}\frac{\left(\mathbf{h}^{-T}\boldsymbol{\pi}_i\right)\cdot\left(\mathbf{h}^{-T}\boldsymbol{\pi}_i\right)}{2m_i}+\mathcal{V}\left(\mathbf{h}\boldsymbol{s}^N\right)+\frac{\mathbf{p}_g:\mathbf{p}_g}{2W}-V_0\mathbf{S}:\boldsymbol{\eta}. \qquad (3.27)$$

[††]The elastic term in eqn (3.27) is slightly more cumbersome in the original description, since Parrinello and Rahman made a distinction between applying a purely isotropic stress, in which case the elastic term should simply read $-P(V-V_0)$, and a stress state that is not purely isotropic, in which case eqn (3.27) is valid. As the interest here is specifically for the latter case, eqn (3.27) will be adopted throughout. It is important to note, however, that the PR barostat for isotropic stresses does not suffer from the same approximations as the anisotropic PR barostat.

In this expression, which can be extended to simultaneously allow for temperature control,[88] $\boldsymbol{\pi}_i = \mathbf{h}^T \boldsymbol{p}_i$ is the momentum conjugate to the fractional coordinates $\boldsymbol{s}_i$ of particle i, and $\mathbf{p}_g$ is the cell momentum matrix conjugate to the cell matrix $\mathbf{h}$. The third and fourth terms in eqn (3.27) describe the kinetic and elastic energy associated with cell deformations, the latter being described by the product of the reference volume V_0 and the double contraction of the second Piola–Kirchhoff tensor of eqn (3.16) and the finite Lagrangian strain of eqn (3.4). As a result, this Hamiltonian depends on a reference cell matrix $\mathbf{h}_0$ through both the reference cell volume and the strain, raising the same limitations on its applicability as discussed in Section 3.2.1.

Although being widely used, the PR barostat suffers from two inaccuracies which may become nonnegligible for soft framework materials such as MOFs. First, since the transformation from the original Hamiltonian in eqn (3.9) to that of eqn (3.27) is not canonical, as shown in ref. 8, the PR equations of motion are only satisfied exactly if the time derivative of the cell matrix can be neglected with respect to the time derivatives of the fractional coordinates ($|\dot{\mathbf{h}}\boldsymbol{s}_i| \ll |\mathbf{h}\dot{\boldsymbol{s}}_i|$).[15] Second, the direct dependence of the equations of motion on the cell matrix is unsatisfactory. Consider a modular transformation $\mathbf{T}$ that transforms the cell matrix $\mathbf{h}$ to $\mathbf{h}' = \mathbf{hT}$, where $\mathbf{T}$ is a 3×3 matrix only containing integer elements and chosen such that $\det\mathbf{T} = 1$. This transformation is a simple volume-conserving redefinition of the periodic cell vectors. Describing the system in terms of $\mathbf{h}'$ is completely interchangeable with describing it in terms of $\mathbf{h}$. However, the PR Hamiltonian and equations of motion do explicitly depend on this choice. As a result, the PR equations of state are not modularly invariant (or T-invariant), as recognised by Cleveland and Wentzcovitch, and a system's trajectory through time in a PR-controlled MD simulation will artificially depend on the chosen cell matrix.[89,90]

A solution to both drawbacks is to select the deformation gradient $\mathbf{F}$ of eqn (3.2) instead of $\mathbf{h}$ as the fundamental variable describing the cell deformation. By construction with respect to a reference cell matrix, $\mathbf{F}$ is modularly invariant, and any Hamiltonian that only depends on $\mathbf{F}$ is hence also modularly invariant.[91] This approach was followed by Tadmor *et al.*, who used the deformation gradient to define the generating function of eqn (3.10).[8] Given that, in an MD simulation, the deformation gradient explicitly depends on time, this generating function yields the transformed Hamiltonian

$$\mathcal{H}_0\left(\boldsymbol{r}_0^N, \boldsymbol{p}_0^N, \mathbf{F}\right) = \sum_{i=1}^{N} \frac{\left(\mathbf{F}^{-T}\boldsymbol{p}_{i,0}\right)\cdot\left(\mathbf{F}^{-T}\boldsymbol{p}_{i,0}\right)}{2m_i} + \mathcal{V}\left(\mathbf{F}\boldsymbol{r}_0^N\right) - \sum_{i=1}^{N}\left(\mathbf{F}^{-T}\boldsymbol{p}_{i,0}\right)\cdot\left(\dot{\mathbf{F}}\boldsymbol{r}_{i,0}\right), \quad (3.28)$$

Extending this Hamiltonian with the kinetic and potential energy terms of the barostat yields

$$\mathcal{H}\left(\boldsymbol{r}_0^N, \boldsymbol{p}_0^N, \mathbf{F}, \mathbf{p}_g\right) = \sum_{i=1}^{N} \frac{\left(\mathbf{F}^{-T}\boldsymbol{p}_{i,0}\right)\cdot\left(\mathbf{F}^{-T}\boldsymbol{p}_{i,0}\right)}{2m_i} + \mathcal{V}\left(\mathbf{F}\boldsymbol{r}_0^N\right) + \frac{\mathbf{p}_g : \mathbf{p}_g}{2W} - V_0\mathbf{S} : \boldsymbol{\eta} - \sum_{i=1}^{N}\left(\mathbf{F}^{-T}\boldsymbol{p}_{i,0}\right)\cdot\left(\dot{\mathbf{F}}\boldsymbol{r}_{i,0}\right). \quad (3.29)$$

Compared to the PR Hamiltonian of eqn (3.27), an additional last term appears in eqn (3.29) which ensures that modularly invariant equations of motion are obtained under stress control.[8]

A remaining issue, which was also present in the PR barostat, is that both Hamiltonian formulations – and hence also the equations of motion – feature the second Piola–Kirchhoff tensor **S** as the stress control variable. As a result, the second Piola–Kirchhoff tensor is also the property to which the system converges, as demonstrated in Figure 3.5 for an MD simulation of an aluminium crystal, although it is the Cauchy stress $\boldsymbol{\sigma}$ that is controlled experimentally.[92] While this difference between both properties is negligible for small deformations, it becomes important for larger deformations from the cell matrix $\mathbf{h}_0$, as can be observed from eqn (3.16)–(3.17). This difference may hence play a crucial role during phase transitions in MOFs. To overcome this, Miller *et al.* developed an adaptive 'Cauchystat', in which the Cauchy stress is directly controlled through proportional feedback control.[92]

Besides these Hamiltonian approaches to impose stress control, many other barostats have been introduced. Among those still used extensively today are the Berendsen barostat,[93] the Hoover barostat,[94,95] the barostat developed by Martyna, Tobias, and Klein (MTK),[96] and the Langevin barostat.[97] Given that these approaches do not start from a canonical transformation of the Hamiltonian, they allow for more freedom in defining the equations of motion which may also benefit their convergence.[92] Recently, stress control achieved through the Berendsen, MTK, and Langevin barostats was compared to study phase transformations in MOFs, demonstrating that the Berendsen barostat does not sample the correct constant-stress ensemble, whereas the MTK and Langevin barostats lead to interchangeable results, as shown in Figure 3.6.[83]

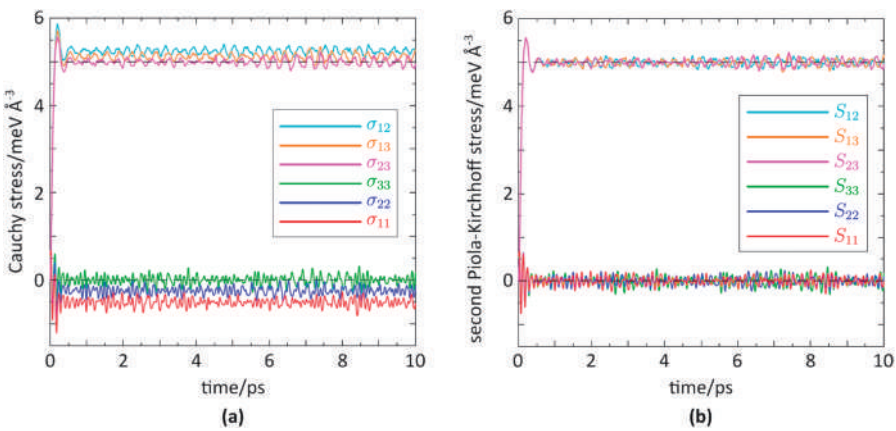

Figure 3.5 Instantaneous values of (a) the Cauchy stress and (b) the second Piola–Kirchhoff stress during a short MD simulation of a perfect aluminium crystal using the PR barostat. The horizontal dashed lines indicate the stress values supplied to the PR barostat (5 meV Å^{-3} for the off-diagonal elements, 0 meV Å^{-3} for the diagonal elements), showing that the components of the second Piola–Kirchhoff tensor rather than those of the Cauchy stress converge to these values. Adapted from ref. 92 with permission from the American Institute of Physics, Copyright 2016.

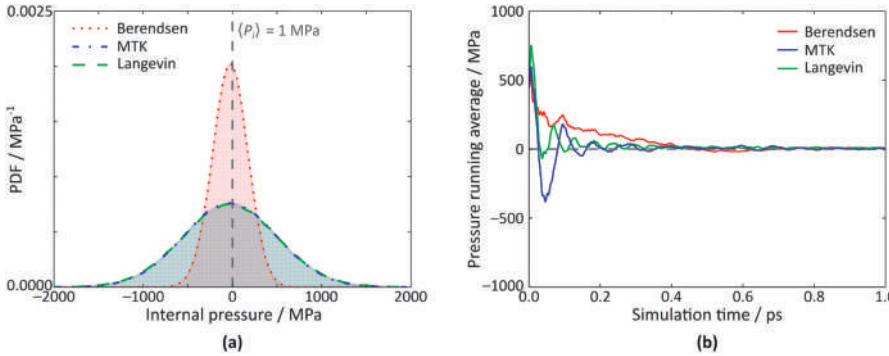

Figure 3.6 Internal pressure exhibited by MIL-53(Al) during an (N, P, $\boldsymbol{\sigma}_a = \mathbf{0}$, T) MD simulation at 1 MPa and 300 K using the Berendsen, MTK, and Langevin barostats and starting from the lp phase of this material at 0 K. (a) Probability density function (PDF) generated over a simulation time of 800 ps. (b) Running average of the internal pressure generated for the first picosecond. Adapted from ref. 83 with permission from American Chemical Society, Copyright 2015.

3.4 The Equilibrium Mechanical Behaviour of MOFs: the Elastic Regime

MOFs exhibit an extremely rich versatility in their response to mechanical stimuli, especially when the magnitude of the stimulus increases (see Sections 3.5 and 3.6). However, near an equilibrium configuration, the mechanical response of a MOF can be completely characterised by the stiffness or elasticity tensor $\mathbf{C}$, which relates the (Cauchy) stress $\boldsymbol{\sigma}$ that needs to be exerted on the material to realise an infinitesimal (Cauchy) strain $\boldsymbol{\varepsilon}$:

$$\boldsymbol{\sigma} = \mathbf{C} : \boldsymbol{\varepsilon} \Leftrightarrow \sigma_{\alpha\beta} = \sum_{\gamma=1}^{3}\sum_{\delta=1}^{3} C_{\alpha\beta\gamma\delta}\varepsilon_{\gamma\delta}. \tag{3.30}$$

Eqn (3.30) can be regarded as the 3D generalisation of Hooke's law for a 1D spring.[‡‡] The infinitesimal strain $\boldsymbol{\varepsilon}$ entering this expression is obtained from both the finite Lagrangian and Eulerian strains defined in eqn (3.4) and eqn (3.5) in the limit of small (infinitesimal) deformations.[98] Since both the stress and strain are 3×3 second-rank tensors, the stiffness tensor $\mathbf{C}$ as well as its inverse, the compliance tensor $\mathbf{S} = \mathbf{C}^{-1}$, are $3 \times 3 \times 3 \times 3$ fourth-rank tensors, the elements of which completely govern the response of a material to 'small' stresses.

[‡‡]Eqn (3.30) is not the only way to define the stiffness tensor. Alternative definitions are based on the energy density of a deformed material in the harmonic approximation, eqn (3.33), or through the equation of motion of an elastic wave propagating through the material, an approach that is often followed experimentally,[247] but which is seldomly used computationally.[299] For an unstressed material, all three definitions are interchangeable. Only when a material is held under external stress does care need to be taken to distinguish between these three definitions.[247]

To properly define 'small' stresses, it suffices to expand the Helmholtz free energy of eqn (3.8) with respect to the Lagrangian strain $\boldsymbol{\eta}$ around the unstressed equilibrium configuration:

$$F(N,T;\boldsymbol{\eta}) = F(N,T;\boldsymbol{\eta}_0 = \mathbf{0}) + \sum_{\alpha,\beta=1}^{3} \left.\frac{\partial F(N,T;\boldsymbol{\eta})}{\partial \eta_{\alpha\beta}}\right|_{\boldsymbol{\eta}_0=\mathbf{0}} \eta_{\alpha\beta} + \frac{1}{2}\sum_{\alpha,\beta,\gamma,\delta=1}^{3} \left.\frac{\partial^2 F(N,T;\boldsymbol{\eta})}{\partial \eta_{\alpha\beta}\partial \eta_{\gamma\delta}}\right|_{\boldsymbol{\eta}_0=\mathbf{0}} \eta_{\alpha\beta}\eta_{\gamma\delta} + \mathcal{O}(\eta^3). \tag{3.31}$$

By combining eqn (3.7) with the definitions of eqn (3.4) and (3.16), one finds that $\partial F/\partial \eta_{\alpha\beta} = V_0 S_{\alpha\beta}$, where V_0 is the volume of the reference configuration and $S_{\alpha\beta}$ are the elements of the second Piola–Kirchhoff tensor. Hence, in an unstressed configuration, the second term in the right-hand side of eqn (3.31) vanishes. Furthermore, $F(N, T; \boldsymbol{\eta}_0 = \mathbf{0}) \equiv F_0$ is a constant that can be absorbed by the left-hand side of eqn (3.31). As a result, eqn (3.31) can be rewritten as:

$$F(N,T;\boldsymbol{\eta}) - F_0 = \frac{V_0}{2}\sum_{\alpha,\beta,\gamma,\delta=1}^{3} \left.\frac{\partial S_{\alpha\beta}(N,T;\boldsymbol{\eta})}{\partial \eta_{\gamma\delta}}\right|_{\boldsymbol{\eta}_0=\mathbf{0}} \eta_{\alpha\beta}\eta_{\gamma\delta} + \mathcal{O}(\eta^3). \tag{3.32}$$

For a configuration sufficiently close to equilibrium, we may replace the Lagrangian strain $\boldsymbol{\eta}$ in eqn (3.32) by the infinitesimal strain $\boldsymbol{\varepsilon}$, and the second Piola–Kirchhoff tensor $\mathbf{S}$ by the Cauchy tensor $\boldsymbol{\sigma}$. Together with the definition of the stiffness tensor in eqn (3.30), this yields:

$$F(N,T;\boldsymbol{\varepsilon}) - F_0 = \frac{V_0}{2}\sum_{\alpha,\beta,\gamma,\delta=1}^{3} C_{\alpha\beta\gamma\delta}\varepsilon_{\alpha\beta}\varepsilon_{\gamma\delta} + \mathcal{O}(\varepsilon^3) = \frac{V_0}{2}\boldsymbol{\varepsilon}:\mathbf{C}:\boldsymbol{\varepsilon} + \mathcal{O}(\varepsilon^3). \tag{3.33}$$

Eqn (3.33) demonstrates the importance of the stiffness tensor: its elements completely define the (change in) free energy of the material upon infinitesimal strain, and hence completely define how the material will respond to a small mechanical stimulus. Because of the truncation of eqn (3.33) up to second order, the 81 elements that enter the stiffness tensor are called second-order elastic constants (higher-order elastic constants exist but have to date not been reported for MOFs). A very similar derivation starting from the internal energy instead of the free energy gives an expression similar to eqn (3.33); the difference being that the internal energy U is the appropriate thermodynamic potential when entropy is controlled instead of temperature. As a result, the elastic constants derived when starting from the internal energy are defined as the *adiabatic* elastic constants $V_0 C_{\alpha\beta\gamma\delta} = \partial^2 U/\partial\varepsilon_{\alpha\beta}\partial\varepsilon_{\gamma\delta}$, whereas eqn (3.33) gives rise to the *isothermal* elastic constants $V_0 C_{\alpha\beta\gamma\delta} = \partial^2 F/\partial\varepsilon_{\alpha\beta}\partial\varepsilon_{\gamma\delta}$.

The 81 elements within the stiffness and compliance tensors are not all independent. As these tensors are the second-order derivatives of the free energy with respect to the strain and the order of differentiation is unimportant, $C_{\gamma\delta\alpha\beta} = C_{\alpha\beta\gamma\delta}$ and only 45 independent elements remain (the major

symmetry of **C**). Furthermore, because of the symmetry of the stress and strain tensors, eqn (3.30) implies that $C_{\beta\alpha\gamma\delta} = C_{\alpha\beta\delta\gamma} = C_{\alpha\beta\gamma\delta}$ (the minor symmetries of **C**).[8] As a result, for a general material, 21 independent elastic constants exist, although the symmetry of the unit cell can reduce this number further – *e.g.*, the elastic tensor of a cubic material is defined by only three independent constants.[99] Because of the general symmetries of the stress, strain, and stiffness tensors, one often writes the infinitesimal strain and Cauchy stress tensors as 6 × 1 vectors that inherently take into account these symmetries using the so-called Voigt contraction,[100] as detailed further in Section 2.2.1 of Chapter 2:

$$\boldsymbol{\sigma} = [\sigma_{11}\ \sigma_{22}\ \sigma_{33}\ \sigma_{23}\ \sigma_{13}\ \sigma_{12}]^T \quad \boldsymbol{\varepsilon} = [\varepsilon_{11}\ \varepsilon_{22}\ \varepsilon_{33}\ 2\varepsilon_{23}\ 2\varepsilon_{13}\ 2\varepsilon_{12}]^T. \tag{3.34}$$

Likewise, the fourth-rank compliance and stiffness tensors can be reduced to 6 × 6 matrices that account for the minor symmetries:

$$\mathbf{C} = \begin{bmatrix} C_{1111} & C_{1122} & C_{1133} & C_{1123} & C_{1113} & C_{1112} \\ C_{2211} & C_{2222} & C_{2233} & C_{2223} & C_{2213} & C_{2212} \\ C_{3311} & C_{3322} & C_{3333} & C_{3323} & C_{3313} & C_{3312} \\ C_{2311} & C_{2322} & C_{2333} & C_{2323} & C_{2313} & C_{2312} \\ C_{1311} & C_{1322} & C_{1333} & C_{1323} & C_{1313} & C_{1312} \\ C_{1211} & C_{1222} & C_{1233} & C_{1223} & C_{1213} & C_{1212} \end{bmatrix}$$

$$\mathbf{S} = \begin{bmatrix} S_{1111} & S_{1122} & S_{1133} & 2S_{1123} & 2S_{1113} & 2S_{1112} \\ S_{2211} & S_{2222} & S_{2233} & 2S_{2223} & 2S_{2213} & 2S_{2212} \\ S_{3311} & S_{3322} & S_{3333} & 2S_{3323} & 2S_{3313} & 2S_{3312} \\ 2S_{2311} & 2S_{2322} & 2S_{2333} & 4S_{2323} & 4S_{2313} & 4S_{2312} \\ 2S_{1311} & 2S_{1322} & 2S_{1333} & 4S_{1323} & 4S_{1313} & 4S_{1312} \\ 2S_{1211} & 2S_{1222} & 2S_{1233} & 4S_{1223} & 4S_{1213} & 4S_{1212} \end{bmatrix}. \tag{3.35}$$

Due to the major symmetry of **C**, the matrices in eqn (3.35) are symmetric. The factor of two appearing in the last three elements of the strain vector of eqn (3.34) and the factors of two and four appearing in the compliance matrix of eqn (3.35) arise so that Hooke's law in 3D, eqn (3.30), can be written in Voigt notation as $\boldsymbol{\sigma} = \mathbf{C}\boldsymbol{\varepsilon}$ or $\boldsymbol{\varepsilon} = \mathbf{S}\boldsymbol{\sigma}$. In what follows, the Voigt notation will be systematically adopted.

Although eqn (3.35) fully defines the elastic response of a material, these matrices are often not very practical to interpret, especially for low-symmetry materials. For instance, anomalous mechanical properties may not be directly clear from inspecting these matrices and it may be cumbersome to predict and visualise the response of a material to a specific deformation based on eqn (3.35), although it contains all necessary ingredients. Therefore, studies on the elastic behaviour of MOFs often report the elastic moduli, such as the bulk modulus K (an isotropic property), the Young's modulus

$E(\boldsymbol{u})$ (the value of which depends on the direction $\boldsymbol{u}$ along which the stress is applied, which coincides with the direction along which the deformation is measured), and the shear modulus $G(\boldsymbol{u},\boldsymbol{v})$ (which depends both on the direction of the applied stress and the orthogonal direction of the deformation measurement). Programs such as ElAM[101] and ELATE[102] form an instrumental tool in this regard, as they allow one to easily visualise these directional elastic *moduli* – as well as the directional Poisson's ratio and linear compressibility – using the elastic *constants* as input. Alternatively, directional moduli can be averaged out to obtain a 'mean' elastic modulus, using either the Voigt (based on the stiffness tensor, assuming a uniform strain[100]), Reuss (based on the compliance tensor, assuming a uniform stress[103]), or Hill (the arithmetic average of the Voigt and Reuss values[104]) averaging schemes. For anisotropic materials, such as most MOFs, however, the usefulness of these average values is limited.

Based on eqn (3.33), the elastic regime of a material – or more precisely, of a given phase of a material – can now be rigorously defined as that region in deformation space for which eqn (3.33) is (approximately) valid; this elastic regime will be the focus of this section. First, in Sections 3.4.1 and 3.4.2, the two main methods to extract elastic constants from a simulation will be discussed, illustrated with examples from MOF literature. Subsequently, in Section 3.4.3, we will focus our attention on how the equilibrium elastic constants can be used to predict whether a MOF is prone to single-crystal-to-single-crystal phase transitions under moderate pressures. In Section 3.4.4, the limits of the elastic regime will be explored to identify under which conditions the material becomes unstable, at which point it enters the inelastic regime discussed in Sections 3.5 and 3.6.

3.4.1 Extracting Elastic Constants Through Explicit Deformations

The most popular method to derive elastic constants starts with considering a set of linearly independent deformation modes and calculating either the energy or the stress of the material strained along this deformation mode. In Section 3.4.1.1, the general methodology behind this approach will be outlined. Given the relatively large body of work on the mechanics of isoreticular MOFs (IRMOFs) and ZIF-like materials, these studies will be used in Sections 3.4.1.2 and 3.4.1.3 to illustrate the different flavours of the explicit deformation approach and how these choices affect the extracted elastic moduli. Afterwards, the UiO-66 family and HKUST-1 will be discussed in Sections 3.4.1.4 and 3.4.1.5, focussing on the importance of taking into account the intrinsic disorder in these materials. Section 3.4.1.6 focuses on the MIL-53/MIL-47 family of wine-rack type materials, given that they exhibit pressure-induced flexibility. Finally, Section 3.4.1.7 provides a brief overview of other MOFs for which elastic constants have been extracted using the explicit deformation approach.

3.4.1.1 General Methodology

The adiabatic elastic constants of a material, $C_{\alpha\beta\gamma\delta} = 1/V_0(\partial^2 U/\partial\varepsilon_{\alpha\beta}\partial\varepsilon_{\gamma\delta})$, can be completely defined using six independent deformation modes, which in turn can be constructed by considering deformations in which all but one of the elements in the strain vector of eqn (3.34) are put to zero. For each deformation mode, the nonzero entry is set to $n\Delta\varepsilon$, where $\Delta\varepsilon$ is a small strain increment and n takes on $2n_{\max} + 1$ different discrete values centred around $n = 0$ (corresponding to the undeformed reference state). Appropriate values of $\Delta\varepsilon$ depend on the system and elastic modulus; for smaller elastic moduli and moduli corresponding to volume-preserving deformations, typically larger increments need to be chosen to ensure the obtained energy difference between the strained and unstrained structure exceeds the computational inaccuracy. A comprehensive example of how the strain increment size and the value of $n_{\max}$ may impact the stiffness tensor of a MOF can be found in ref. 78. For each of the resulting strains $n\Delta\varepsilon$, either the stress or the energy of the system is calculated through a relaxation of the fractional coordinates while keeping the deformed cell matrix fixed. The stiffness tensor **C** is then found by requiring that the imposed strains and the resulting stresses satisfy eqn (3.30) in a least-squares sense or, in the case the energy was measured, that the adiabatic version of eqn (3.33) is satisfied in a least-squares sense.[105] Any excessive remaining error after this fit may indicate that too large a strain increment $\Delta\varepsilon$ was chosen, so that the maximum deformation $n_{\max}\,\Delta\varepsilon$ no longer falls in the elastic regime, or that too small a strain increment was chosen, so that the obtained data is marred by the inaccuracy of the used level of theory. Typically, this boils down to deformations of a few percent. For more symmetric MOFs, such as the cubic IRMOF or UiO-66 series, the number of deformation modes can be reduced given the lower number of independent elastic constants. The basic algorithm outlined here gives rise to *adiabatic* elastic constants, at 0 MPa and at 0 K, although approximate approaches to obtain isothermal elastic constants are also discussed below. In contrast, Sections 3.4.2 and 3.4.4 will focus on dedicated techniques by which to obtain *isothermal* elastic constants at finite temperatures and/or pressures.

In many cases, one is especially interested in the volumetric contraction of the MOF upon a small hydrostatic pressure, as expressed through the bulk modulus K. While the bulk modulus can be determined from the elastic constants calculated above, it can also be calculated directly by considering only one type of deformation, namely a volumetric deformation. In this case, a number of initial structures are prepared with volumes $V = V_0 + n\Delta V$, where V_0 is the reference volume and ΔV is a small volume increment. As before, n takes on discrete values around zero, corresponding to the reference state. Typically, volumes of up to around 10% above and below the equilibrium volume are sampled, with the main criterion being that the elastic regime should be sampled. At each volume, a full optimisation of the nuclear positions and the cell shape is performed, and the final energy is tabulated. From the resulting energy *versus* volume profile, the bulk modulus can then be

obtained by the second-order derivative of the profile around its equilibrium value, as[§§]

$$K = V_0 \left. \frac{\partial^2 E}{\partial V^2} \right|_{V=V_0} \tag{3.36}$$

As this second-order derivative may lead to large inaccuracies, a more appropriate way to extract the bulk modulus from the $E(V)$ profile, is to fit the simulated $E(V)$ data to a known equation of state (EOS), such as the Murnaghan,[106] Birch–Murnaghan,[107] or Rose–Vinet[108] equation of state. In all these equations of state, the bulk modulus (as well as its pressure derivative) appear as fitting parameters. Appropriately fitting the simulated $E(V)$ data therefore yields an alternative way of calculating the bulk modulus and inherently takes into account the anharmonicities described by the EOS, whereas bulk moduli extracted from the elastic stiffness tensor are necessarily harmonic approximations. Furthermore, this fitting procedure has the added benefit that it allows determination of the equilibrium volume without the Pulay effect that mars volume optimisations in plane-wave DFT codes.[109] While all three equations of state are used interchangeably, the Rose–Vinet equation of state has been observed to better describe the response of a solid material upon contraction, and is hence the most appropriate choice, especially when treating flexible MOFs.[109] To account for temperature, the energy E in eqn (3.36) should be replaced by the free energy F, which can be obtained using dedicated simulation techniques, as discussed in Section 3.5.3.

Finally, a last direct approach to calculate the 0 K elastic stiffness tensor $\mathbf{C}$ is by splitting the tensor into two components (in Voigt notation):[110,111]

$$\mathbf{C} = \bar{\mathbf{C}} - \frac{1}{V_0} \mathbf{\Lambda}^T \mathbf{H}^{-} \mathbf{\Lambda}. \tag{3.37}$$

In this expression, $\bar{\mathbf{C}}$ is the Born term (also called the clamped-ion or frozen-ion elastic stiffness tensor): this is the stiffness tensor that is obtained when straining the material *without allowing the ions to equilibrate in this strained unit cell* (*i.e.*, at fixed fractional coordinates, without performing a nuclear optimisation in the above procedure). As this would overestimate the true stiffness of the material, the second term in eqn (3.37), the 'nuclear relaxation term', corrects for this *via* the $3N \times 6$ force-response internal strain tensor $\mathbf{\Lambda}$ and the $3N \times 3N$ Hessian matrix $\mathbf{H}$, both evaluated in the equilibrium configuration and defined component-wise as

$$\Lambda_{ij} = -\frac{\partial^2 U}{\partial x_i \partial \varepsilon_j} = -\frac{\partial \sigma_j}{\partial x_i} \quad \text{and} \quad H_{ij} = \frac{\partial^2 U}{\partial x_i \partial x_j}, \tag{3.38}$$

[§§]The symbol E instead of U will be used here to denote the 0 K (internal) energy of the system, in line with the general nomenclature when discussing equations of state. The reader must not confuse this with the Young's modulus denoted also by symbol E.

where x_i is the ith element of the vector $\boldsymbol{r}^N$ defined in Section 3.2. The eigenmodes and eigenvalues of the Hessian matrix $\mathbf{H}$ define the $3N-3$ vibrational modes of the undeformed periodic system and the associated harmonic frequencies (the three 'missing' eigenvectors correspond to global translations of the periodic system, which have a zero frequency). The force-response internal strain tensor $\mathbf{\Lambda}$ contains derivatives of the energy with respect to both the nuclear displacement x_i and the strain component ε_j, and can be regarded as the off-diagonal elements of an 'extended' or 'generalised' Hessian matrix:[110]

$$\mathbf{H}^{\text{ext}} = \begin{bmatrix} \mathbf{H} & -\mathbf{\Lambda} \\ -\mathbf{\Lambda}^T & \mathbf{V}_0\bar{\mathbf{C}} \end{bmatrix}. \tag{3.39}$$

With these definitions, it is clear that the second term in eqn (3.37) can be interpreted as the product of the transpose of the displacement-response internal strain tensor $\mathbf{\Gamma}^T = \mathbf{\Lambda}^T\mathbf{H}^-$, which describes the first-order displacements resulting from a first-order strain, and the force-response internal strain tensor $\mathbf{\Lambda}$.[110] Both here and in eqn (3.37), $\mathbf{H}^-$ denotes the pseudo-inverse of the Hessian matrix $\mathbf{H}$, as the aforementioned three zero frequency modes precludes one from taking the proper inverse. This 'extended Hessian' approach is only seldomly used for MOFs, given that these materials typically exhibit many low-frequency modes (Section 1.7 of Chapter 1) that are difficult to calculate accurately yet dominate its pseudo-inverse. As a result, the direct calculation of the elastic stiffness tensor is more straightforward in most cases, although the extended Hessian approach does allow partitioning the nuclear part of the elastic constants into different vibrational contributions, as pursued by Maul *et al.* to understand the nuclear origin for shear deformation in ZIF-8.[112]

3.4.1.2 The IRMOF Family

As a first case study, we draw our attention to MOF-5 (IRMOF-1), which is composed of Zn_4O inorganic nodes that are sixfold connected through benzene-1,4-dicarboxylate (BDC) organic ligands (see Figure 3.7(a)).[113] MOF-5 was originally introduced as a very promising material for hydrogen storage, with a hydrogen uptake of up to 4.5 wt% at 78 K.[114] For this purpose, the material should also be stable under (relatively low) mechanical pressures, explaining why MOF-5 and its sister materials in which the BDC ligand is replaced by other dicarboxylate ligands, the IRMOF series, were the first MOFs whose mechanical behaviour was extensively characterised both experimentally and theoretically. As MOF-5 exhibits a cubic conventional unit cell in equilibrium ($Fm\bar{3}m$ space group), its stiffness tensor only features three independent elastic constants: C_{11}, C_{12}, and C_{44}. As a result, its elastic constants can be determined using three independent deformation modes, typically an isotropic contraction (yielding $K = (C_{11} + 2C_{12})/3$), a volume-conserving orthorhombic strain (yielding C_{11}–C_{12}), and a volume-conserving monoclinic shear (yielding C_{44}).[115]

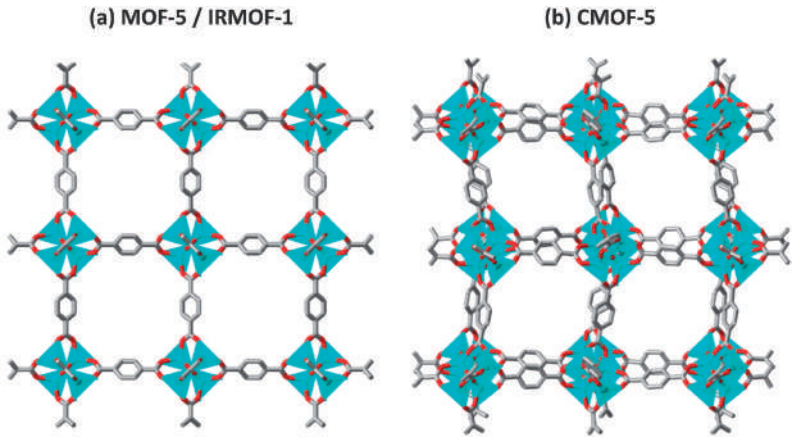

Figure 3.7 Structure of (a) MOF-5 or IRMOF-1 and (b) the Δ enantiomer of chiral MOF-5 (CMOF-5). Hydrogen atoms have been omitted for clarity, ZnO_4 tetrahedra, oxygen atoms, and carbon atoms are coloured blue, red, and grey, respectively. Adapted from ref. 144 with permission from American Chemical Society, Copyright 2016.

The first DFT studies on MOF-5 mechanics consistently revealed a very low C_{44} shear elastic constant. As explored in more detail in Section 3.4.4, this indicates that the material is prone to shear instability. However, the exact value of this constant – and hence the exact point at which the material becomes unstable – depends substantially on the technical aspects of the simulation. While Mattesini *et al.* reported a value of 7.54 GPa using a local density approximation (LDA) of the exchange-correlation functional and a double-zeta atomic-centred basis set,[116] a plane-wave basis set with an LDA functional resulted in a much lower value of 1.4 GPa or 1.16 GPa,[117,118] depending on the implementation code, the size of the basis set, and the size of the sampling grid in reciprocal space. At a higher level of theory, using a generalised gradient approximation (GGA), Bahr *et al.* reported an elastic constant C_{44} of 3.6 GPa.[119] The same variations in magnitude arise for the other two elastic constants, with C_{11} varying between 21.5 GPa and 29.4 GPa and C_{12} varying between 10.6 GPa and 14.8 GPa,[116–119] although the relative importance of these variations is evidently smaller than for the stability-defining C_{44} elastic constant. This first observation immediately emphasises that the impact of technical aspects in these simulations, including the choice of functional, the type of basis (plane wave basis *vs.* atomic-centred basis), the basis set size, the reciprocal sampling grid, and the unit cell size, should be carefully investigated to ensure that convergence has been reached for each of these aspects before calculating the stiffness tensor.[120] To give an idea of the magnitude of such possible deviations, Nazarian *et al.* performed a benchmark study including twelve MOFs and six DFT functionals and observed deviations of up to 20 GPa in elastic moduli depending on the choice of functional.[121]

To obtain a more accurate prediction of the MOF-5 stiffness tensor, Banlusan *et al.*[120] used the Perdew–Burke–Ernzerhof (PBE) functional[122] including Grimme D3 dispersion corrections,[123] which has become a very popular choice to account for long-range dispersion interactions in periodic calculations. In addition, they also used larger triple-zeta valence basis sets including polarisation functions for all elements except for zinc, obtaining results – C_{11} = 25.44 GPa, C_{12} = 10.92, and C_{44} = 1.00 GPa – that are largely in agreement with the aforementioned LDA values. Based on these elastic constants, they also calculated the MOF-5 directional Young's modulus. As illustrated in Figure 3.8(a), the highest Young's modulus in MOF-5, obtained when uniaxially deforming the material along the ⟨100⟩ directions along which the ligands are located, is about 6.5 times larger than its value along the ⟨111⟩ directions, which points along the body diagonal into the MOF-5 cavity.[120]

In their 2007 study, Bahr *et al.* initially aimed to follow the general procedure sketched above to determine the elastic constants.[119] However, the energy *versus* deformation curve they obtained was not sufficiently smooth to extract the elastic constants. They hypothesised that this could be caused by local dynamic effects – *in casu* the rotation of the linker about its symmetry axis – that are not accurately captured by DFT optimisations.[119] While they circumvented this issue by determining the stiffness tensor *via* only a single deformation and calculating the resulting strain, the question remained as to how the increased importance of entropy at higher temperatures would affect the elastic behaviour of MOF-5. Traditional materials, which expand upon heating as covalent bonds tend to expand due to anharmonicities, typically become less rigid at higher temperatures. For MOF-5, which instead shows NTE,[124] this reasoning would predict a hardening of the material at higher temperatures.

To verify this hypothesis, the MOF-5 elastic constants should be calculated at finite temperatures, for instance by performing MD simulations for a series of deformed structures in the $(N,V,\mathbf{h}_0,T)$ ensemble at the target temperature and calculating the time-averaged stress. Given the computational cost associated with these dynamic simulations compared to optimisations,

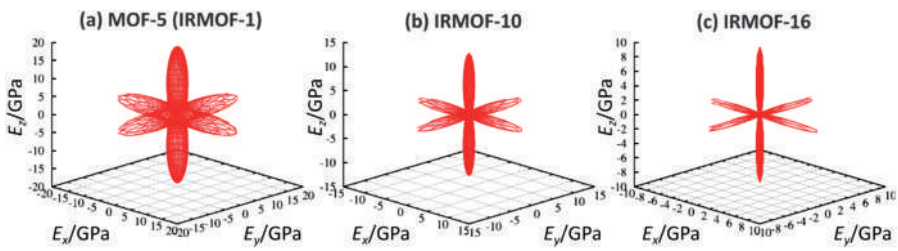

Figure 3.8 Directional 0 K Young's modulus of (a) MOF-5, (b) IRMOF-10, and (c) IRMOF-16 as calculated using the PBE+D3 level of theory. Adapted from ref. 120 with permission from the American Institute of Physics, Copyright 2017.

the first isothermal elastic constants at room temperature were determined using a variety of force fields instead of *ab initio* techniques.[125–129] These simulations confirmed the experimental NTE behaviour of MOF-5, but also predicted the material to become *softer* at higher temperatures despite this NTE. For instance, the generic DREIDING force field[130] predicted a decrease in both C_{11} and C_{44}, from 44.53 GPa to 26.27 GPa and from 1.82 GPa to 1.04 GPa, respectively, when increasing the temperature from 10 K to 600 K, while C_{12} was predicted to increase from 6.79 GPa to 9.83 GPa under the same conditions.[125] Similar decreases in elastic moduli were also predicted using the CVFF force field[131] by Greathouse *et al.*[126] However, the force field values of the elastic constants at 0 K differ appreciably from the ones obtained with DFT mentioned earlier, which was partially explained by Dubbeldam *et al.* as they observed that some of the aforementioned 0 K elastic constants were incorrectly calculated at a stationary point on the PES that does not correspond to a minimum.[129] In addition, it is important to mention that different force fields can give substantially different elastic moduli, even surpassing the deviations between different functionals.[132] When comparing both generic force fields, such as UFF,[133] UFF4MOF,[134] and DREIDING,[130] as well as force fields that were specifically derived to describe MOFs, such as BTW-FF[74] and the one constructed in ref. 135, Boyd *et al.* observed variations in the largest MOF-5 elastic constant, C_{11}, of up to several tens of GPa between these different force fields.[132] This discrepancy can be traced back to the generic character of most of these force fields, or to the fact that they were fitted to experimental data, which makes it difficult to assess their accuracy for different materials.

Therefore, Tafipolsky *et al.* presented a force field specifically derived for MOF-5, starting from a higher-level *ab initio* description of the equilibrium structure and using a genetic algorithm approach that would later be used to generate the MOF-FF library.[127] Using this *ab initio*-derived force field, they obtained 0 K elastic constants amounting to 25.3 GPa, 8.9 GPa, and 2.3 GPa for C_{11}, C_{12}, and C_{44}, respectively. These results are in much closer agreement to the DFT results of Banlusan *et al.*,[120] again demonstrating the importance of using an appropriate and sufficiently accurate level of theory. Furthermore, at 300 K, Tafipolsky *et al.* observed a decrease of 15% and 40% in C_{11} and C_{12}, confirming the reduced stiffness of the material.[127] In 2017, Banlusan *et al.* also calculated the 300 K elastic constants directly *via ab initio* MD, obtaining values of 21.6 GPa, 7.6 GPa, and 0.8 GPa for C_{11}, C_{12}, and C_{44},[120] which coincide well with the 300 K results obtained by an *ab initio*-derived QuickFF force field (22.3 GPa, 8.9 GPa, and 4.0 GPa) except for the shear coefficient C_{44}.[136] Also at 300 K, Banlusan *et al.* observed very large anisotropy in the Young's modulus, which drops significantly upon small deviations from the stiff ⟨100⟩ directions (see Figure 3.9). This observation motivated them to hypothesise that the remaining mismatch between experimentally and theoretically determined elastic moduli in MOF-5 could, at least partially, be explained by small tilts of the crystal during the nanoindentation experiments.[120] In this regard, however, also the potential degradation of the

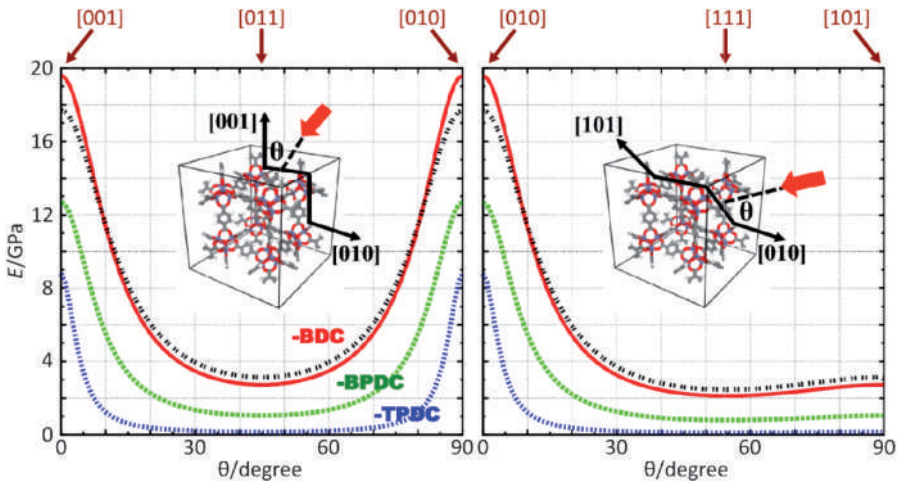

Figure 3.9 Directional 300 K Young's modulus for MOF-5 (red), IRMOF-10 (green), and IRMOF-16 (blue) as a function of the deviation angle (left) from the [001] towards the [010] direction and (right) from the [010] towards the [101] direction, as calculated using the PBE+D3 level of theory. The dashed black lines represent MOF-5 results obtained at a longer simulation time of 5 ps. Adapted from ref. 120 with permission from the American Institute of Physics, Copyright 2017.

moisture-dependent MOF-5 sample during preparation or the nanoindentation experiment should not be neglected,[137,138] which would reduce the stiffness of the material.[139]

Besides MOF-5, a whole series of IRMOF materials have been synthesised that share the MOF-5 architecture but feature a different ligand. Several of these materials have also been the subject of simulation studies to interrogate their equilibrium mechanical behaviour, using either DFT,[120] density functional based tight binding (DFTB),[140] generic force fields,[125,128,141] or system-specific force fields.[78] Adding extra phenyl rings in the BDC ligand leads to the extended biphenyl-4,4′-dicarboxylate (BPDC, IRMOF-10) and terphenyl-4,4″-dicarboxylate (TPDC, IRMOF-16) ligands. As shown in Figure 3.8(b and c), DFT calculations indicate that such linker expansions decrease the stiffness of the material and enhance the anisotropy in elastic moduli.[120] Similar weakening for larger ligands was observed also when using the DFTB framework and with various force fields;[78,125,128,140,141] the only exceptions being hypothetical cage-containing ligands for which the DFTB framework predicts slightly stiffer materials.[140]

In addition to determining the full stiffness tensor, the bulk modulus of MOF-5 and other IRMOF materials have also been widely studied. Given the relative softness of MOFs and the relative ease with which the bulk modulus can be determined, these studies are also widely used to validate new force field and DFTB models that approximate the PES,[74,76,132,142] to compare different equations of state,[143] to study the impact of symmetry,[144] and, at finite

temperatures, to quantify the impact of thermostat and barostat schemes.[83] In 2005, Fuentes-Cabrera *et al.* used an LDA functional to calculate the bulk modulus of different MOF-5 analogues, in which the zinc ions were replaced by either cadmium, beryllium, magnesium, or calcium.[145] They found that the bulk modulus of MOF-5, amounting to around 18.0 GPa, drops when going down the periods in the periodic table; a feature they attributed to the simultaneous increase in porosity and equilibrium volume when incorporating larger cations.[145] This was further investigated in a series of studies by Yang *et al.*[143,146–154] Regarding the effect on the bulk modulus, their work can be summarized in five main points. First, the bulk modulus of IRMOF-type materials is insensitive to the exact form of the equation of state, be it the one proposed by Birch,[107] Birch–Murnaghan,[106] or Rose–Vinet.[108] Second, the aforementioned observation that the bulk modulus decreases when replacing zinc with heavier cations also holds for all alkaline earth metals and for different IRMOF materials, including IRMOF-10,[147] IRMOF-14 (based on pyrene-2,7-dicarboxylate),[148] IRMOF-993 (based on anthracene-9,10-dicarboxylate),[149] IRMOF-M0 (in which the inorganic nodes are directly connected through formate units),[152] and the IRMOF constructed with fumarate ligands.[150] Third, upon increasing the length of the organic ligand and hence the porosity of the material, the bulk modulus decreases. Fourth, when replacing the oxygens in the Zn_4O node with heavier chalcogens, the bulk modulus decreases.[153] Fifth, when fully halogenating the BDC ligand in MOF-5, the bulk modulus decreases for fluorine, but increases systematically when replacing fluorine with chlorine, bromine, or iodine.[154]

In contrast to the full elastic tensor, the MOF-5 bulk modulus is quite insensitive to the level of theory, with 0 K values between 15.5 and 18.2 GPa for different LDA and GGA functionals,[118,145,155] even when including dispersion interactions,[156,157] and between 13.6 and 22.0 GPa for different force fields.[132] Even within the DFTB framework, a similar bulk modulus was found for MOF-5, which decreased when incorporating longer ligands, yielding MOF-177 and MOF-205 (also known as DUT-6).[142] The only somewhat deviating DFT value was reported by Evans and Coudert, who used the PBESOL0 functional[158] and an atom-centred triple-zeta valence and polarisation basis set as implemented in CRYSTAL14[159] to obtain a MOF-5 bulk modulus of 13.5 GPa.[144] Interestingly, they also investigated CMOF-5, a MOF-5 analogue in which chirality is induced by guest adsorption (see Figure 3.7(b)). This lowers the symmetry of the cubic unit cell and also lowers the bulk modulus from 13.5 GPa to 11.1 GPa, showing the importance of choosing a sufficiently large unit cell to investigate MOFs (see Section 3.3.1).

Similar to the elastic constants, Banlusan *et al.* showed through *ab initio* MD (AIMD) simulations that the MOF-5 bulk modulus decreases with increasing temperature, from 15.8 GPa at 0 K to 12.3 GPa at 300 K.[120] Using the CVFF force field description, Greathouse *et al.* overestimated this temperature-induced softening, obtaining a decrease in bulk modulus from 20 GPa to 4 GPa when increasing the temperature from 0 K to 300 K. The latter value was obtained by fitting a Birch–Murnaghan equation of state to the average

energy of an isotropically scaled MOF-5 system that was simulated in the $(N,V,\mathbf{h}_0,T)$ ensemble, which constrained the cubic symmetry.[126] By allowing temporary deviations from this cubic cell shape while constraining the cell volume, Rogge *et al.* obtained a higher bulk modulus of 6.6 to 7.3 GPa at 300 K, depending on the precise barostat implementation.[83] This approach to determine the bulk modulus and, more generally, the full pressure and free energy equation of state of MOFs at finite temperatures is further detailed in Section 3.5.3. A decrease in bulk modulus from *ca*. 15 GPa at 0 K to *ca.* 13 GPa at 350 K – which approaches the AIMD results – was obtained using the quasi-harmonic approximation (QHA) to the free energy.[157] In the QHA framework, anharmonicities in interatomic vibrations or phonon modes, which become more prominent at higher temperatures and are especially present in low-frequency vibrations, are partially taken into account by assuming that the temperature dependence of the vibrational frequencies is completely caused by the temperature-induced change in volume.[160] However, this QHA framework was found to be very sensitive, as an earlier QHA study observed an increase in bulk modulus upon increasing temperature instead.[161]

3.4.1.3 Zeolitic Imidazolate Frameworks (ZIFs) and Associated Materials

Zeolitic imidazolate frameworks (ZIFs) are a subclass of MOFs that, since they are composed of tetrahedrally coordinated cations – typically zinc or cobalt – connected through imidazolate-based ligands, can adopt the same topologies as zeolites.[162,163] Compared to the IRMOF series discussed above, they are chemically and thermally more stable,[163] and are more easily synthesised in the form of single crystals, making them ideal subjects for nanoindentation studies. From a theoretical point of view, ZIF-zni, composed of zinc cations surrounded by imidazolate ligands in a rather dense framework, was the first ZIF for which the bulk modulus was obtained through DFT optimisations, yielding a 0 K bulk modulus of 13.3 GPa.[164] By replacing the zinc cations in ZIF-zni alternatingly with lithium and boron ions, BIF-1(Li) is obtained, for which a slightly higher 0 K bulk modulus of 16.5 GPa was calculated. Both moduli are in excellent agreement with the experimental values of ~14 GPa and ~16.6 GPa collected under ambient conditions.[164]

Tan *et al.* carried out the first full tensorial DFT analysis of a ZIF material by investigating ZIF-8, a cubic material consisting of zinc cations and 2-methylimidazolate ligands that synthesises into the sodalite (**sod**) topology.[165] By adopting the hybrid B3LYP functional[166] using a double-zeta atom-centred basis set, as implemented in CRYSTAL09,[167] they obtained C_{11} = 11.04 GPa, C_{12} = 8.33 GPa, and C_{44} = 0.94 GPa, resulting in a moderately anisotropic material that is most compliant to shear deformations, to an even greater extent than MOF-5.[165] The simulated elastic constants correspond very well with the experimental values of 9.522 GPa, 6.865 GPa, and 0.967 GPa determined *via* Brillouin scattering,[165] in contrast to the larger discrepancies between experiment and simulation for MOF-5 discussed above.

The remaining mismatch between the theoretically and experimentally obtained values was attributed to the absence of thermal effects in the simulations.[165] Very similar elastic constants were obtained using the ZIF-FF force field derived by Weng and Schmidt[168] and the MOF-FF force field derived by Dürholt *et al.*[73] The bulk modulus of 9.23 GPa predicted by Tan *et al.*[165] is also in good agreement with the value of 8.9 GPa obtained by Zhang *et al.* using the hybrid M06-2X functional.[169,170] MAF-7, a ZIF-8 analogue containing 3-methyl-1,2,4-triazolate instead of 2-methylimidazolate ligands (MAF = metal-azolate framework), was found to exhibit higher mechanical resilience than ZIF-8 (K = 10.29 GPa), an effect that was attributed to the electron-donating effect of the additional nitrogen atom in the triazolate ligand.[171] Maul *et al.* established that the elastic constants of ZIF-67, the cobalt analogue of ZIF-8, were very similar to those obtained for ZIF-8.[112] Interestingly, they adopted the extended Hessian approach to determine that only a selected amount of vibrational modes substantially contribute to (the nuclear part of) the ZIF-8 elastic moduli within the harmonic approximation. All identified modes exhibit low frequencies, in the THz regime (see Section 1.7.2 of Chapter 1), being associated with the symmetric gate-opening phenomenon for C_{11} and C_{12}, and with the antisymmetric gate opening phenomenon and breathing deformations of the four-membered ring (4MR) windows for the shear coefficient C_{44}.[112]

Following a similar approach but using the less expensive PBE functional,[122] Tan *et al.* also calculated the elastic tensors of ZIF-4 and ZIF-zni, both composed of zinc cations surrounded by unsubstituted imidazolate ligands, but exhibiting different topologies (**cag** for ZIF-4 *versus* **zni** for ZIF-zni).[172] Similar to ZIF-8, a very good correspondence with the experimental bulk and Young's moduli was obtained.[172] As shown in Figure 3.10, ZIF-zni is more anisotropic than ZIF-4 and ZIF-8, whereas both ZIF-zni and ZIF-4 exhibit greater resistance towards shear deformation than the prototypical ZIF-8 material.[172] Even so, the lowest shear modulus of ZIF-zni, the densest ZIF structure, only lies at ~1.6 GPa, indicating that even dense ZIF materials are prone to shear deformation.[172] Just as other ZIFs that feature 4MR windows, this low shear modulus can be understood by the compliance of the four ZnN_4 tetrahedra surrounding the 4MR windows.[172] In addition, this full tensorial analysis revealed certain directions along which ZIF-4 exhibits (limited) auxetic behaviour, which is uncommon in rigid materials.[172] Using the hybrid B3LYP functional, three more materials with the same composition as ZIF-4 and ZIF-zni were studied in a follow-up study: ZIF-1, ZIF-2, and ZIF-3, exhibiting the **crb** (ZIF-1 and ZIF-2) or **dft** (ZIF-3) topology.[173] Using the hybrid B3LYP functional, Ryder *et al.* observed an almost zero but non-negative Poisson ratio for ZIF-1, ZIF-2, and ZIF-4, whereas ZIF-3 showed both significant auxetic behaviour and an exceptionally low minimum shear modulus of 0.11 GPa, lower than any other ZIF to date.[173] In addition, limited NLC was observed along certain directions in ZIF-1 and ZIF-2.[173] Comparing both studies, it is clear that the choice of exchange-correlation functional impacts the emergence of auxetic behaviour in ZIF-4, and that care should be taken

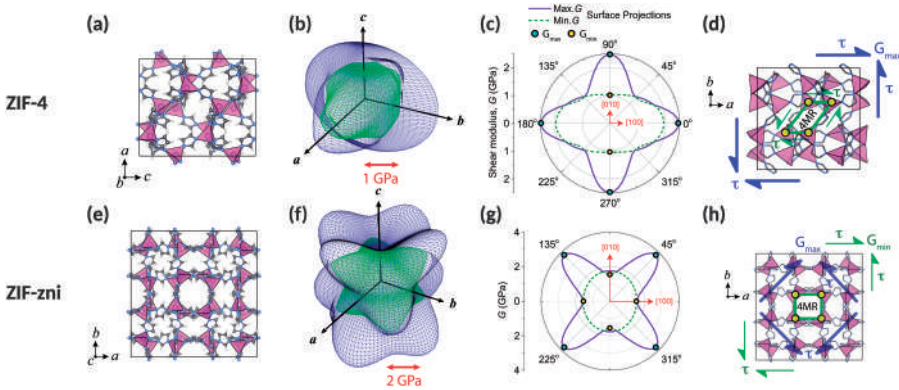

Figure 3.10 Comparison of the directional 0 K shear moduli of ZIF-4 and ZIF-zni calculated at the PBE level of theory. (a and e) Orthorhombic and tetragonal unit cells of ZIF-4 and ZIF-zni, respectively, with ZnN_4 tetrahedra, nitrogen atoms, carbon atoms, and hydrogen atoms indicated in purple, blue, grey, and white, respectively. (b and f) Shear modulus representation surface, where blue and green colour coding denotes the maximum and minimum moduli. (c and g) Polar plots obtained *via* projections through the origin and down the *c* axis, showing the positions of maximum and minimum shear moduli. (d and h) Structure–property relationships illustrating the source of the maximum shear moduli in relation to the position of the 4MR, which has low rigidity against shear deformations. Shear stresses in blue generate G_{max}, while the opposite pairs in green result in G_{min}. Adapted from ref. 172 with permission from the Royal Society of Chemistry.

to ensure that the used level of theory is sufficiently accurate to describe the phenomena under study, as discussed in Section 3.3.2.

The above statement can be further exemplified by the study of Zheng *et al.*, who investigated the elastic constants of five sodalite ZIFs containing zinc cations and either unsubstituted imidazolate (SALEM-2), 2-chloroimidazolate (ZIF-Cl), 2-bromoimidazolate (ZIF-Br), 2-iodoimidazolate (ZIF-I) or imidazolate-2-carboxaldehyde (ZIF-90) as a ligand.[174] Using the PBE functional with dispersion corrections,[122] they found that the mechanical resilience of ZIF-Cl outperformed that of ZIF-Br, which in turn outperformed that of both SALEM-2 and ZIF-90, despite the larger functional group on the ligand of ZIF-90.[174] The authors were able to negatively correlate the magnitude of the elastic constants with the (positive) charge on the zinc cations, which in turn is a function of the electron withdrawing character of the functional group. They hypothesised that the smaller the electron density surrounding the zinc cations, the more flexible the ZnN_4 tetrahedra, and the easier the tetrahedra may deform under stress.[174] Interestingly from a theoretical standpoint, the authors also investigated the effect of the choice of the exchange-correlation functional and the inclusion of dispersion corrections on the reported elastic moduli. While the aforementioned trends were observed for all theoretical models, their absolute magnitude varied by more

than 100%, highlighting the importance of validating and benchmarking these choices.[174] A similar trend was observed by Dürholt *et al.*, *via* both DFT calculations and calculations performed with newly derived MOF-FF force fields.[73] This observed correlation between functionalisation and mechanical stability was generalised by Moosavi *et al.*, who investigated the effect of ligand functionalisation in 50 different ZIF topologies, considering unsubstituted imidazolate, 2-methylimidazolate, 4,5-dichloroimidazolate, and 2-nitroimidazolate as ligands, using a DREIDING-based force field.[130,175] They observed that the nonbonding interactions, which are strengthened by these functional groups, give rise to a secondary network that can impart the material with additional mechanical stability beyond the primary network, defined by the bonding interactions and hence the topology.[175] These functional groups therefore act as 'chemical caryatids' that may strengthen the ZIF structure.

Finally, Zhang *et al.* derived a system-specific force field to determine the bulk modulus of a mixed-matrix membrane (MMM) composed of polybenzimidazole (PBI) and various amounts of ZIF-7 as a filler material.[176] To speed up their calculations, they assumed rigid ZnN_4 tetrahedra, formed from the coordination of the benzimidazolate ligands around the zinc ions in ZIF-7 and only allowed for flexibility in the ligands themselves. They observed that the bulk modulus of neat PBI, amounting to 4.1 GPa, could be substantially increased with increasing ZIF-7 filler content, up to 5.9 GPa for a MMM with 45 wt% of ZIF-7. However, given the exceptionally large value of the pure ZIF-7 bulk modulus they obtained (29.5 GPa) and the observed flexibility of the ZnN_4 tetrahedra in the aforementioned studies, the mechanical properties of this MMM are most likely overestimated by the here imposed constraint that the ZnN_4 tetrahedra are rigid.[176]

3.4.1.4 The UiO-66 Series

The UiO-66 series has been lauded for its exceptional stability compared to other MOFs, a result of its $Zr_6(\mu_3\text{-}OH)_4(\mu_3\text{-}O)_4$ inorganic nodes that are, in its ideal structure, twelvefold connected by either BDC (UiO-66), BPDC (UiO-67), or TPDC (UiO-68) through relatively strong zirconium–oxygen bonds.[45] However, UiO-66 is also one of the first MOFs for which it became apparent that it exhibits tuneable disorder, in which different types and concentrations of defects impact the macroscopic properties of the material, including its mechanical behaviour.[5,29,32] In this respect, the interest in modelling the mechanical properties of UiO-66 lies both in understanding *why* it has such a high mechanical resistance and, especially in more recent years, *how* this is impacted by disorder. As for MOF-5, the conventional cells of the UiO-66 series in equilibrium exhibit cubic symmetry, so that the same three independent deformations can be used to obtain the elastic constants.

As expected given its highly coordinated structure, UiO-66 exhibits high elastic constants, with 0 K elastic constants amounting to 59.4 GPa, 31.9 GPa, and 17.6 GPa for C_{11}, C_{12}, and C_{44}, and a low anisotropy.[177] Wu *et al.*

furthermore observed that replacing the zirconium cations in UiO-66 with either hafnium or titanium cations does not change its 0 K elastic stiffness tensor appreciably.[177] In contrast, increasing the linker length to obtain UiO-67 or UiO-68 does have a profound effect, with the elastic constants and moduli systematically decreasing by about 52–58% for UiO-67 and by about 58–66% for UiO-68.[177] Exchanging the BPDC ligands in UiO-67 with azobenzene-4,4′-dicarboxylate (ABDC) ligands results in a further small decrease in elastic moduli of ~12%.[178] In contrast, exchanging the BDC ligands in UiO-66 by shorter fumarate ligands increases the elastic moduli by ~10%, except for the C_{12} elastic modulus, which decreases by ~20%, presumably due to exchanging an aromatic for an aliphatic ligand.[120] Using system-specific force fields, Moghadam *et al.* generalised these observations for 14 different ligands, obtaining a strong negative correlation between the equilibrium cell length of the UiO-66-type material on the one hand and its elastic constants and elastic moduli on the other hand.[141] Increasing the temperature to 300 K results only in a small decrease in elastic moduli and retains the weak anisotropy in the material.[120]

In the aforementioned studies, UiO-66 and its analogues were treated as defect-free materials, which led to an overestimation of the mechanical stiffness compared to experimental samples that contained ligand and/or node vacancies. To remedy this, Cliffe *et al.* calculated in their landmark study on node defects in UiO-66 the impact of such node vacancies on the elastic constants of UiO-66(Zr) and UiO-66(Hf).[5] While little difference was found between the zirconium and hafnium analogues, the node-defective **reo** materials exhibit *ab initio* elastic moduli that are halved compared to the defect-free **fcu** materials discussed above,[5] clearly demonstrating the importance of correctly accounting for structural defects when modelling UiO-66, as elucidated in Section 3.3.1. Thornton *et al.* further investigated this issue, considering defect-free **fcu** and node-defective **reo** materials, as well as four materials that were obtained from the defect-free structure by systematically removing one, two, three, or four ligands per node, without creating node vacancies.[48] Given that these linker vacancies alter the cubic symmetry of the material (in contrast to the **fcu** and **reo** materials, which are both cubic), six instead of three distinct deformation modes had to be considered in order to characterise all different elastic constants. As illustrated in Figure 3.3, the elastic constants decreased and the anisotropy in elastic moduli increased with an increasing number of linker vacancies, even leading to auxetic behaviour for the most defective structures.[48] Furthermore, they also showed that larger substituents used to cap the vacancy locations, such as acetate and trifluoroacetate, yield elastic moduli that are an order of magnitude larger than smaller substituents such as formate, hydroxyl, or chloride.[48]

As for the elastic constants, the bulk modulus drops significantly upon linker expansion, from K = 37–42 GPa for UiO-66, over 17–22 GPa for UiO-67 and 15–17 GPa for UiO-ABDC, to 14–15 GPa for UiO-68, depending on the DFT level of theory.[177–180] This bulk modulus is quite insensitive to the metal

cation, with similar bulk moduli reported for the zirconium, hafnium, and titanium analogues of these materials.[177,179] The sole exception appears to be UiO-66(Ce), for which a small drop in bulk modulus was observed compared to UiO-66(Zr), from 42 GPa to 37 GPa.[180] From a force-field perspective, Bristow *et al.* reported substantially smaller bulk moduli at 1 K of 27.2 GPa and 19.2 GPa for UiO-66 and UiO-67, respectively.[74] At elevated temperatures, a force-field investigation of the bulk modulus of 14 UiO materials with different ligands demonstrated a decrease in bulk modulus upon increasing linker length, from ~35 GPa for a dicarboxylate linker with a C≡C moiety to ~6 GPa for a dicarboxylate linker with two phenyl rings and two C≡C moieties.[141]

When including node vacancies in UiO-66, the 0 K bulk modulus was observed to decrease from ~39.5 GPa for the defect-free **fcu** material to ~18.3 GPa for the node-defective **reo** material.[5] A very similar decrease was observed when including four ligand vacancies per conventional cubic unit cell instead, although the 0 K bulk modulus is impacted not only by the concentration of ligand vacancies but also by their distribution throughout the framework.[181] Additionally, the dehydrated form of UiO-66 was observed to have a slightly smaller bulk modulus than the hydrated form discussed up to this point.[181] Force-field studies confirmed and generalised these observations to 300 K.[49,182] By considering all inequivalent ways in which one or two ligand vacancies could be distributed throughout the conventional UiO-66 unit cell, Rogge *et al.* observed a decrease in bulk modulus from 22.2 GPa for the defect-free UiO-66 material to 19.9 GPa for UiO-66 in which one out of every 24 ligand positions was vacant.[49] Removing an additional ligand results in a bulk modulus of 15.5–18.9 GPa, depending on the distribution of the two linker vacancies,[49] which coincides with the experimental results obtained by Yot *et al.* with a similar defect concentration.[50] In a combined experimental/theoretical study, the effect of systematically replacing one or multiple zirconium cations in the inorganic node with either hafnium or cerium cations was investigated. Figure 3.11 reveals a negligible effect for hafnium incorporation but a slight decrease in bulk modulus upon cerium incorporation.[182] Finally, node vacancies lead to a distinct drop in 300 K bulk modulus, from 25.5 GPa to 13.9 GPa for UiO-66(Zr),[182] which is somewhat lower than the 0 K results obtained by Cliffe *et al.*[5]

3.4.1.5 HKUST-1

From a mechanical point of view, the cubic HKUST-1 framework, composed of copper paddlewheel units connected through benzene-1,3,5-tricarboxylate (BTC) ligands,[183] shows two distinct changes with respect to the aforementioned MOFs. First, the inorganic nodes are connected through tritopic instead of ditopic ligands, which should impart additional stability to the material. Second, the undercoordinated square-planar copper paddlewheel units in HKUST-1 feature two axial positions to which molecules can adsorb.

Despite being first synthesised in 1999, the first study of the HKUST-1 elastic stiffness tensor only took place in 2010, when Watanabe *et al.* simulated

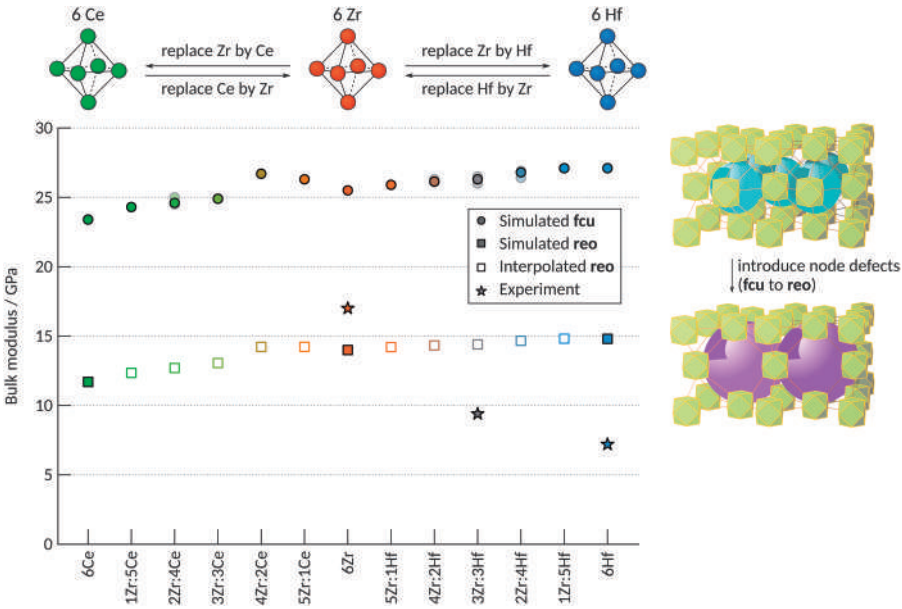

Figure 3.11 Equilibrium bulk moduli at 300 K for a series of bimetallic UiO-66 materials as determined from the pressure equations of state (see Section 3.5.3), both in the pristine **fcu** (circles) and the defective **reo** (squares) topologies, as obtained through force field calculations. For mixed-metal bricks for which two inequivalent bricks can be obtained, the weighted average is shown, whereas the two independent results are included as semi-transparent data points. Experimental results are indicated with stars. Reproduced from ref. 182 with permission from American Chemical Society, Copyright 2020.

its elastic constants within the DFT framework using the PW91 GGA functional.[184] They obtained elastic constants C_{11} = 31.8 GPa, C_{12} = 21.2 GPa, and C_{44} = 12.7 GPa, and a bulk modulus of 24.4 GPa determined *via* a Birch–Murnaghan equation of state.[185] Very similar values were reported by Tafipolsky *et al.*, who derived a MOF-FF force field that could also predict the NTE of the material.[186] While the 0 K bulk modulus was also well reproduced by BTW-FF and more generic force fields,[74,132] DFTB calculations obtained a much larger value of 34.66 GPa,[142] close to the value Zhao *et al.* obtained at 300 K using a newly derived system-specific force field.[187]

The high elastic constants, indicative of a mechanically resistant material, were also calculated using the PBE functional,[122] retrieving good agreement for C_{11} and C_{12} with deviations of up to 20% compared to the aforementioned studies, although a much lower value of C_{44} amounting to 4.41 GPa was found.[177] These latter values were also confirmed independently by Ryder *et al.* using the hybrid B3LYP functional,[166] showing that the inclusion of dispersion corrections has only a minor influence on the elastic stiffness tensor in this case.[188] In addition, they obtained an average difference of less

than 1% between the elastic constants of the ferromagnetic and antiferromagnetic form of HKUST-1.[188] Interestingly, Ryder *et al.* also showed that HKUST-1 exhibits auxetic behaviour, which is most pronounced in the ⟨110⟩ directions upon application of a uniaxial strain in the ⟨1$\bar{1}$0⟩ direction, which could be explained by the theoretically observed low-frequency twisting of the copper paddlewheel clusters shown schematically in Figure 3.12.[188]

In order to probe the structural and mechanical properties of HKUST-1 at longer length scales – and hence to be able to describe the experimentally observed mesopores in the material[34] – Dürholt *et al.* developed the first coarse-grained MOF force field that builds upon their earlier MOF-FF framework.[7] In their coarsest HKUST-1 model, the ⟨100⟩ Young's modulus and bulk modulus were found to be 20.3 GPa and 17.6 GPa, respectively, comparable with the values of 23.8 GPa and 19.6 GPa obtained using an atomistic MOF-FF force field.[7] In addition, they found that the inclusion of nonbonded interactions, *i.e.*, van der Waals and Coulomb interactions, did not alter these values appreciably, and that a hypothetical HKUST-1 material that adopts the **pto** topology would be about 20–40% more rigid than the experimentally observed **tbo** topology, although the latter is energetically more favourable.[7] This coarse-grained force field was then adopted in a multiscale investigation to determine the 0 K bulk modulus of defective HKUST-1 samples, in which spherical mesopores of different sizes and with different concentrations were created.[23] As expected, increasing the mesopore volume

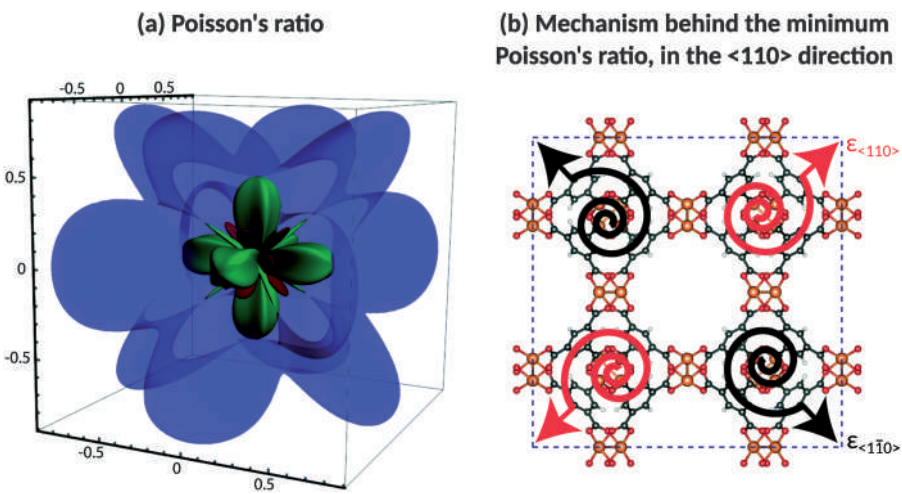

Figure 3.12 (a) 0 K Poisson's ratio representation surface obtained at the B3LYP-D level of theory, where blue signifies the maximum Poisson's ratio and green and red denote the positive and negative (= auxetic behaviour) minimum Poisson's ratios, respectively. (b) Demonstration of the plausible mechanism associated with cluster rotational dynamics responsible for the auxetic response. Adapted from ref. 188 with permission from the Royal Society of Chemistry.

leads to a continuous decrease in bulk modulus, although the decrease in bulk modulus remains modest.[23] Interestingly, Dürholt *et al.* observed that many smaller mesopores in the material impact the bulk modulus more strongly than one larger mesopore with the same total mesopore volume,[23] an important guideline when designing defect-engineered MOFs.

3.4.1.6 Wine-Rack Type MOFs: MIL-47 and MIL-53-type Materials

Wine-rack type MOFs are composed of extended one-dimensional inorganic chains that are connected through dicarboxylate ligands, in such a way that their structure viewed along the 1D chain resembles that of a wine rack (Figure 1.1(e)). The most prominent examples of this family are the MIL-47 and the MIL-53 series,[189,190] which can be synthesised with different metal cations. Because of their wine rack structure, these materials can undergo large-amplitude phase transitions between a large-pore (lp) and closed-pore (cp) structure, so-called 'breathing', induced by mechanical stress,[191,192] among other external stimuli,[193] and feature NLC, NTE, and auxeticity (Chapter 2).[1,194,195] Since these MOFs have a lower symmetry than the MOFs mentioned before, they exhibit more independent elastic constants and hence more independent deformations are needed to fully characterise their elastic tensor.

A full tensorial analysis of the elastic tensors of the lp structures of MIL-53(Al), MIL-53(Ga), and MIL-47 was first reported by Ortiz *et al.*[196] using the B3LYP functional.[166] The nine elastic constants for these orthorhombic structures are reproduced in Table 3.2, while Figure 3.13 visualises the resulting directional Young's modulus of the lp structures of MIL-53(Al) and MIL-47.[196,197] This visualisation shows very strong anisotropy, with stiffer directions along the inorganic chains and the organic ligands, and very compliant directions along the diagonals of the lozenge-shaped pore.[196] As discussed further in Section 3.4.3, this strong anisotropy in Young's modulus and other elastic moduli was posited as a revealing signature of structural flexibility in MOFs.[196] In addition, Ortiz *et al.* showed that all investigated MIL-53 and MIL-47 materials exhibit NLC along a direction pointing into the channel, with a magnitude of up to −257 TPa^{-1} for MIL-53(Al) lp.[196] Finally,

Table 3.2 0 K stiffness constants for five wine-rack type materials in Voigt notation, obtained at the B3LYP level of theory. Reproduced from ref. 196 with permission from the American Physical Society, Copyright 2012.

C_{ij}/GPa	C_{11}	C_{22}	C_{33}	C_{44}	C_{55}	C_{66}	C_{12}	C_{13}	C_{23}
MIL-53(Al) lp	90.85	65.56	33.33	7.24	39.52	8.27	20.41	54.28	12.36
MIL-53(Ga) lp	112.32	56.66	18.52	5.45	21.71	6.64	22.87	45.35	10.86
MIL-47 lp	40.68	62.60	36.15	50.83	7.76	9.30	12.58	9.28	46.98
DMOF-1 loz	57.15	35.59	17.68	0.62	16.39	0.69	9.85	31.43	5.47
DMOF-1 sq	35.33	58.20	58.45	0.11	0.44	0.28	7.32	7.55	11.68

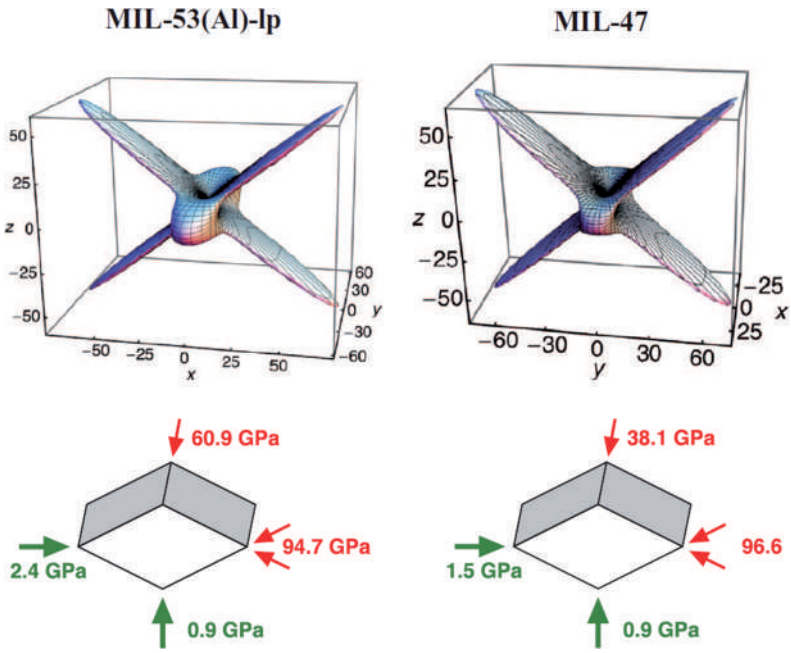

Figure 3.13 Top: Directional 0 K Young's modulus for the lp phases of MIL-53(Al) (left) and MIL-47 (right) represented as 3D surfaces, with axes tick labels in GPa. Bottom: Scheme of the Young's modulus values for the stiffest and most compliant directions, with Young's modulus values indicated. Reproduced from ref. 197 with permission from the American Institute of Physics, Copyright 2013.

they reported that the bulk modulus calculated from these elastic constants depends on the averaging scheme, in contrast to the less anisotropic MOFs discussed before,[196] with values between 1 and 20 GPa for the MOFs considered here. In line with earlier results on rigid MOFs, DFTB strongly overestimates the true bulk modulus also for MIL-53.[142] For MIL-47(V), similar elastic constants as those reported in Table 3.2 were obtained by Vanpoucke *et al.* and Heinen *et al.* using the generalised Hessian approach.[78,109] As noted earlier for MOF-5, Vanpoucke *et al.* also observed that a proper energy minimisation is essential to obtain the true unstrained equilibrium structure and its elastic constants.[109] The MIL-47 *ab initio* elastic constants from the three aforementioned studies were used by Heinen *et al.* to propose an alternative force field fitting procedure based on the elastic stiffness tensor.[78] The elastic constants predicted using this MIL-47 force field correspond remarkably well with those obtained from DFT calculations,[78] in contrast to more *ad hoc* based force fields.[191] Heinen *et al.* furthermore observed that amino functionalising the BDC ligands in MIL-47 leads, on average, to a decrease in elastic constants, although the exact magnitude of the elastic constants depends on the location of the amino group, with the most stable amino-functionalised

structures being those with the highest elastic constants.[198] Finally, also the fumarate-based analogues of MIL-53(Al) and MIL-53(Ga) were studied at the DFT level using the PBE functional,[122] showing that the gallium analogue is softer than the aluminium variant.[199]

Regarding the cp phases, DFT calculations using the PBE functional[122] reveal that the MIL-53(Al) cp structure exhibits a lower anisotropy in Young's and shear moduli compared to its lp structure, although it still features directions of NLC and auxetic response.[200] A similar result was obtained for fumarate-based MIL-53(Al) and MIL-53(Ga).[199] Furthermore, it was observed that low water loadings in the MIL-53(Al) lp structure soften some of the deformation modes of the material,[200] a counterintuitive response upon adsorption that was observed earlier by Mouhat *et al.*[201] A similar effect was observed at 300 K for MIL-53(Cr), where a force-field study showed a decrease in bulk modulus from ~1.8 GPa to ~0.75 GPa at low CO_2 loading.[202] For MIL-47, the cp structure was found to exhibit both directions of NLC and of auxetic behaviour.[109] In addition, the MIL-47 cp structure shows higher anisotropy in Young's modulus and a lower anisotropy in shear modulus than its lp structure.[109] While DFT predicts its 0 K bulk modulus to decrease from 6.1 GPa to 2.8 GPa when transitioning from the lp to the cp structure,[109] a force field study predicts that MIL-53(Al) does the opposite, with an increase in 300 K bulk modulus from ~1.6 GPa to ~3.7 GPa when transitioning to the denser structure.[83] A similar increase in bulk modulus for the denser phase was observed for COMOC-2,[203] an isoreticularly expanded version of MIL-47 in which the BDC ligands are replaced by BPDC ligands.[204] Additionally, Wieme *et al.* observed a decrease in bulk modulus for the COMOC-2 cp state and an increase for the COMOC-2 lp state with increasing temperature, whereas the bulk moduli of MIL-47 and COMOC-3 (obtained by replacing the BDC ligand in MIL-47 by a naphthalene-2,6-dicarboxylate (NDC) ligand) are largely temperature-independent.[204] The MIL-47 bulk modulus furthermore depends on the magnetic ordering of the vanadium ions in the inorganic chain, with antiferromagnetic chains leading to bulk moduli that are ~2 GPa larger than for ferromagnetic chains.[205] Finally, Hoffman *et al.* observed only a modest decrease in bulk modulus with temperature for the MIL-53(Al) cp phase within the QHA framework, while a much larger increase in bulk modulus was observed for the lp phase, from 2.1 GPa at 0 K to 8.4 GPa at 500 K.[206] The latter effect, however, was assigned to an overestimation of the thermal expansion behaviour of the lp phase in this study.[206] For both phases, they were able to pinpoint the magnitude of the bulk modulus to a limited set of low-frequency vibrational modes (see Figure 1.19).[206]

In a follow-up study,[197] Ortiz *et al.* compared the behaviour observed for MIL-53 and MIL-47 to that of two other wine-rack type MOFs, MIL-122[207] and MIL-140.[208] MIL-122 is structurally similar to MIL-53, with the exception that the ditopic BDC ligands in MIL-53 are replaced by tetratopic naphthalene-1,4,5,8-tetracarboxylate ligands, which precludes wine-rack type hinging. While MIL-122 was observed to still exhibit auxetic behaviour and directions of NLC, a feature of wine-rack type MOFs, the anisotropy

in its Young's modulus is about two orders of magnitude smaller than for the flexible MIL-53 and MIL-47 materials.[197] The zirconium-based MIL-140 material, in turn, can be regarded as a 'reinforced' or 'retrofitted' wine-rack structure, which features additional linkers that span the pores, hence again precluding flexibility. Although MIL-140 does exhibit strong anisotropy in its Young's and shear moduli, the most compliant directions are not located along the pores and hence predict that the material is not flexible.[197] While Ortiz *et al.* did not observe any directions with NLC,[197] Ryder *et al.* observed NLC directions both in MIL-140, albeit rather of limited magnitude, and an isoreticular framework with a BPDC ligand.[209] By systematically increasing the length of the ligand, they observed a continuous increase in anisotropy for the elastic moduli of these materials as well as a continuous increase in auxetic behaviour and a continuous decrease in bulk modulus.[209] However, no such correlation was observed regarding the occurrence of NLC and the shape of the linear compressibility representation surface in general.[209] Furthermore, as for the MIL-53 materials, it was noted that the bulk modulus calculated from the elastic constants is dependent on the chosen averaging scheme.[209]

3.4.1.7 Other Systematic Observations in MOF Mechanics

Alongside the prototypical MOFs given above, several other studies have appeared in recent years in which the elastic constants or moduli of MOFs have been determined. Noteworthy examples include 2D MOFs such as MOF-901 (the most compliant directions of which are located in the direction perpendicular to the 2D planes),[210] MOFs with differing degrees of interpenetration, such as in the MOF-14/DUT-34 pair of structures (where interpenetration increases the mechanical stability),[211] thin film SURMOFs,[212] flexible 3D MOFs such as ZnPurBr,[213] DUT-49,[214] DMOF-1,[215] ZAG-4,[216] ZAG-6,[216] CoBDP,[217] and others.[218] While it is impossible to discuss them exhaustively here, two systematic sets of 'high-throughput' studies have appeared in recent years that warrant a more in-depth discussion.

In 2019, Alexandrov *et al.* performed a comparative DFT study of 22 MOFs assembled from chain-like inorganic building blocks and calculated their full stiffness tensor.[219] They observed that many of these MOFs exhibit both NLC and auxetic behaviour, even though not all of them were flexible.[219] This work generalises earlier observations of such anomalous behaviour in rod-like MOFs,[220] such as the MIL-47 and MIL-53 series discussed in Section 3.4.1.6, ZAG-4 (which shows NLC but no auxetic behaviour),[216] ZAG-6,[216] SION-8,[221] CoBDP,[217] the lozenge-pore phase of DMOF-1 (although a similar effect is missing in its square-pore structure),[196] MOF-74(Zn),[222] and its analogue with a shorter 2,3-dihydroxyfumarate (which shows auxetic behaviour but no NLC),[223] CAU-13,[224] and NOTT-300 (which shows auxetic behaviour but no NLC).[224] Based on this anomalous behaviour, CAU-13 and NOTT-300 were predicted to be flexible,[224] which was later confirmed experimentally for CAU-13.[225]

On a larger scale, Anderson *et al.* constructed a library of 122 copper-paddlewheel MOFs, focusing on how their mechanical properties are altered as a function of their organic ligands and the topology in which the material assembles.[226] 19 different topologies were included in this study, as it was observed that previous high-throughput studies lacked diversity in this aspect. This path was further explored by Moghadam *et al.*, who constructed a database of 3385 MOFs consisting of 41 different topologies and various types of organic and inorganic building blocks, making it the largest MOF database up to this point for which the mechanical properties have been fully calculated.[141] Given the size of these databases, they were explored using the UFF4MOF force field with the aim of understanding what makes certain MOFs more robust than others.[134] Both studies revealed the topology of the material to be the most important predictor of its mechanical properties,[141,226] to the extent that a neural network could not satisfactorily predict the mechanical behaviour of MOFs without considering topology as a feature.[141] Additionally, these studies revealed that MOFs tend to become more compliant when they exhibit low-connected inorganic nodes or when the size of the organic ligand increases,[141,226] in line with the observation that the densest MOFs are also the most mechanically rigid.[139,227] Efforts to discover mechanically stable MOFs with exceptional internal surface areas therefore need to find building blocks and topologies that balance these two aspects, such as found in the recently synthesised DUT-60 framework that adopts the less common **ith-d** topology.[228]

3.4.2 Extracting Elastic Constants Through Fluctuation Formulae to Predict Temperature Effects

Most mechanical studies on MOFs in the elastic regime use the explicit deformation methodology outlined in Section 3.4.1. However, the elastic constants derived using the relation $V_0 C_{ij} = \partial^2 U / \partial \varepsilon_i \partial \varepsilon_j$ are obtained at 0 K, whereas the mechanical properties of MOFs are strongly temperature dependent. An extension of the explicit deformation methodology to finite temperature is, in principle, possible by replacing the internal energy U by the Helmholtz free energy F, but obtaining the free energy from a simulation requires dedicated simulation protocols, as explained in Section 3.5.3, and is therefore not straightforward. The same limitation arises for the energy equation of state: to obtain the finite-temperature bulk modulus, the *free* energy equation of state should be constructed. In Section 3.4.2.1, an alternative approach based on fluctuation formulae will be outlined from which the finite-temperature elastic stiffness tensor can be obtained. Its application to MOF research will be discussed in Section 3.4.2.2. Given that this methodology requires taking appropriate ensemble averages, it is computationally more expensive than the explicit deformation approach, explaining the rather limited MOF literature on the topic and the focus on force field rather than DFT studies.

3.4.2.1 General Methodology

Two main types of fluctuation formula arise, which differ in whether the stress is imposed and variations in strain are measured, or whether the strain is imposed and variations in stress are measured. Also mixed forms exist, but are not discussed here as they have not yet been used in MOF research. For the first category, Parrinello and Rahman showed that the elements of the fourth-rank compliance tensor **S** of a material around an equilibrium structure with volume V_0 and at a temperature T can be obtained as:[229]

$$S_{\alpha\beta\mu\nu} = \frac{V_0}{k_B T}\left\langle \Delta\varepsilon_{\alpha\beta}\Delta\varepsilon_{\mu\nu}\right\rangle = \frac{V_0}{k_B T}\left(\left\langle \varepsilon_{\alpha\beta}\varepsilon_{\mu\nu}\right\rangle - \left\langle \varepsilon_{\alpha\beta}\right\rangle\left\langle \varepsilon_{\mu\nu}\right\rangle\right). \quad (3.40)$$

In this expression, $\langle\cdot\rangle$ denotes an ensemble average. When this average is taken in the (N, P, $\boldsymbol{\sigma}_a$, H) ensemble, the adiabatic compliance tensor is obtained, whereas taking the average in the (N, P, $\boldsymbol{\sigma}_a$, T) ensemble leads to the isothermal compliance tensor.[229] The corresponding stiffness tensor then follows through matrix inversion. This formula can be extended to also calculate higher-order stiffness tensors.[230]

For the second category, Squire *et al.* and Ray *et al.* showed that a material's fourth-rank stiffness tensor **C** around an equilibrium structure with volume V_0 and at a temperature T can be obtained as:[15,231,232]

$$C_{\alpha\beta\mu\nu} = \left\langle \bar{C}_{\alpha\beta\mu\nu}\right\rangle - \frac{V_0}{k_B T}\left(\left\langle \sigma_{\alpha\beta}\sigma_{\mu\nu}\right\rangle - \left\langle \sigma_{\alpha\beta}\right\rangle\left\langle \sigma_{\mu\nu}\right\rangle\right) + \frac{2Nk_B T}{V_0}\left(\delta_{\alpha\nu}\delta_{\beta\mu} + \delta_{\alpha\mu}\delta_{\beta\nu}\right). \quad (3.41)$$

In this expression, where the notation of ref. 111 is used, δ_{ij} is the Kronecker delta, being one if $i = j$ and zero otherwise. $\bar{C}_{\alpha\beta\mu\nu}$ is the Born term, which was first encountered in eqn (3.37). The second and third terms are the fluctuation term, which converges to the relaxation term in eqn (3.37) in the zero temperature (0 K) limit, and the ideal gas term, which vanishes in the same limit.[233] The ensemble over which the average is taken again determines which elastic tensor is calculated: the (N, V, $\mathbf{h}_0$, E) ensemble yields the adiabatic stiffness tensor, whereas the (N, V, $\mathbf{h}_0$, T) ensemble yields the isothermal stiffness tensor.[15,231,232]

While both eqn (3.40) and (3.41) can be used interchangeably to determine the elastic constants, they differ from a practical perspective. First, eqn (3.40) requires pressure control during the simulation, and as a result the barostat simulation parameters may impact the observed fluctuations, as discussed in Sections 3.3.3 and 3.5.1. This was illustrated in ref. 83, in which the 300 K bulk modulus of MIL-53(Al) was determined based on fluctuations in the unit cell volume, similar to eqn (3.40). For the Langevin and MTK barostats, bulk moduli of 8.5–12.1 GPa for the cp phase and 3.2–10.1 GPa for the lp phase were predicted.[83] Those variations were caused only by a variation in coupling strength between the barostat and the system, as the barostat relaxation time was varied between 1 ps and 10 ps.[83] This effect was two orders of magnitude worse for the Berendsen barostat, where the same procedure led to bulk moduli of 275–1150 GPa (cp phase) and 93–215 GPa (lp phase) due

to the artificial suppression of volume fluctuations in this barostat coupling scheme.[83] Second, eqn (3.40) was observed to converge more slowly than eqn (3.41),[82] although this argument is less important for force-field based simulations. The main disadvantage of eqn (3.41) lies in the Born term, which requires calculating the second-order derivatives of the potential energy with respect to the strain along the simulation to calculate the first term. While first-order derivatives of the potential energy are readily available in molecular software as they determine the forces on the system, this is often not the case for second-order derivatives which quickly become very intricate (see ref. 129, 233, and 234 for examples).

3.4.2.2 Application to MOFs

A first study of the temperature-dependent elastic properties of MOFs was performed for the cubic ZIF-8 material by Ortiz *et al.*, showing an increase in C_{11} when increasing the temperature from 77 K to 500 K, while the C_{12} and C_{44} elastic constants, the last of which determines the most compliant deformation mode in ZIF-8, were largely temperature-independent.[235] Despite the ZIF-FF force field showing an overall good agreement with *ab initio* data, it could not reproduce this temperature-induced increase in C_{11}.[168] Ying *et al.* used eqn (3.40) to predict the effect of linker functionalisation in ZIF-8 on its 300 K shear elastic constant C_{44}, showing that C_{44} is smaller for ZIF-Cl and ZIF-Br than for ZIF-8, while it is larger in SALEM-2.[236] In comparison, the bulk modulus was found to increase from SALEM-2 over ZIF-8 and ZIF-Cl to ZIF-Br,[236,237] in contrast to earlier observations obtained at 0 K.[73,174] In contrast to the temperature-induced stiffening in ZIF-8, the three elastic constants of HKUST-1 were predicted to decrease when increasing the temperature from 0 K to 400 K, as shown in the inset of Figure 3.14, thereby lowering the structural stability of the material.[238] These theoretical predictions of temperature-induced softening in HKUST-1 were confirmed by the nanoindentation experiments illustrated in Figure 3.14.[238]

A comparative study of the elastic moduli in UiO-66, MOF-5, MIL-47, and the two phases of MIL-53 demonstrated that the impact of temperature on the elastic moduli is strongly material dependent.[136] For UiO-66, the maximum Young's and shear moduli were predicted to increase with temperature, while their minimum values decreased slightly, thereby increasing the anisotropy with increasing temperature.[136] For MOF-5, only the minimum shear modulus was found to decrease appreciably upon increasing temperature, making the material even less stable, whereas other elastic moduli were found to remain more or less constant, thereby reducing the anisotropy with increasing temperature.[136] For the lp phases of MIL-47 and MIL-53, an increase in maximum values of the Young's and shear moduli were obtained with increasing temperature, whereas the minimum values either remained more or less constant (for MIL-47) or decreased (for MIL-53), in both cases leading to an increase in anisotropy.[136] Finally, for the MIL-53 cp phase, a mixed picture was obtained where the minimum Young's modulus,

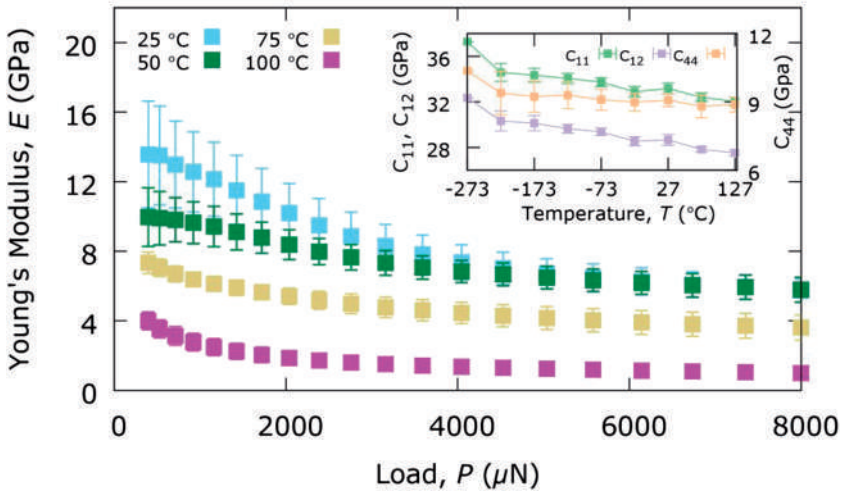

Figure 3.14 Young's modulus as a function of load at various temperatures obtained from nanoindentation experiments. Inset: Variable-temperature elastic constants obtained from classical molecular dynamics simulations. Lines provide guidance for the eye. Adapted from ref. 238 with permission from American Chemical Society, Copyright 2018.

the maximum Young's modulus and the minimum shear modulus increased with temperature, whereas the other values remained constant, leading to a net decrease in anisotropy for these two elastic moduli upon an increase in temperature.[136]

In two force field studies, Ying *et al.* used the strain fluctuation formula of eqn (3.40) to calculate the 300 K elastic moduli of DUT-49 and four isoreticular analogues obtained by changing the organic ligand.[237,239] In agreement with earlier 0 K observations discussed in Section 3.4.1, they found that longer ligands decrease the magnitude of all 300 K moduli, both in the open-pore (op) and cp phase, as shown in Figure 3.15.[237,239] In addition, Figure 3.15 reveals that the cp phase exhibits lower elastic moduli than the op phase for all investigated DUT materials.[239] Finally, a full elastic tensorial analysis of eleven $Zn(CN)_2$ polymorphs revealed auxetic behaviour in all these structures, although only one also showed NLC.[240]

3.4.3 Predicting Flexibility from Equilibrium Elastic Properties

Up to this point, we have been interested in characterising the elastic regime of MOFs, determined through the second-order elastic stiffness tensor. Based on the derivation in eqn (3.33), this limits the region for which the properties and observations in Sections 3.4.1 and 3.4.2 hold to small strains around an

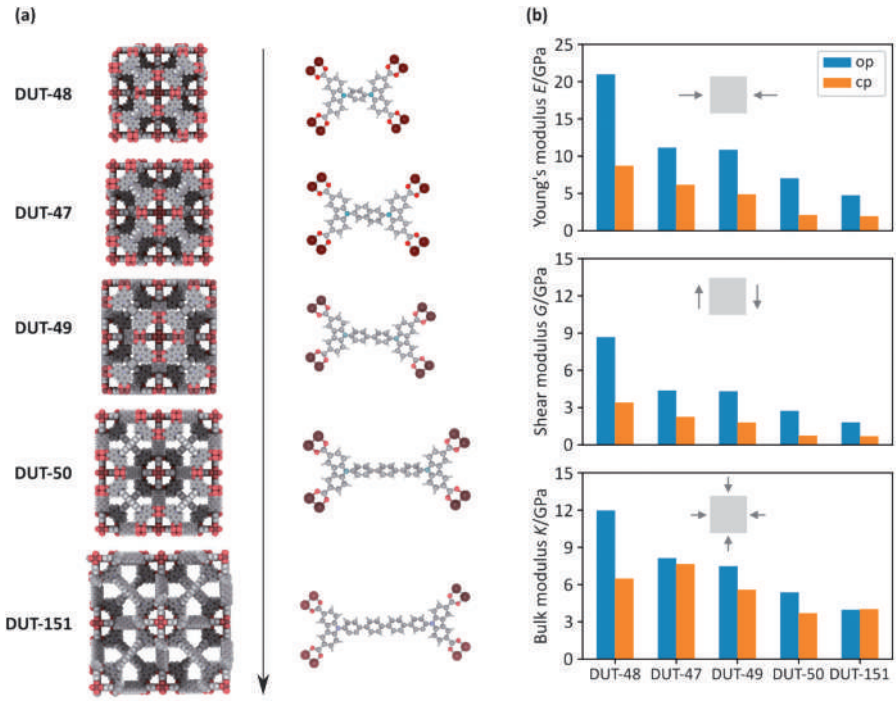

Figure 3.15 (a) Atomic structures of five isoreticular DUT materials with increasing ligand length. Copper, oxygen, nitrogen, carbon, and hydrogen atoms are shown in brown, red, cyan, grey, and white, respectively. (b) Averaged Young's, shear, and bulk moduli for these five materials in both the op (blue) and cp (orange) phase. The insets show the deformation mode corresponding to each modulus. Adapted from ref. 239 with permission from American Chemical Society, Copyright 2021.

equilibrium structure of the MOF, either at 0 K or at elevated temperatures. It is only natural, however, to ponder to which extent these elastic properties can be correlated with 'plastic' mechanical properties (exceeding the elastic limit) – for instance, in how far can elastic constants distinguish between flexible materials, exhibiting a single-crystal-to-single-crystal phase transition under plastic deformation, and rigid materials, exhibiting a single-crystal-to-amorphous phase transition instead? Finding such correlations would be very powerful, both from an experimental and a theoretical perspective. Experimentally, such correlations would circumvent the need to perform destructive tests to establish the plastic behaviour of a material. Theoretically, it is often far easier to describe the equilibrium structure of a material rather than its structure during plastic deformation, as discussed in Sections 3.5 and 3.6.

Empirically, Zener found that the anisotropy index $A = 2C_{44}/(C_{11} - C_{12})$, which is the ratio of the resistance of a cubic material against monoclinic shear to its resistance to an orthorhombic shear, is an important quantity by

which to predict mechanical processes in metals beyond the elastic regime.[241] This Zener anisotropy index forms a signature for phase transformations in alloys and for plastic anisotropy in sheet metals: the higher the anisotropy, the less energetically costly the phase transformation becomes.[242,243] The question remains, however, if a similar measure can also be introduced for MOFs, which often exhibit noncubic structures.

In this regard, Ortiz *et al.* systematically calculated the 0 K elastic moduli of the flexible MIL-53, MIL-47, and DMOF-1 materials, and observed that the ratio of the maximum and minimum Young's modulus, as well as the ratio of the maximum and minimum shear modulus, is about two orders of magnitude higher for these flexible MOFs than for relatively rigid MOFs such as MOF-5 and ZIF-8.[196] This motivated them to conclude that high anisotropy in these moduli, and hence the presence of directions with rather low Young's and shear moduli, is an indicator for structural flexibility in MOFs – hence predicting their plastic behaviour.[196] Later, they noted that the occurrence of such 'soft' deformations modes along which the material can deform with only a small energy penalty can also be directly extracted by determining the eigenvalues and eigenmodes of the stiffness tensor **C**, as the eigenmode with the lowest eigenvalue describes the softest deformation mode of the material.[197] Their elastic signature for flexibility in MOFs can therefore be more generally expressed as the simultaneous occurrence of soft deformation modes and large anisotropy in eigenvalues of the elastic stiffness tensor.[197] Although they recognised that this signature should be used with caution – counterexamples were found in the rigid MIL-140,[197] which shows unexpectedly high anisotropy, and in a series of flexible DUT-49 analogues, which show unexpectedly low anisotropy[237] – this criterion remains to date a convenient criterion to check for flexibility in MOFs based on their computed equilibrium properties, both at 0 K and at finite temperatures.[136,216] When a material is brought closer to instability, its anisotropy was furthermore observed to increase substantially.[136] In 2014, Sarkisov *et al.* demonstrated that soft deformation modes in a material, and hence large-amplitude flexibility, could also be predicted by representing the MOF as a mechanical model constructed from rigid trusses that are connected through flexible hinges (Section 2.4.5).[244] The flexibility of this mechanical model and hence the associated MOF, can then be predicted by considering the energy needed to deform the model under various deformation modes.[244]

3.4.4 Determining the Stability Range of MOFs: Elasticity Under Pressure

Predicting the thermodynamic conditions – temperature, stress, adsorption – under which a certain phase of a MOF is stable is essential in order to know how these MOFs can be shaped and handled, as well as for which applications they can be adopted. This can be directly achieved by modelling the material outside of its elastic equilibrium, which is the topic of Sections 3.5 and 3.6. In contrast, herein two main methods will be outlined to determine

the stability of MOFs – focussing on their 'mechanical stability' – based on properties derived in the *elastic* regime: either the elastic stiffness tensor (Section 3.4.4.1) or the vibrational modes (Section 3.4.4.2).

To do so, however, it is first necessary to generalise the definition of the stiffness tensor of eqn (3.33) to account for finite pressures. Recall that finite temperatures are already taken care of in eqn (3.33), given that the elastic tensor is therein defined based on the Helmholtz free energy F. At a finite stress $\boldsymbol{\sigma}$, the Helmholtz free energy of eqn (3.33) should be replaced by the Gibbs free energy G, defined in eqn (3.6) for a general stress and in eqn (3.19) for a hydrostatic pressure.[245] As a result, the first-order expansion coefficients in eqn (3.31) will no longer disappear at finite stress, and the unloaded elastic stiffness tensor $\mathbf{C}$ should be replaced by the elastic stiffness tensor $\mathbf{B}$ under a load $\boldsymbol{\sigma}$, defined component-wise as:[246,247,¶¶]

$$B_{ijkl} = C_{ijkl} + \frac{1}{2}\left(\sigma_{ik}\delta_{jl} + \sigma_{il}\delta_{jk} + \sigma_{jk}\delta_{il} + \sigma_{jl}\delta_{ik} - 2\sigma_{ij}\delta_{kl}\right). \tag{3.42}$$

In general, $B_{klij} \neq B_{ijkl}$ due to the last term between brackets in eqn (3.42). Hence, the *loaded* elastic stiffness tensor $\mathbf{B}$ has, in general, a lower symmetry than the *unloaded* elastic stiffness tensor $\mathbf{C}$. As a result, also the Voigt notation cannot be used in this case. Under a hydrostatic pressure $\sigma_{ij} = -P\delta_{ij}$, eqn (3.42) simplifies to

$$B_{ijkl} = C_{ijkl} - P(\delta_{ik}\delta_{jl} + \delta_{il}\delta_{jk} - \delta_{ij}\delta_{kl}), \tag{3.43}$$

and the Voigt symmetry of $\mathbf{C}$ is preserved.[246–248]

From a practical perspective, one can hence determine the loaded elastic stiffness tensor $\mathbf{B}$ at a given temperature and stress by first determining the unloaded elastic stiffness tensor $\mathbf{C}$ under the same conditions and then applying eqn (3.42) or eqn (3.43). Alternatively, the elements of the loaded elastic stiffness tensor can be determined directly through fluctuation formulae similar to those presented in Section 3.4.2 but including a correction term, and by setting the reference cell matrix necessary to define the strain in eqn (3.4) equal to the average cell matrix at the applied stress and temperature, $\mathbf{h}_0 = \langle \mathbf{h} \rangle$, as derived in ref. 249 and 250.

3.4.4.1 Determining Elastic Stability through the Born Stability Criteria

Intuitively, a MOF structure is said to be elastically stable at a given temperature T if any arbitrary infinitesimally small strain $\boldsymbol{\varepsilon}$ increases its free energy F.[251] For such small strains, the harmonic approximation of eqn (3.33) is valid

¶¶As mentioned before, the different definitions of the elastic stiffness tensor (based on the stress–strain, stress–energy density, and elastic wave propagation) no longer coincide when the material is subjected to an external load. Herein, we will apply the definition necessary to check the Born stability criteria (based on strain–energy density) and refer the interested reader to further discussions on this topic.[245,248,310,311]

and the aforementioned statement requires **ε**:**C**:**ε** to be positive for all small deformations **ε**, the so-called Born stability criterion. As a result, a necessary and sufficient condition for a given MOF structure to be elastically stable at a given temperature T is that its elastic stiffness tensor **C** is *positive definite* or, in other words, that the eigenvalues of **C** are all positive or that all its leading principal minors are positive (Sylvester's criterion).[251,252] Using the terminology introduced in Section 3.4, this implies that energy needs to be supplied to deform the system, even along the softest or most compliant deformation mode, which is the eigenmode corresponding to the lowest eigenvalue of **C**. From the point of view of the fluctuation formula of eqn (3.40), Parrinello and Rahman noted that elastic instability of a crystal would lead to a divergence in some of the correlations $\langle \varepsilon_{\alpha\beta}\varepsilon_{\mu\nu}\rangle - \langle \varepsilon_{\alpha\beta}\rangle\langle \varepsilon_{\mu\nu}\rangle$.[229]

For a cubic crystal, calculating the eigenvalues of the elastic stiffness tensor and requiring them to be positive leads to the well-known elastic stability criteria[251]

$$C_{11} + 2C_{12} > 0,\ C_{11}{-}C_{12} > 0,\ C_{44} > 0. \tag{3.44}$$

In turn, these inequalities can be interpreted as requiring the material to be stable against a volumetric compression or expansion, against orthorhombic deformation, and against monoclinic shear.[253] Important, however, is to realise that eqn (3.44) is a specific form of the Born stability criteria valid *only when a cubic crystal system* is considered. For other crystal systems, with other nonzero elastic constants, the requirement that the elastic stiffness tensor is positive definite leads to different Born stability criteria, as summarised by Mouhat and Coudert.[252] The lower the symmetry of the system, the more elastic constants appear in the stiffness tensor and the more intricate these expressions become.[252]

For materials subjected to an external stress **σ**, the Born stability criteria should be expressed in terms of the loaded elastic stiffness tensor **B** (see eqn (3.42)) or its symmetric variant $2\mathbf{A} = \mathbf{B} + \mathbf{B}^T$: a given material at a certain temperature and under a certain external stress is stable with respect to small elastic deformations if, and only if, **B** or **A** is positive definite.[253–255] As an example, for a cubic system under a hydrostatic pressure P (which retains the cubic symmetry), the elastic stability criteria of eqn (3.44) transform to

$$C_{11} + 2C_{12} + P > 0,\ C_{11} - C_{12} - 2P > 0,\ C_{44} - P > 0. \tag{3.45}$$

One has to take care, however, that a general stress may lower the symmetry of the crystal. The requirement that the loaded elastic stiffness tensor is positive definite, may hence involve a more cumbersome expression of its elastic constants than requiring the unloaded elastic stiffness tensor to be positive definite.

Using these definitions, the elastic stability region of a MOF can be defined as that region in parameter space (including, *e.g.*, temperature, stress, and gas loading) for which the Born stability criteria are satisfied. A first study

exploring this stability region for a MOF was performed in 2012, by calculating the Born stability criteria for the cubic ZIF-8 material as a function of the pressure for different temperatures and methane loadings.[235] As shown in Figure 3.16, which illustrates the two smallest out of the three Born stability criteria for this cubic material, $C_{44} - P > 0$ is the first criterion to be violated for ZIF-8, irrespective of the methane loading or temperature.[235] As could be predicted qualitatively by the extremely low 0 K shear modulus of ZIF-8 discussed in Section 3.4.1, the material first becomes mechanically unstable under shear deformation.[235] However, while the 0 K shear constant C_{44} of ZIF-8 amounts to about 1 GPa, the guest-free material becomes unstable already at a lower pressure of ~0.4 GPa,[235] a result which was later also verified *via* DFT calculations.[112] This illustrates the importance of determining the elastic constants and verifying the positive definiteness of **B** at or close to the thermodynamic conditions of interest, at finite temperatures and pressures (using the technique in Section 3.4.2), rather than obtaining the elastic constants from simulations without external stress (using the technique in Section 3.4.1) and applying eqn (3.44) or its analogues to determine the stability region.[245] While Figure 3.16 demonstrates that the pressure at which this instability occurs is rather insensitive to temperature, the inclusion of methane in this material does expand its region of stability appreciably.[235]

A similar shear-induced elastic instability was also observed for ZIF-4,[235] several ZIF-8 analogues,[236] and the denser $Zn(CN)_2$ materials,[240] whereas

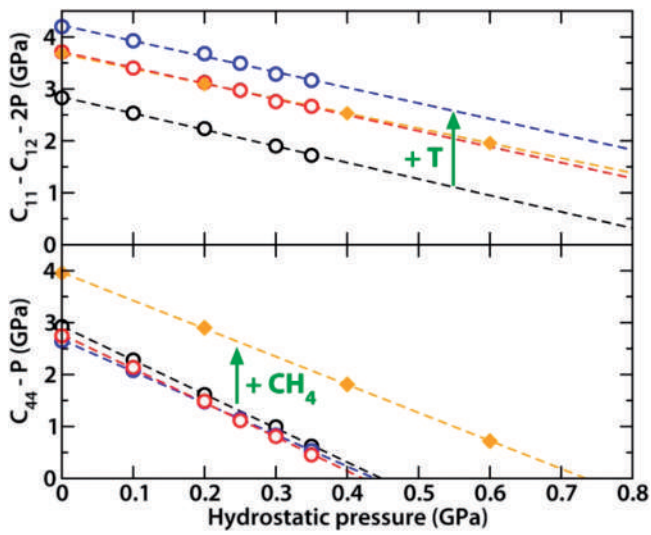

Figure 3.16 Evolution of the Born stability criteria for compression (upper panel) and shear (lower panel) of ZIF-8 as a function of hydrostatic pressure. Black: empty ZIF-8 at 77 K; red: empty ZIF-8 at 300 K; blue: empty ZIF-8 at 500 K; orange: ZIF-8 with 18 methane molecules per unit cell at 300 K. Reproduced from ref. 235 with permission from American Chemical Society, Copyright 2013.

the softest deformation mode for the defect-free cubic UiO-66 MOF was observed to be an axial deformation, which violates the Born stability conditions starting from a pressure of ~1.85 GPa onwards.[49] In contrast, in the UiO-66 analogue obtained by replacing the phenyl ring in the BDC ligand by a C≡C moiety, the first Born stability criterion to be violated is the isotropic compression mode.[141] This difference with respect to UiO-66 was attributed to the weaker steric hindrance when compressing the MOF containing this aliphatic linker compared to the aromatic linker in UiO-66.[141] A similar variation in the weakest deformation mode leading to mechanical instability was observed in DUT-49 and reticular analogues, although the underlying mechanism remains uncertain at this point.[237]

In 2018, this procedure to determine the mechanical stability of MOFs was contrasted with the anisotropy signature described in Section 3.4.3 and the construction of pressure-*versus*-volume equations of state, which will be discussed in more depth in Sections 3.5 and 3.6. To this end, next to the cubic and rigid UiO-66 and MOF-5 materials, MIL-47 and MIL-53 were also considered, for which the lp phases belong to the orthorhombic crystal system.[136] For MOF-5, this analysis showed that the first Born stability criterion to be violated is not due to shear deformation, as one may expect based on the low C_{44} value and based on predictions within the QHA framework,[157] but is rather induced by isotropic compression, given that Figure 3.17 reveals that the associated Born stability criterion shows a

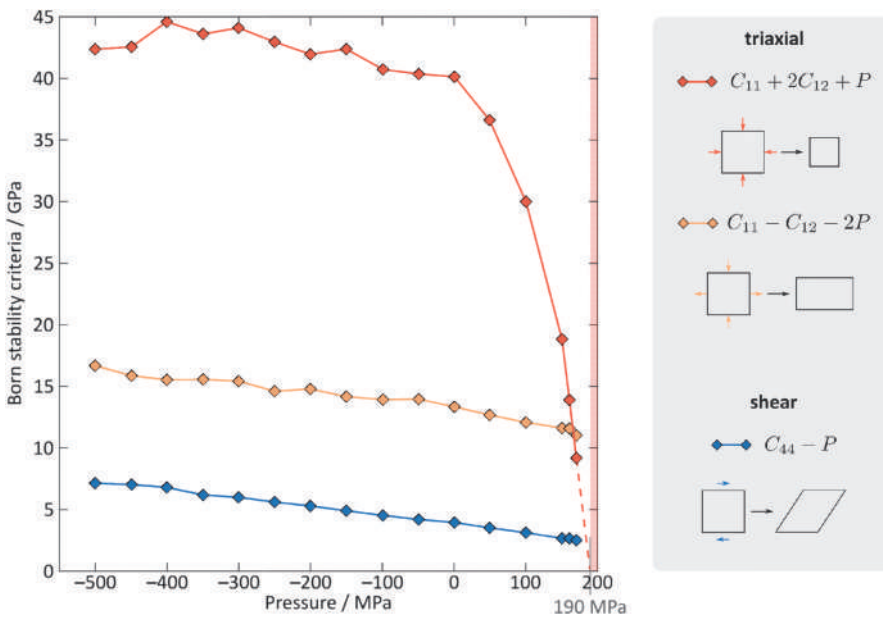

Figure 3.17 Born stability criteria for MOF-5 as a function of the hydrostatic pressure, at 300 K. Adapted from ref. 136 with permission from American Chemical Society, Copyright 2018.

substantial pressure-induced softening.[136] Despite the similarities between the lp phases of MIL-47(V) and MIL-53(Al), their mechanical instability was observed to be induced by two different deformation modes: a triaxial deformation mode for MIL-47 and a shear deformation mode for MIL-53, presumably due to the weaker inorganic chain present in the latter material.[136] In contrast to the cubic UiO-66 and MOF-5 materials, however, the weakest axial deformation mode in MIL-47 is not easily interpretable, due to the lower symmetry of this orthorhombic structure.[136] This was further exemplified by the even less-symmetric monoclinic cp phase of MIL-53(Al). In this case, the Born stability criteria need to be evaluated by calculating the eigenvalues of the stiffness tensor and requiring them to be positive, giving only limited and less-interpretable information about the deformation mode leading to mechanical instability compared to more symmetric phases.[136]

3.4.4.2 Determining Dynamic Stability through the Vibrational Spectrum

While the elastic stability criteria in Section 3.4.4.1 give insight into the macroscopic deformation mode of the crystal that first induces mechanical instability, complementary microscopic insight can in principle be obtained through the vibrational spectrum. The Hessian matrix, introduced in eqn (3.38), describes the energy associated with small displacements of the different nuclei from their equilibrium structure, in the harmonic approximation. The Hessian matrix therefore takes a very similar role to that of the stiffness tensor: while the elastic stiffness tensor should be positive definite to ensure elastic stability, the Hessian matrix should be positive definite to ensure dynamic stability. If the Hessian matrix contains negative eigenvalues, corresponding to imaginary vibrational frequencies, displacing the nuclei along the associated vibrational modes would lower the energy of the system, indicating its mechanical instability. However, theoretically obtaining these low-frequency or terahertz vibrations is highly challenging, as is their interpretation, given that these collective vibrational modes contain contributions from many atoms in the unit cell.[188,256]

As an instructive example, Ryder *et al.* investigated the terahertz vibrations in ZIF-4, ZIF-7, and ZIF-8,[256] as well as in HKUST-1,[188] which were discussed earlier in Section 3.4.1.5. For ZIF-4, two soft phonon modes were identified: one associated with a distortion of the 4MR aperture, discussed earlier in Section 3.4.1.3, and one associated with a gate-opening phenomenon.[256] For ZIF-7 and ZIF-8, several soft modes were found that could be associated with gate-opening and breathing mechanisms, as well as a soft mode that could explain the experimentally observed phase transition in these materials.[256–258] Also the phase transition in the related $Zn(CN)_2$ material could be associated with the instability of several low-frequency vibrational modes.[259] While promising, extending this approach to finite temperatures is not

straightforward due to the difficulties in accurately assigning vibrational modes in those cases. Recently, Maul *et al.* presented such an approach that combines this vibrational analysis with the Born stability criteria to obtain both macroscopic insight into the weakest deformation mode and atomic insight into which nuclei play a major role in determining mechanical instability.[112] The Born stability criteria revealed that the shear deformation, defined by C_{44}, is the weakest deformation mode in ZIF-8.[112] Subsequently, they determined through the relaxation term in eqn (3.37) that the antisymmetric breathing of the 4MR aperture and the antisymmetric gate opening contribute most to the relaxation term associated with the C_{44} elastic constant and hence to instability.[112]

3.5 The Response of Flexible MOFs to Large Pressures: the Inelastic Regime

Thanks to their porous structure, many MOFs undergo large-amplitude structural phase transitions under external stimuli.[3] Studying the mechanical response of these flexible MOFs or SPCs beyond the equilibrium regime requires dedicated techniques differing from those outlined in Section 3.4. While the approaches discussed in Sections 3.4.3 and 3.4.4 give insight into whether a MOF is flexible or not and, in the case of the Born stability criteria, at which pressure it may undergo a phase transition, they do not model the phase transition explicitly. As a result, none of these aforementioned techniques provide information about the structure of the MOF during and after the phase transition or the energy needed to induce these transitions.

In this section, three general techniques will be discussed to access that information. The most straightforward technique, outlined in Section 3.5.1, consists in probing the response of the MOF structure during an MD simulation in the $(N,P,\boldsymbol{\sigma}_a,T)$ ensemble at various pressures and following the phase transition that is observed once the external pressure P is sufficiently high. Due to the inability of this technique to determine the energy required to induce the phase transition or the difference in energy between the initial and final phases, as well as due to inaccuracies in predicting the transition pressure, two other approaches will be outlined in Sections 3.5.2 and 3.5.3. In Section 3.5.2, the energy-*versus*-volume equation of state, introduced in Section 3.4.1 to extract the equilibrium bulk modulus, will be extended so to cover the different phases the material can attain. In Section 3.5.3, a technique will be outlined that generalises this approach to finite temperatures, giving rise to pressure and free energy equations of state that govern the dynamics of MOFs under experimental conditions. While flexibility in MOFs can be induced by many stimuli, we will focus on mechanical stress and pressure as stimuli herein to keep the discussion succinct and refer the reader interested in a broader range of stimuli-induced transitions to ref. 3 and 260.

3.5.1 Directly Modelling Phase Transformations in Flexible MOFs and Its Limitations

Initial force field studies on MOFs focussed on their exceptional adsorption properties, which were described by keeping the atomic structure of the MOF rigid and only accounted for noncovalent interactions between the MOF and the adsorbed gases. Given that these so-called 'rigid' force fields are unable to describe phase transitions, and given that *ab initio* MD simulations lasting several picoseconds – necessary to observe a phase transition – were computationally too costly in the early years of MOF research, the first direct (N,P,$\boldsymbol{\sigma}_a$,T) simulations that demonstrate pressure-induced phase transitions in MOFs were only reported in the early 2010s. For MIL-47(V), Yot *et al.* combined high-pressure mercury intrusion experiments with direct force field simulations to discover that this material, which was known to remain rigid under gas adsorption, can undergo phase transitions under high mechanical pressures.[191] The simulated lp-to-cp transition pressure of 137 MPa and the simulated cp-to-lp transition pressure of 66 MPa were both in good agreement with the experimental range of pressures, amounting to 85–125 MPa and 55–75 MPa, respectively, and are rather high compared to other flexible MOFs.[191] For isostructural MIL-53(Cr), lower transition pressures were observed, amounting to 53.5 MPa and 2.4 MPa for the lp-to-cp and cp-to-lp transitions, respectively, which decrease further when low amounts of guest molecules are present inside the pores.[202,261,262] This latter observation is in line with the equivalence between internal adsorption stress and external mechanical stress postulated earlier.[263] These computational studies also identified the rotation of the phenyl ring with respect to the carboxylate group in the BDC ligand as one of the main rearrangements during breathing in MIL-47(V) and MIL-53(Cr),[191,202,261] next to the experimentally observed 'knee cap' motion in which the carboxylate O–O axis acts as a hinge.[264] For MIL-53(Al), an even lower lp-to-cp transition pressure of 19 MPa was obtained.[265]

In addition to the aforementioned force field studies, also several *ab initio* MD simulations have been performed to study pressure-induced phase transformations in MOFs. In cases where the studied phase transformation is reconstructive in nature rather than displacive, such an *ab initio* approach is vital to describe the bond rearrangement. However, as with force fields, extreme care needs to be exerted regarding technical details, given that the occurrence of a phase transformation may depend on, among other things, the basis set size, the size of the unit cell, and the functional and dispersion scheme used, and this to an even larger extent than for the static simulations described in Section 3.4.1.[266] Using the B3LYP functional,[166] Ortiz *et al.* followed this approach to predict the flexibility of NOTT-300 and CAU-13.[224] For NOTT-300, an lp-to-cp transformation was observed from pressures of 700 MPa onwards.[224] Although the authors noted that large volume fluctuations were already visible starting from 500 MPa, no transformation was observed in the 6 ps simulation time at this pressure, an important point discussed later in this section.[224] Also CAU-13 was predicted to be flexible, although

the transformation to its lp phase was observed for *negative* mechanical pressures.[224] However, as mentioned before, such negative pressures can be achieved by means of adsorption stress, when a low amount of suitable guest molecules adsorb in the MOF.[263]

Similarly, ZAG-4 and ZAG-6 were predicted to undergo proton transfer at high pressures (3.7 GPa and 3.0 GPa, respectively), which in the case of ZAG-6 is accompanied by a coiling of the linker.[216] While these results were obtained through minimisation of the enthalpy rather than through a direct $(N,P,\boldsymbol{\sigma}_a,T)$ simulation, it is important to mention that the proton transfer describing the phase transformation cannot be modelled *via* force-field techniques due to the bond rearrangement, necessitating the more costly *ab initio* technique used in this study.[216] A similar minimisation procedure was employed to theoretically predict a displacive phase transition in ZIF-8 at around 3.8 GPa, under the condition that the well-known reconstructive phase transition at lower pressures is suppressed, for instance by theoretically constraining the symmetry of the material.[169] For CoBDP, an lp-to-cp phase transition was predicted at an extremely low pressure of 0.5 MPa.[217]

While these direct simulation approaches are attractive to gain insight into the possible occurrence of phase transitions in a material, there are a few pitfalls associated with them. Direct simulations explore only one possible trajectory through phase space at the given temperature and pressure, while discarding all other potential trajectories. This also implies that repeating the same simulation with slightly different initial conditions – atomic positions, velocities, or slight changes in the initial cell matrix – may fundamentally alter the simulation results, making interpretations based on a single simulation speculative. Instead, a proper analysis of phase transitions requires taking an ensemble average over all possible trajectories, weighted with their proper statistical importance. This is key in the approaches outlined in Sections 3.5.2 and 3.5.3.

However, even when repeating the direct $(N,P,\boldsymbol{\sigma}_a,T)$ simulations of this section several times with slightly different initial conditions to stimulate ergodicity, taking a statistical average may still underestimate the transition pressure. To understand this, Figure 3.18 shows the simulation time needed to observe an lp-to-cp transition in a $1 \times 2 \times 1$ unit cell of MIL-53(Al), containing 152 atoms, at 300 K and at various pressures between 0.1 MPa and 1000 MPa.[83] For each pressure, 100 independent simulations were performed starting in the lp phase.[83] In addition, each simulation was conducted for two different barostat implementations, the MTK barostat and the Langevin barostat,[96,97] and three different barostat relaxation times of 1 ps, 5 ps, and 10 ps.[83] For simulations performed at pressures higher than the experimental lp-to-cp transition pressure, an lp-to-cp transition was observed in all simulations, as expected.[83] Moreover, these transitions occurred on a subpicosecond timescale, as shown in Figure 3.18(b), which are also accessible in AIMD simulations.[83] However, an lp-to-cp transition was also unexpectedly observed for all simulations at pressures *below* the experimental transition pressure and *below* the transition pressure extracted *via* the thermodynamic

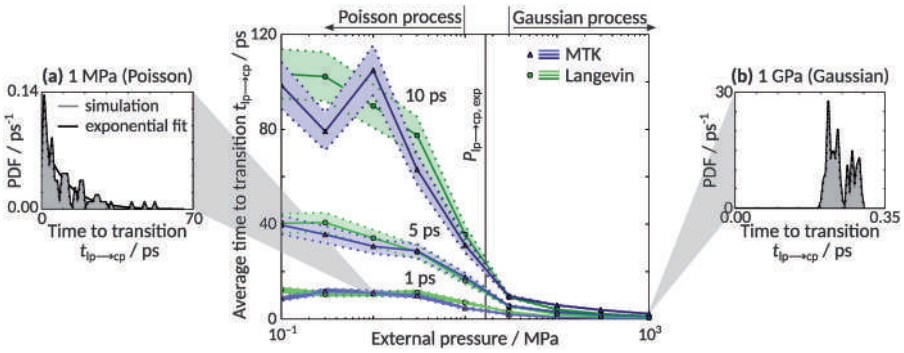

Figure 3.18 Average simulation time needed to observe the MIL-53(Al) lp-to-cp transition in a $(N,P,\boldsymbol{\sigma}_a = 0,T)$ ensemble at 300 K as a function of the applied pressure and carried out for different barostats and barostat relaxation times of 1, 5, and 10 ps. The shaded regions indicate the 1σ confidence interval for this average simulation time. The vertical line indicates the experimental transition pressure. The side panes (a) and (b) display the probability density function (PDF) of the time to transition for two selected pressures, each constructed based on 100 independent simulations carried out with the MTK barostat and a relaxation time of 1 ps. Adapted from ref. 83 with permission from American Chemical Society, Copyright 2015.

approach outlined in Section 3.5.3.[83] Compared to transitions at higher pressures, the simulation time needed to induce transitions at these lower pressures is substantially higher – up to several tens of picoseconds, which are not reached in the aforementioned AIMD simulations – and also more strongly impacted by the barostat relaxation time.[83] Furthermore, as shown in Figure 3.18(a), the time to observe the transition at a certain pressure below the experimental transition pressure was found to be exponentially distributed, indicating that the mechanism inducing this transition is stochastic in nature.[83]

These premature phase transformations were found to be induced by fluctuations in the internal pressure of the material.[83] Even though the average internal pressure converges to the value supplied to the barostat scheme, simulations with pressure control show substantial relative fluctuations in the instantaneous pressure, as demonstrated in Figure 3.6(a). These fluctuations, which scale inversely with the square root of the number of atoms, are necessary to properly sample the isobaric ensemble; a similar effect is also present in temperature control.[267] In the case of the 152-atom unit cell of MIL-53(Al), these pressure fluctuations were found to amount to several gigapascals, thereby exceeding the experimental lp-to-cp transition pressure by several orders of magnitude.[83] When a sufficiently large sequence of positive pressure fluctuations are observed during a simulation, they may hence trigger a premature phase transition.[83] A similar underestimation of the transition pressure *via* direct $(N,P,\boldsymbol{\sigma}_a,T)$ simulations was also observed for a series of IRMOFs by Ying *et al.*[237] They also noted that this effect was

much less pronounced in DUT-49-like materials, most likely because of their larger conventional unit cells, as the conventional DUT-49 unit cell contains 1728 atoms.[237] Besides providing an underestimation of the transition pressure, these premature phase transitions also limit how close to mechanical instability one can simulate the vibrational spectra or Born stability criteria of Section 3.4.4. As a result, to use these techniques, one needs to rely on extrapolations to obtain the Born stability criteria or vibrational modes at the point of instability.[136]

3.5.2 Modelling Flexible MOFs at 0 K: Energy Equations of State

A first approach to overcome the limitations of direct (N,P,$\boldsymbol{\sigma}_a$,T) simulations outlined in Section 3.5.1 – as well as the Pulay stress for plane–wave codes mentioned earlier in Section 3.4.1 – is to model the energy-*versus*-volume equation of state of the material that connects the different (meta)stable states. Such an energy equation of state can be obtained by optimising the cell shape and nuclear coordinates of the MOF while keeping its volume fixed for different structures dispersed along a volume grid, and collecting the internal energy as a function of the volume. This gives access both to the energy difference between the different phases and to the transition pressure necessary to induce transformations between them, given that the 0 K pressure equation of state can be obtained as the negative of the first derivative of the $E(V)$ profile with respect to the volume. The approach outlined here assumes that the different phases can be distinguished based on the volume and is in its basic form limited to 0 K results. Although extensions to both limitations will be discussed in Section 3.5.3, these 0 K profiles are computationally less expensive than those discussed in Section 3.5.3 because they only require optimisations. As a result, they are more easily accessible through *ab initio* techniques, thereby providing a first set of guidelines on how to model the flexibility of MOFs at 0 K, which are directly transferable to finite temperatures.

Although Vanpoucke *et al.* only reported partial energy equations of state for the cp and lp phases of MIL-47, they extracted an *ab initio* lp-to-cp transition pressure between 82 and 125 MPa, depending on the magnetic ordering of the inorganic chains, and an lp phase that is around 1.3 kJ mol^{-1} more stable than the cp phase.[109,205,‖‖] Through the harmonic approximation, they predicted that entropic factors would increase the relative stability of the lp phase to around 13.7 kJ mol^{-1} at 300 K.[109] These small energy differences emphasise the need to use very accurate models to estimate the energy, given that changes in the choice of functional or dispersion scheme can give rise to errors that are substantially larger than these energy differences.[55,268,269] This can be exemplified by MIL-53(Cr), shown in Figure 3.19, where both the

‖‖Energy differences are defined per unit cell of the material, which contain four metal atoms for MIL-47 and MIL-53.

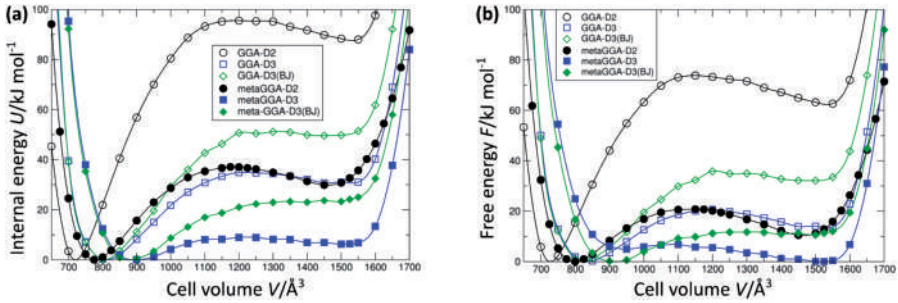

Figure 3.19 Equation of state of (a) the internal energy, neglecting zero-point motion, and (b) the Helmholtz free energy at 293 K for MIL-53(Cr) as a function of the volume, for different density functionals. Each curve is scaled so that its minimum is zero. Adapted from ref. 268 with permission from American Chemical Society, Copyright 2017.

internal energy and the Helmholtz free energy at 293 K obtained through QHA strongly depend on the functional and dispersion scheme, which also affect the prediction of the most stable phase in this temperature range.[268]

The aforementioned observations were the motivation behind a more extensive study by Wieme *et al.*, in which the random phase approximation (RPA) to the correlation energy, including single-excitation (SE) effects, was adopted to model the 0 K energy equation of state for MIL-53(Al).[269] The RPA + SE equation of state showed that the MIL-53(Al) cp phase was only around 7.4 kJ mol^{-1} more stable than the lp phase, separated by an lp-to-cp barrier amounting to around 8 kJ mol^{-1}.[269] This bistability was found to occur because of an interplay between entropic effects (favouring the lp phase) and dispersion interactions (favouring the cp phase).[269] They used this knowledge to show that lowering the extent of dispersion interactions, such as by replacing the BDC ligand in MIL-53(Al) with a fumarate ligand, gives rise to an energy equation of state with only an lp minimum, while replacing the ligand with either BPDC or NDC ligands, with larger aromaticity and hence higher dispersion interactions, leads to energy profiles with only a cp minimum.[269] In contrast, altering the metal atom only has a minor effect on the energy profile, with MIL-53(Ga) showing the same bistability as MIL-53(Al).[269] The absence of a 0 K cp minimum in the fumarate-based MIL-53(Al) material as well as the bistability of MIL-53(Al) were also reproduced using a QuickFF force field,[265,270] although the stability of the cp phase in MIL-53(Al) was overestimated at both 0 K and 300 K.[265]

A similar MIL-53(Al) cp overstabilisation was also observed when applying the quasi-harmonic approximation[206] or through umbrella sampling simulations.[271] For the fumarate-based MIL-53, it was found that the gallium analogue stabilises the cp phase compared to the aluminium analogue, forming a metastable phase at 0 K.[199] A similar relative stabilisation was also observed by replacing the copper cation in DMOF-1(Cu) with zinc, although the lp phase remained the most stable phase at 0 K.[215]

These observations led to the theoretical prediction that the cp phase in DMOF-1 could be accessed by applying appropriate mechanical pressure, which was subsequently confirmed experimentally.[215] Finally, for a different wine-rack type material, CUK-1(Mg), the slope of the 0 K energy equation of state as a function of the volume is almost constant between the cp and lp phase.[272] This indicates that the cp-to-lp and lp-to-cp transition pressures coincide for CUK-1(Mg), hence forming the first pressure-driven molecular MOF spring.[272]

3.5.3 Modelling Flexible MOFs at Finite Temperature: Free Energy Equations of State

3.5.3.1 General Methodology

To incorporate the full impact of temperature on the mechanical properties of a MOF, the energy-*versus*-volume equation of state in Section 3.5.2 should be replaced by a Helmholtz free energy equation of state as a function of the volume.[273,274] Free energy profiles are ubiquitously adopted to describe transformations in biomolecular complexes, using a variety of so-called enhanced sampling techniques such as metadynamics,[275,276] umbrella sampling,[277] multistate Bennett acceptance ratio estimation,[278] thermodynamic integration,[279] and free energy perturbation.[280] When the free energy profile is obtained as a function of the volume, the pressure profile can be retrieved as the negative of its first derivative:

$$P(N,T;V) = -\frac{\partial F(N,T;V)}{\partial V}. \tag{3.46}$$

This pressure profile directly reveals the mechanical response of the material upon pressure.

An alternative way that circumvents taking this derivative – and hence avoids the numerical noise that may be introduced when predicting transition pressures this way – is to directly simulate the pressure-*versus*-volume or $P(V)$ equation of state, as first derived in ref. 83. In Section 3.5.2, the 0 K pressure profile was obtained by optimising the cell shape and nuclear coordinates at fixed volume for a variety of structures along a predefined volume grid. Analogously, the pressure profile at finite temperatures can be obtained by determining the ensemble-averaged instantaneous pressure of a material at a range of fixed volumes, while simultaneously allowing the nuclear positions and cell shape to dynamically fluctuate in line with the applied temperature and so that the average deviatoric stress is zero (only yielding a hydrostatic pressure).[83] Hence, the appropriate ensemble to directly simulate these $P_i(V)$ or $P(V)$ profiles at finite temperatures is the $(N,V,\boldsymbol{\sigma}_a = \mathbf{0},T)$ ensemble, in which the temperature T and the deviatoric stress $\boldsymbol{\sigma}_a$ are controlled and both the number of particles N and the cell volume V are kept fixed.[83] As was demonstrated in ref. 271, this thermodynamic integration procedure parallels the accuracy of alternative enhanced sampling methods, while

being, together with umbrella sampling, among the most efficient methods for this purpose.

As shown in Figure 3.20, any pressure equation of state can be divided into regions with a positive slope, which are mechanically unstable regions as they show a thermodynamically forbidden negative volume compressibility, that separate mechanically stable regions (with a negative slope), which can be stabilised under pressure. More specifically, the different (meta)stable states and transition states at any given pressure P_{ext} can be obtained by determining the intersections of the $P(V)$ profile with a horizontal line at $P = P_{ext}$ and classifying these intersections into mechanically (meta)stable states and mechanically unstable transition states. This is demonstrated in Figure 3.20, which shows three pressures that lead only to a stable cp state (at a pressure P_1), only to a stable lp state (at a pressure P_3), or to the presence of both a (meta)stable cp and lp state separated by a transition state (at a pressure P_2). Furthermore, the transition pressures between the different phases follow as the minima and maxima in the pressure profile (see Figure 3.20).

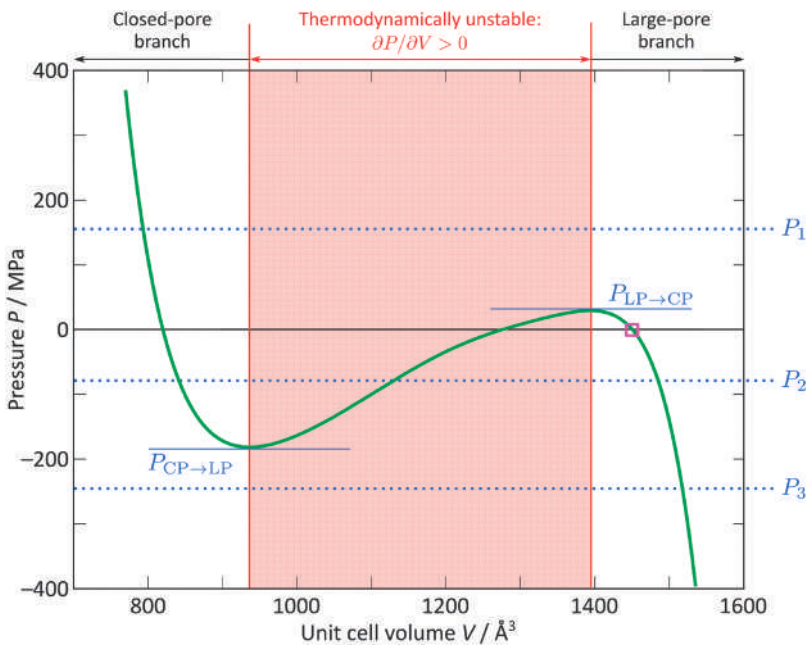

Figure 3.20 Generic pressure-*versus*-volume equation of state (green) for a bistable material, exhibiting a closed-pore (cp) and a large-pore (lp) phase, separated by a thermodynamically unstable region (red). The two transition pressures, lp-to-cp and cp-to-lp, are indicated by solid blue lines, whereas the magenta square indicates the (met)stable lp state at atmospheric pressures. The intersections between the equation of state and a blue dotted line indicate the different (meta)stable and, if present, transition state at that pressure. Adapted from ref. 136 with permission from American Chemical Society, Copyright 2018.

From the pressure profile, the free energy equation of state can be constructed *via* thermodynamic integration:[83]

$$F(N,T;V) - F(N,T;V_0) = -\int_{V_0}^{V} P(N,T;V')\mathrm{d}V' = -\int_{V_0}^{V} \langle P_i(N,T;V') \rangle \mathrm{d}V'. \quad (3.47)$$

Finally, from the above Helmholtz free energy, also the Gibbs free energy or free enthalpy profile at a pressure P can be determined as

$$G(N,P,T;V) = F(N,T;V) + PV \quad (3.48)$$

thereby revealing the relative stability of the different (meta)stable phases at any given pressure.[83] By repeating this procedure at different temperatures, also temperature-induced phase transitions can be predicted.[274] It is important to emphasise here that the cell shape $\mathbf{h}_0$ should be able to fluctuate when constructing $P(V)$ profiles.[281] If, instead of the appropriate $(N,V,\boldsymbol{\sigma}_a = 0,T)$ ensemble, the more popular but shape-restricted $(N,V,\mathbf{h}_0,T)$ ensemble is used, cell shape contributions to the free energy are neglected, which introduces a free energy error comparable to the free energy difference between the lp and cp phases in MIL-53(Al).[281] Finally, one should realise that the volume may not always be the most optimal parameter to describe pressure-induced phase transitions in MOFs.[282,283] In that case, one has to employ one of the other enhanced sampling techniques mentioned above to construct the free energy profile,[282,283] from which the pressure profile can then be obtained by taking its derivative with respect to the volume.

3.5.3.2 *Application to MOFs*

The general procedure described above was first adopted to determine the transition pressures for MIL-53(Al), revealing lp-to-cp and cp-to-lp transition pressures of *ca.* 30 MPa and −180 MPa, respectively, yielding much better agreement with the experimental transition pressures than those obtained through the direct method of Section 3.5.1.[83,136] For MIL-47, both transition pressures were found to be higher and the corresponding free energy equation of state only revealed a stable lp phase at atmospheric pressure and for temperatures between 100 K and 400 K.[136,204] Increasing the aromaticity of the ligand increases the relative stability of the cp phase, resulting in a bistable BPDC-containing COMOC-2 material, similar to MIL-53(Al), whereas the NDC-containing COMOC-3 material exhibits only a stable cp phase between 100 K and 400 K.[204] For CUK-1(Mg), a similar procedure demonstrated that it behaves as a spring-like material in which the lp-to-cp and cp-to-lp transition pressures coincide.[272] Similar to their 0 K behaviour discussed in Section 3.5.2, MIL-53(Ga) and the fumarate-based MIL-53(Al) show only a single stable phase at 300 K and atmospheric pressure.[274] For the MIL-53(Al) analogue in which the hydroxide anions in the inorganic chain are replaced by fluoride anions, a similar bistability as in MIL-53(Al) is found at room temperature, although only a stable lp phase remains at temperatures of around 450 K and higher.[274]

For the unfunctionalised DMOF-1(Zn), mercury intrusion experiments indicate an lp-to-cp transition at around 51 MPa without exhibiting a cp-to-lp transition upon lowering the pressure again, indicating that the material is bistable at 300 K in the absence of an external pressure.[215] Although this bistability was not retrieved using a QuickFF force field fitted to the *ab initio* Hessian matrix and geometry,[215] Keupp *et al.* did correctly obtain this bistability using a MOF-FF force field that was derived in a similar fashion,[18] demonstrating how small differences in the theoretical description of the interatomic interactions may greatly affect the predicted macroscopic behaviour. This is true to an even larger extent when considering fu-MOFs, which are obtained from DMOF-1 by the side chain functionalisation of its BDC linkers.[284] Keupp *et al.* noticed that the volume of the fu-MOF cp phase as well as its relative stability with respect to the lp phase strongly depend on the alkoxy group present on the BDC linker.[285] Even more importantly, for the longest functional groups considered in this study, the $P(V)$ profile depends on the conformation of the functionalised BDC linker, where some conformations exhibit a metastable cp phase, while others only retrieve a monostable lp material, which indicates that the volume alone may not be appropriate to describe the phase transition.[285] By combining experimental and computational tools, they further explored this observation for the copper-containing DMOF-1 and fu-DMOF-1 analogues.[286] This study revealed that the stability of the cp and lp phases of these materials, as probed through pressure equations of state, is governed both by the configurational entropy associated with the different conformations of the alkoxy groups as well as by the dispersion interactions acting between them.[286]

To explore the extreme volume contraction during the op-to-cp transition in DUT-49, Evans *et al.* highlighted the similarities between the elastic buckling of the ligand in this material and the (plastic) buckling of a column upon application of a critical load in macroscopic mechanics.[20] In addition, they constructed pressure-*versus*-volume equations of state at fixed guest loadings to understand the thermodynamics underpinning negative gas adsorption (NGA) in DUT-49.[20] Although these simulations were performed in the $(N,V,\mathbf{h}_0,T)$ ensemble instead of the $(N,V,\boldsymbol{\sigma}_a = \mathbf{0},T)$ ensemble and hence neglect cell shape sampling (*vide supra*), this has no substantial impact on the predicted free energy profiles given the large number of nuclear degrees of freedom in DUT-49.[281] These observations were later generalised to other members of the DUT family, revealing that the linker should both be stiff enough to stabilise the op phase of the structure under guest-free and overloaded conditions, while simultaneously being sufficiently soft to allow for the guest-induced op-to-cp transformation.[237,287,288]

Pressure equations of state have also been adopted to investigate the phase transition mechanism in flexible MOFs. In 2019, Rogge *et al.* investigated how increasing the simulation cell size affects the thermodynamics of MIL-53(Al), demonstrating that cp and lp phases may coexist as metastable configurations in between the pure-phase cp and lp phases, but only for crystals that are sufficiently large, as visualised in Figure 3.21.[19] For the studied MIL-53(Al)

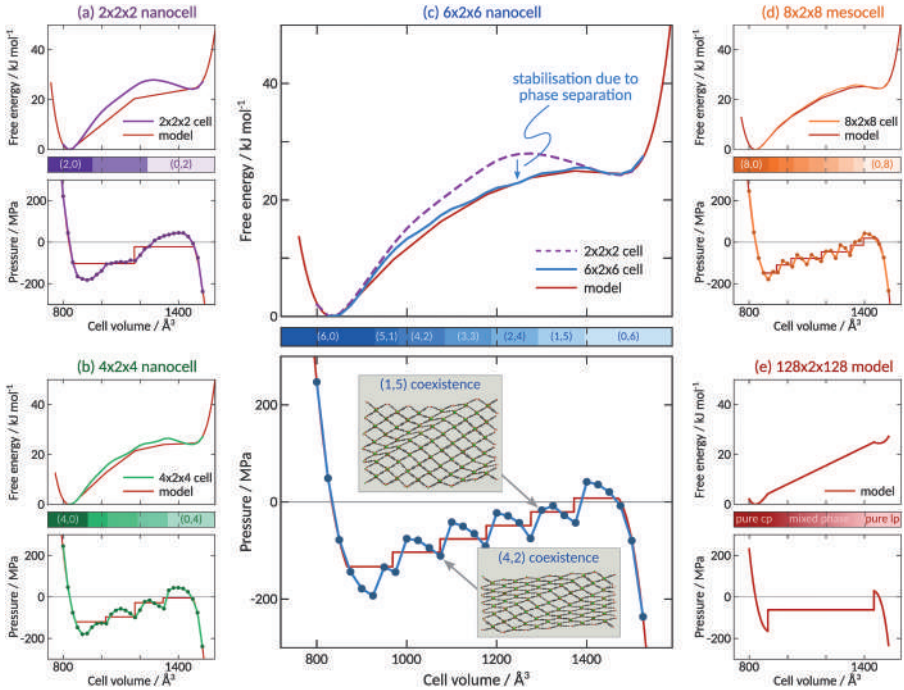

Figure 3.21 Stabilisation of the metastable cp/lp coexistence regions with increasing cell size. Pressure (bottom) and free energy (top) equations of state, with indication of the metastable (n_{cp},n_{lp}) phase coexistence regions, in which n_{cp} cp and n_{lp} lp layers coexist, as a function of the volume (middle) for four different cell sizes: (a) a 2 × 2 × 2 supercell, (b) a 4 × 2 × 4 supercell, (c) a 6 × 2 × 6 supercell, and (d) an 8 × 2 × 8 supercell, all at 300 K. The red lines indicate the fitted thermodynamic model, which is extrapolated in (e) for a 128 × 2 × 128 supercell (208.0 × 1.4 × 171.2 nm^3), similar in size to experimental MIL-53(Al)-NH_2 crystals. Reproduced from ref. 19, https://doi.org/10.1038/s41467-019-12754-w, under the terms of the CC BY 4.0 license https://creativecommons.org/licenses/by/4.0/.

mesocells, with a critical dimension larger than 10 nm, the possibility of phase coexistence also impacts the phase transition mechanism. While periodic boundary conditions on small unit cells imply a transition mechanism in which all unit cells transform collectively, phase coexistence in mesocells allow for a layer-by-layer transition mechanism[289] that is energetically more favourable than the concerted transition mechanism, as shown in Figure 3.21, and which becomes more likely the larger the crystal.[19] These phase coexistence regions, shown in the insets of Figure 3.21 for MIL-53(Al), can also be stabilised by dedicated temperature, pressure, or adsorption quenching experiments, as shown for DMOF-1(Zn), MIL-53(Al)-F, and CoBDP.[19] In a follow-up study on a one million atom simulation cell of MIL-53(Al), it was observed that the phase transition could also proceed *via* discrete nucleation

points instead of this layer-by-layer transition mechanism, but only for sufficiently high excess pressures.[24]

For DMOF-1(Zn), a similar layer-by-layer transition mechanism was also observed by Keupp *et al.* when discarding periodic boundary conditions altogether and modelling the free energy of various finite DMOF-1 crystallites with different sizes.[18] They found that this transition mechanism becomes more complex for fu-MOFs with larger alkoxy functionalised ligands.[285] However, by going beyond periodic boundary conditions, and hence also beyond the definition of a simulation cell, it also becomes less straightforward to define pressure in a finite crystallite simulation, in line with the discussion in Section 3.2.[18] To circumvent this problem, they calculated the free energy equations of state *via* umbrella sampling instead.[18] More recently, they proposed an alternative approach in which the pressure medium was modelled explicitly and distinguished between four different transition mechanisms in finite crystallites of DMOF-1, DUT-8, and DUT-128.[290]

While pressure equations of state derived in the $(N,V,\boldsymbol{\sigma}_a = \mathbf{0},T)$ ensemble can directly model pressure- and temperature-induced phase transitions, guest-induced transitions require a different approach. To model the appropriate thermodynamic potential in this case – the osmotic potential – the chemical potential μ of the guest molecules needs to be controlled next to the number of atoms of the host material N_{host}, giving rise to the osmotic ensemble.[291] However, directly simulating in this $(N_{host},\mu,P,\boldsymbol{\sigma}_a = \mathbf{0},T)$ ensemble may give rise both to unsurmountable free energy barriers between the different metastable states and to large volume fluctuations in the MOF unit cell, limiting the accuracy of this method similar to the earlier discussion in Section 3.5.1.[292] Therefore, Rogge *et al.* proposed in ref. 292 a hybrid MC/MD scheme in which MD simulations in the $(N_{host},N_{guest},V,\boldsymbol{\sigma}_a = \mathbf{0},T)$ ensemble are considered as an extra type of trial move during grand canonical Monte Carlo simulations in the $(N_{host},\mu,V,\mathbf{h}_0,T)$ ensemble. The flexible-host osmotic potential can then be directly calculated from the obtained flexible adsorption isotherms.[292] By comparing this method with three existing approaches, it was shown that it features a strongly improved accuracy thanks to isolating the volume – the coordinate along which the largest free energy barriers are typically encountered in flexible MOFs – from the other dynamic variables.[292] This approach was also successfully used to construct the osmotic potential in DUT-49 and explain how the occurrence of different (meta)stable states as a function of (gas) pressure and volume give rise to the attractive NGA phenomenon.[293]

3.6 The Response of 'Rigid' MOFs to Large Pressures: the Inelastic Regime

The distinction between rigid and flexible MOFs is not an absolute one (see Section 2.4 of Chapter 2) as many 'rigid' MOFs still contain some flexible modes, albeit not as extreme in amplitude as flexible MOFs. However, in

contrast to the flexible MOFs discussed in Section 3.5, the rigid MOFs discussed in this section all undergo a transition to a noncrystalline state when subjected to high pressures. Noncrystalline states, which are for instance encountered in amorphous MOFs, MOF liquids, or MOF glasses, show no long-range order.[26,37,294] This makes obtaining an accurate structural model of the material, as discussed in Section 3.3.1, substantially more difficult and limits the use of periodic boundary conditions, as they assume perfect translational order at a length scale corresponding to the simulation cell. Furthermore, classical force fields cannot describe these phase transformations if they are reconstructive in nature. As a result, many of the techniques mentioned in Section 3.5 can be adopted only to a limited extent for these noncrystalline states, and pressure-induced transitions of rigid MOFs are studied in a more *ad hoc* way compared to transitions in flexible MOFs. Herein, three important aspects will be covered: how plastic deformation nucleates and propagates through MOFs (Section 3.6.1, using MOF-5 as a case study), which deformation modes are responsible for MOF amorphisation and melting (Section 3.6.2, using ZIFs as a case study), and how different types of disorder and defects alter this plastic deformation behaviour (Section 3.6.3, using UiO-66 as a case study). Other important results concerning the inelastic behaviour of rigid MOFs will be discussed in Section 3.6.4.

3.6.1 Nucleation and Propagation of Mechanical Instability in the IRMOF Series

As the prototypical rigid MOF that undergoes amorphisation under relatively low pressures, different complementary approaches have been adopted to study amorphisation in MOF-5. In 2011, Graham *et al.* performed a series of *ab initio* optimisations under various external pressures, observing that mainly the zinc–oxygen bond lengths that connect the MOF-5 inorganic brick with the carboxylate moieties decrease upon increasing pressure.[155] In a classical force-field-based study in which the phase transition was modelled directly, Biswas *et al.* observed that MOF-5 undergoes a pressure-induced transition towards a ~60% denser structure at around 250 MPa,[128] which is below the amorphisation pressure determined experimentally.[36] This transition was found to be irreversible for the empty MOF-5, since releasing the pressure did not allow them to retrieve the original unstressed structure, although reversibility was obtained upon low hydrogen gas loadings.[36] In contrast to ref. 155, they did not find any substantial effect on the bond lengths under pressure, but rather attributed the observed phase transition to a cooperative rotation of the ligands and a hinge-like motion of the metal oxide clusters around the carboxylate joints.[36] A similar phase transition was also obtained by Rogge *et al.*, Ryder *et al.*, and Erkartal *et al.*,[136,157,295] although this latter study only observed amorphisation at pressures between 1 and 2 GPa.[295] Even though no bond reorganisation was observed, strong local distortions of the framework led to disorder within the unit cell, as evidenced from

radial distribution functions.[136,295] In all aforementioned studies, however, periodic boundary conditions were assumed and relatively small unit cells were used, thereby preventing the direct simulation of the loss of long-range order that accompanies amorphisation and limiting the range of transition mechanisms that could be observed, as discussed in Section 3.5.3.2.

To allow for disorder to take place on longer length scales, Banlusan *et al.* generated a 6 × 6 × 12 supercell of MOF-5, containing around 180 000 atoms.[296] They directly followed the structural transformation of the framework upon different uniaxial deformations *via* the ReaxFF force field,[296] which overcomes some of the limitations of classical force fields as it can be adopted to describe reactive events such as reconstructive phase transitions.[297] As an example, Figure 3.22 illustrates various snapshots of the plastic deformation in MOF-5 upon increasing compression along the [001] direction, using a colour bar to localise the positions in the material that show the largest volume compression and the largest plastic deformation.[296] For all deformation directions, Banlusan *et al.* observed that plastic deformation nucleates through local slip-collapse events, in which the ligand hinges with respect to the inorganic cluster resulting in a local slip of adjacent planes and an associated collapse of the unit cell,[296] while a later study showed that the exact deformation mechanism depends on the defects present in the material.[298] The propagation of local slip-collapse events releases

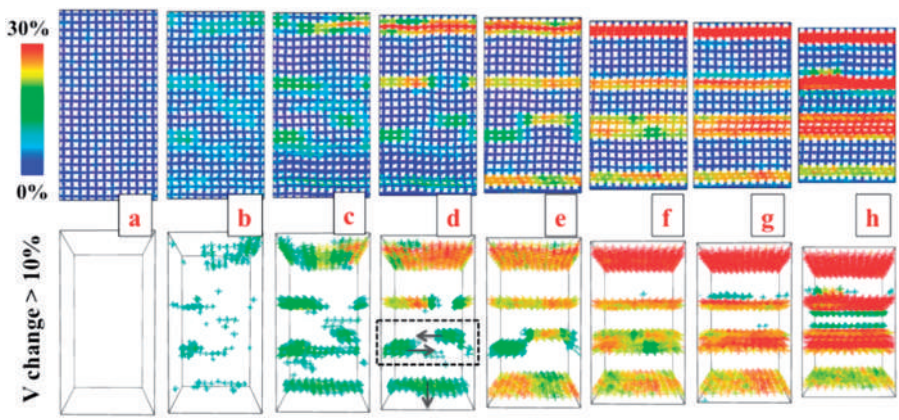

Figure 3.22 Atomistic snapshots showing plastic deformation of MOF-5 during the compression along the [001] direction at various strains, from 0% in panel a to 20% in panel h. Colours indicate the percentage of local volume decrease compared to the initial value in as-equilibrated systems. The bottom panels show only groups of atoms with a volume decrease of more than 10% to highlight the nucleation and propagation of plasticity. The arrows in the bottom panel (d) illustrate the propagation in ⟨100⟩ and ⟨010⟩ directions on the (001) plane of volume collapse. Reproduced from ref. 296 with permission from American Chemical Society, Copyright 2015.

the stress in neighbouring planes, which may even lead to the recovery from plastic deformation, as shown in Figure 3.22. Furthermore, while the initial nucleation of such slip-collapse events requires significant stress, additional slip-collapse events are facilitated by the heterogeneous nature of the now partially collapsed MOF-5, requiring lower stress.[296] Banlusan *et al.* also predicted that plastic deformation makes the material more compliant along certain directions.[296] Using a similar model, they later generalised these quasistatic loading conditions to simulate how a shock wave propagates through the MOF-5 framework.[299] Such a shock propagates through the material in two waves: a leading elastic wave followed by a pore-collapse wave that leads to plastic deformation and significant local heating of the material.[299] For sufficiently fast shocks, the pore-collapse wave also induced chemical decomposition of the material which partially dissipated the energy of the shockwave.[299]

Finally, Pallach *et al.* investigated how functionalising the MOF-5 ligand with different alkoxy sidechains affects its amorphisation behaviour using a variety of experimental and computational tools.[300] Besides calculating the pressure equation of state for these alkoxy-functionalised materials, they also performed pressure ramp force field simulations on much larger simulation cells to directly observe loss of spatial order upon increasing pressure, as evidenced by the simulated X-ray diffraction patterns and pair distribution functions.[300] These simulations confirmed the experimental observations that large volumetric contractions of these frameworks, induced by the alkoxy functionalisation, require random distortions of the framework which conflict with the rigidity of the material, leading to the concept of frustrated flexibility.[300]

3.6.2 Failure Modes in ZIFs and their Melting Behaviour

Given the variety of crystalline, and especially amorphous ZIF states, that can be obtained by controlling the temperature and pressure, these materials form a rich but largely untapped playground to computationally investigate how these different (dis)ordered states can be obtained. To study the mechanism behind the mechanical failure of ZIF-8, Hegde *et al.* investigated whether tensile or shear failure is most likely in this material.[301] Along the first mode, the material is cleaved upon failure, requiring twice the surface energy associated with the cleavage plane. Along the second mode, the material shears upon failure, forming stacking faults, and the free energy barrier to get from the material in equilibrium to the material with stacking faults needs to be overcome.[301] The authors determined computationally that the energy to form intrinsic stacking faults in ZIF-8 is rather low, comparable to that of metals like copper and gold. However, as the lowest-energy barrier to form these stacking faults from a fault-free material was found to require more energy than the energy needed to cleave the material, the authors concluded that ZIF-8 is nonetheless a brittle rather than a ductile material.

Furthermore, they suggested that ZIF-8 might energetically prefer to form a high-density amorphous state under shear stress rather than forming stacking faults.[301]

In 2014, Bouëssel du Bourg *et al.* directly modelled the mechanical stability of a set of ten ZIFs, each composed of zinc cations and unsubstituted imidazolate (Im) ligands but exhibiting a different topology using a force-field approach.[302] At room temperature, nine of these materials mechanically failed under compression at pressures of 0.4 GPa or lower, the sole exception being the material in the **coi** topology, confirming the weak mechanical stability of ZIFs also discussed in Section 3.4.4.1.[302] Despite the clear impact topology has on the mechanical stability of the material, no straightforward relation between the density and stability of the framework was observed.[302] For ZIF-4, one of the materials investigated in this study, Gaillac *et al.* later performed AIMD simulations of the crystalline unit cell at various high temperatures – up to 2250 K – to understand the mechanism behind its melting behaviour.[38] Radial distribution functions revealed that ZIF-4 glasses retain the chemical configuration, porosity, and short-range order of the crystalline parent material, while simultaneously being disordered on longer length scales (while still satisfying periodic boundary conditions).[38] A follow-up study revealed that this mechanism behind ZIF melting is largely unaffected by applying a pressure in the GPa regime during the heating process.[303] However, they did observe a decrease in energy to rupture a zinc–imidazolate bond at higher pressures due to the softening of the Im-Zn-Im angle upon pressurisation, leading to more frequent cleavage events.[303] As a result, AIMD simulations showed that increasing the pressure lowers the temperature necessary to melt ZIF-4; similar observations also hold for ZIF-62.[303]

3.6.3 The Impact of Defects on the Amorphisation of the UiO-66 Series

While localised defects and other types of spatial disorder are expected to profoundly impact the (mechanical) stability and amorphisation of all MOFs, this effect has until now only been extensively studied for MOF-5 (see Section 3.6.1) and the UiO-66 series of materials. In a force-field based study, the pressure-*versus*-volume equations of state of UiO-66, UiO-67, and UiO-68, as well as of a series of low-defective UiO-66 materials were investigated.[49] For the defect-free UiO-66, this equation of state reveals that mechanical instability is induced at 1.83 GPa.[49] In addition, although the force-field description precludes a direct simulation of the amorphisation process, the radial distribution functions and space group of the deformed materials show a distinct loss of crystalline order upon increasing the pressure above this instability, something that is not observed when applying this protocol to the flexible MOFs discussed in Section 3.5.3.[49] By extending the length of the ligand in UiO-66 to achieve the more porous UiO-67 and UiO-68 MOFs, a sharp decrease in loss-of-crystallinity pressure was observed, from 1.83 GPa

over 0.45 GPa to 0.2 GPa.[49] A similar observation holds when increasing the number of defects, although the pressure at which the material becomes unstable is not only determined by the concentration of defects, but also by their distribution throughout the framework (a similar conclusion was also drawn concerning the bulk modulus in Section 3.4.1.4).[49] Both for UiO-66 and UiO-67, the obtained results coincide well with those obtained through mercury intrusion experiments[50] and through computationally optimising the structure at increasing pressures and at 0 K.[178]

When accounting for node defects, the mechanical stability of UiO-66 is compromised even further, yielding a loss-of-crystallinity pressure of only 0.8 GPa for the **reo**-defective material, similar to the decrease in bulk modulus upon increasing defectivity.[182] However, incorporating cerium in the zirconium nodes of UiO-66 affects the loss-of-crystallinity pressure differently than it affects the bulk modulus: while it barely impacts the bulk modulus of the bimetallic UiO-66 materials, as discussed earlier in Figure 3.11, their loss-of-crystallinity pressure strongly decreases upon increasing cerium content, as shown in Figure 3.23.[182] In contrast, no substantial changes were

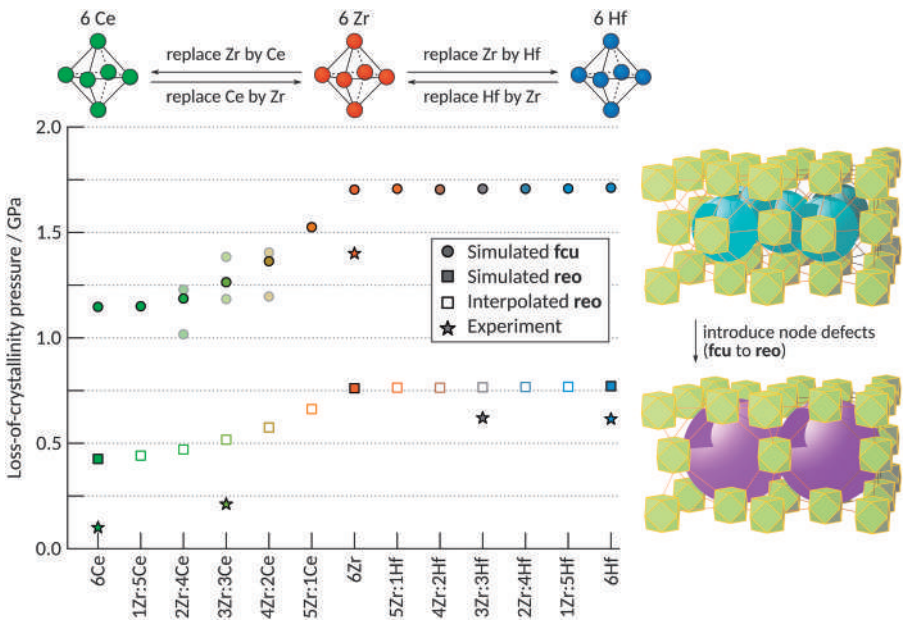

Figure 3.23 Loss-of-crystallinity pressures at 300 K for a series of bimetallic UiO-66 materials as determined from the pressure equations of state, both in the pristine **fcu** (circles) and node-defective **reo** (squares) topologies. For mixed-metal bricks for which two inequivalent bricks can be obtained, the weighted average is shown, whereas the two independent results are included as semi-transparent data points. Experimental results are indicated with stars. Reproduced from ref. 182 with permission from American Chemical Society, Copyright 2020.

observed upon hafnium incorporation instead, showing that the lower mechanical stability of UiO-66(Hf) that was observed experimentally in this study is solely a consequence of the higher defect concentration in this material and not an intrinsic materials property.[182] The observation that the mechanical properties in equilibrium, such as the bulk modulus, are not perfect predictors of the mechanical properties near instability was further underscored by the findings of Moghadam *et al.*[141] They noted that replacing the BDC ligand in UiO-66 with a shorter ligand leads to an increase in bulk modulus, as expected, but to a decrease in loss-of-crystallinity pressure, despite the lower porosity of the material.[141] This counterintuitive result was explained based on the two materials featuring different softest modes of deformation.[141]

3.6.4 Other Computational Studies on the Plastic Deformation of MOFs

In 2013, Fang *et al.* derived a force field for $Zn(CN)_2$ and adopted it to study the high-pressure behaviour of this NTE material that features the same tetrahedrally coordinated zinc cations as ZIFs, but with smaller ligands.[259] Direct $(N,P,\boldsymbol{\sigma}_a = \mathbf{0},T)$ simulations revealed that, at room temperature, $Zn(CN)_2$ undergoes a phase transition at pressures between 1.2 and 2.1 GPa, which could be explained by the substantially pressure-induced softening of several vibrational modes.[259] However, since increasing the temperature tends to stiffen these low-frequency modes, the phase transition could be postponed to higher pressures upon increasing the temperature, as confirmed by MD simulations.[259] This study was later extended by Trousselet *et al.*, considering ten additional topologies in which $Zn(CN)_2$ could potentially be synthesised. They clearly observed a correlation between porosity on the one hand, and the bulk modulus and the critical pressure needed to induce a structural transition on the other hand, with the densest topologies showing the highest mechanical stability, while the less dense topologies already failed in the sub-gigapascal regime.

As the absence of crystallinity in amorphous states pushes classical simulation methods to its limits, it forms an impetus to develop new approaches to model the plastic deformation in MOFs without resorting to the concept of periodic boundary conditions altogether. Two approaches can be distinguished at this point. First, similar to the finite DMOF-1 crystallites discussed earlier,[18] the Schmid group also cleaved a HKUST-1 surface to investigate how a tungsten tip penetrates into the material, mimicking nanoindentation experiments.[7] Although the classical force field description used in that work precludes modelling plastic deformation, their setup holds promise to model other surface-related mechanical properties. Second, FEM approaches have not only been used to model the elastic behaviour of mixed-matrix membranes,[61] but also to understand how stresses exerted on a macroscopic MOF crystal distribute within the particle, both in the

elastic and plastic regimes.[62] Although both approaches are still in their infancy at this point, the development of these and other methods that bridge the gap towards macroscopic MOF crystals is essential to fully comprehend how the intricate interplay of interactions at the atomic level gives rise to the attractive but complex mechanical behaviour of macroscopic MOF materials.

3.7 Conclusions and Outlook

Although MOFs exhibit a variety of attractive responses to mechanical stimuli, computational research on MOF mechanics remains largely in its infancy. The available literature is concentrated overwhelmingly on pressure-induced responses near equilibrium, such as the NLC and auxetic behaviour discussed in Section 3.4, with a strong focus on their 0 K behaviour. However, the inelastic responses of MOFs to large mechanical pressures, which give rise to flexibility and amorphisation as discussed in Sections 3.5 and 3.6, form an even more attractive field of computational research that remains largely untapped to date. In these concluding remarks, it is my intention to provide a personal reflection on the challenges that need to be overcome to mature computational research on MOF mechanics and the opportunities that the availability of such established and commonly available computational tools would engender.

A first challenge that was formulated throughout this chapter is how the occurrence of spatial disorder on various length scales can be designed to engineer MOF mechanics. While disorder and defects are often regarded as detrimental to the mechanical stability of a MOF, the large degree to which this disorder can be tuned as well as its strong effect on the macroscopic performance of MOFs open up enormous opportunities to design defect-engineered materials.[25] A first example of this was provided in Section 3.3.1, when discussing how the different orientation of low-symmetric ligands on the high-symmetric DUT-8(Ni) topology gives rise to distinct adsorption behaviour,[44] a functional property coined as ‘adaptive flexibility’ by Reynolds *et al.*[304] Two additional case studies, focusing on the inelastic response of MOFs, were presented in Sections 3.6.1 and 3.6.3, when discussing frustrated flexibility induced by the sidechain functionalisation of ligands in otherwise rigid MOFs and when discussing the impact of intrinsic defects in UiO-66 materials on their elastic and inelastic behaviour.[49,182,300] While forming an important guidance, these studies only form the tip of the iceberg, as (correlated) disorder is expected to be the norm rather than the exception in MOFs.[4] Seizing this opportunity requires an enormous effort from computational MOF researchers, as modelling such correlated phenomena requires both sufficiently large simulation cells and a proper inclusion of defects in these models. As with the discussion of phase coexistence in Section 3.5.3.2, where distinct phase transition mechanisms could be identified based on the size of the unit cell,[18,19,24,290] different realisations of correlated

disorder inside a material could in general amplify different sets of mechanical responses, from among a library of available responses.[304] This phenomenon, termed combinatorial mechanics,[304] emphasises the unparalleled design opportunities offered by MOFs; computational research will therefore be vital to isolate and identify the salient features that drive the macroscopic MOF response and to predict how these features interact with one another in macroscopic materials.

A second challenge that closely relates with this first one is how to realistically model disordered MOFs, from the atomic to the macroscopic level and from local defects over amorphous structures to beyond-particle disorder found in mixed-matrix membranes, MOF monoliths, and other shaped MOFs.[17,305] The wildly varying computational cost of different techniques such as DFT, atomistic force fields, CG force fields, and FEM approaches motivates the development of a hierarchical toolbox of computational techniques in order to cover MOF mechanics across these disparate length scales. Crucial in this regard is the proper theoretical foundation and validation of such a hierarchical bottom-up approach. This is determined by the information that is transferred between more accurate but also more expensive methods on the one hand and less accurate methods that can be adopted for larger systems on the other. Examples of such hierarchical approaches are dispersed throughout this chapter and include FEM techniques that take as input the elastic moduli calculated at the *ab initio* or force field level,[61,62,306] the CG force field of HKUST-1 that was fitted based on an atomistic force field,[7] the HKUST-1 atomistic force field derived based on the *ab initio* stiffness tensor,[78] and the micromechanical model, in which the force-field based elastic stiffness tensor is used as input to derive the mechanics of MOFs at much larger length scales.[60] As these examples show, mechanical properties such as strain fields and the elastic stiffness tensor play a central role in bridging these different length scales, evidencing the need for more in-depth and hierarchical computational studies on MOF mechanics.

A third challenge for computational MOF mechanics is to overcome the focus of current literature on the response of these materials to hydrostatic pressures and to account for their response to a more general stress state. Since stress is a tensorial quantity, compared to pressure as a scalar quantity, subjecting a MOF to a general stress state would most likely pave the way to discover an even larger versatility of attractive stress-induced MOF phenomena that are not expressed under pure hydrostatic pressure. However, general stress control in molecular simulations remains the exception today due to the confusion that arises from the different definitions of stress during a molecular simulation, as mentioned in Section 3.2.2, and the apparent lack of a proper definition of a Gibbs free energy under general stresses and for general deformations, as discussed in Section 3.3.3. As a result, current barostat coupling schemes have only been tested for hydrostatic pressures, save for some very limited non-MOF related examples

whose applicability to MOFs is uncertain, given the mechanical softness of these materials that may reveal inconsistencies in general stress coupling schemes that remain hidden for more rigid materials. Therefore, there is an urgent need to develop and validate more general stress coupling schemes, applicable to both periodic simulations and isolated MOF crystallites, both from a fundamental theoretical curiosity and in order to fully explore the entire library of structural responses MOFs can exhibit when subjected to such a general stress.

While this book focuses on MOF mechanics, the mechanical behaviour of MOFs cannot be fully decoupled from their adsorption or thermal behaviour. This is clear when considering for instance the coupling between NTE and purely mechanical phenomena such as NLC and auxetic behaviour, the temperature-induced melting of ZIFs which is affected by the pressure exerted on the material,[303] as discussed in Section 3.6.2, and the impact of temperature on the limit of mechanical instability, which was examined more closely in Sections 3.4.2 and 3.4.4. As a result, a fourth challenge arises to rationalise how different external stimuli – temperature, sorption, mechanical stress, among others – can amplify each other to access MOF phenomena inaccessible when applying only a single stimulus. This idea has been explored through the equivalency between mechanical stress and adsorption-induced stress[263,307] and through thermal stresses,[308] although these examples remain scarce at the moment.

A final challenge for the computational research on MOF mechanics is the general lack of high-throughput studies. Compared to, *e.g.*, adsorption phenomena, such high-throughput studies on the mechanical behaviour of MOFs are much scarcer and the library of MOF structures investigated in these studies is typically much smaller and less diverse. While this connects to the computational cost associated with accurately calculating finite-temperature mechanical properties in MOFs, which is higher than for purely structural properties, such high-throughput studies are vital to identify overarching trends that may be obscured when only focussing on specific MOFs. While the accuracy of these high-throughput projects is typically lower than for studies focussing on one material or one class of materials, the qualitative trends obtained in this way are pivotal to go beyond phenomenological observations of attractive mechanical behaviour in MOFs. In addition, this accuracy limitation may be partially overcome by adopting stepwise screening, as in ref. 141, in which less expensive levels of theory are used first to filter the most promising materials, which are subsequently considered at a higher level of theory.

While this chapter demonstrates that the challenges that need to be overcome to mature computational MOF mechanics to a fully developed field of research are numerous, so are the variety of new mechanical phenomena hiding in these materials. In this respect, our overarching aim should be to develop computational MOF mechanics into a holistic and multiscale research field that is able (i) to provide an in-depth understanding

of what drives these phenomena – both in the elastic and the inelastic regime, and (ii) to predict and identify MOF materials with exceptional mechanical behaviour that can be adopted for practical applications. It is my hope that the critical discussion herein, on both the technical aspects of the computational simulations of MOFs as well as on the mechanical phenomena that can be extracted from these simulations, not only summarises the current state-of-the-art in the research field but also forms an impetus to further its development into uncharted but undoubtedly exciting territories.

Acknowledgements

This work was supported by the Fund for Scientific Research Flanders (FWO) through a senior postdoctoral fellowship (grant no. 12T3522N) and the Research Board of Ghent University (BOF).

References

1. A. B. Cairns and A. L. Goodwin, *Phys. Chem. Chem. Phys.*, 2015, **17**, 20449.
2. N. C. Burtch, S. J. Baxter, J. Heinen, A. Bird, A. Schneemann, D. Dubbeldam and A. P. Wilkinson, *Adv. Funct. Mater.*, 2019, **29**, 1904669.
3. A. Schneemann, V. Bon, I. Schwedler, I. Senkovska, S. Kaskel and R. A. Fischer, *Chem. Soc. Rev.*, 2014, **43**, 6062.
4. T. D. Bennett, A. K. Cheetham, A. H. Fuchs and F.-X. Coudert, *Nat. Chem.*, 2017, **9**, 11.
5. M. J. Cliffe, W. Wan, X. Zou, P. A. Chater, A. K. Kleppe, M. G. Tucker, H. Wilhelm, N. P. Funnell, F.-X. Coudert and A. L. Goodwin, *Nat. Commun.*, 2014, **5**, 4176.
6. Y. Sakata, S. Furukawa, M. Kondo, K. Hirai, N. Horike, Y. Takashami, H. Uehara, N. Louvin, M. Meilikhov, T. Tsuruoka, S. Isoda, W. Kosaka, O. Sakata and S. Kitagawa, *Science*, 2013, **339**, 193.
7. J. P. Dürholt, R. Galvelis and R. Schmid, *Dalton Trans.*, 2016, **45**, 4370.
8. E. B. Tadmor and R. E. Miller, *Modeling Materials: Continuum, Atomistic and Multiscale Techniques*, Cambridge University Press, New York, 2011.
9. J. H. Irving and J. G. Kirkwood, *J. Chem. Phys.*, 1950, **18**, 817.
10. A. Cauchy, *Exercises du Mathématique*, Chez de Bure Frères, Paris, 1828, pp. 227–252.
11. A. Cauchy, *Exercises du Mathématique*, Chez de Bure Frères, Paris, 1828, pp. 253–277.
12. M. Born, *Atomtheorie des Festen Zustandes*, B. G. Teubner, Leipzig, 1923.
13. P. Steinmann, A. Elizondo and R. Sunyk, *Modell. Simul. Mater. Sci. Eng.*, 2007, **15**, S271.

14. T. Loiseau, C. Serre, C. Huguenard, G. Fink, F. Taulelle, M. Henry, T. Bataille and G. Férey, *Chem. – Eur. J.*, 2004, **10**, 1373.
15. J. R. Ray and A. Rahman, *J. Chem. Phys.*, 1984, **80**, 4423.
16. E. B. Tadmor, R. E. Miller and R. S. Elliott, *Continuum Mechanics and Thermodynamics: From Fundamental Concepts to Governing Equations*, Cambridge University Press, New York, 2014.
17. V. Van Speybroeck, S. Vandenhaute, A. E. J. Hoffman and S. M. J. Rogge, *Trends Chem.*, 2021, **3**, 605.
18. J. Keupp and R. Schmid, *Adv. Theory Simul.*, 2019, **2**, 1900117.
19. S. M. J. Rogge, M. Waroquier and V. Van Speybroeck, *Nat. Commun.*, 2019, **10**, 4842.
20. J. D. Evans, L. Bocquet and F.-X. Coudert, *Chem*, 2016, **1**, 873.
21. L. Kollias, D. C. Cantu, M. A. Tubbs, R. Rousseau, V.-A. Glezakou and M. Salvalaglio, *J. Am. Chem. Soc.*, 2019, **141**, 6073.
22. A. Ozcan, R. Semino, G. Maurin and A. O. Yazaydin, *Chem. Mater.*, 2020, **32**, 1288.
23. J. P. Dürholt, J. Keupp and R. Schmid, *Eur. J. Inorg. Chem.*, 2016, **2016**, 4517.
24. S. Vandenhaute, S. M. J. Rogge and V. Van Speybroeck, *Front. Chem.*, 2021, **9**, 718920.
25. Z. Fang, B. Bueken, D. E. De Vos and R. A. Fischer, *Angew. Chem., Int. Ed.*, 2015, **54**, 7234.
26. J. Fonseca, T. Gong, L. Jiao and H.-L. Jiang, *J. Mater. Chem. A*, 2021, **9**, 10562.
27. L. Valenzano, B. Civalleri, S. Chavan, S. Bordiga, M. H. Nilsen, S. Jakobsen, K. P. Lillerud and C. Lamberti, *Chem. Mater.*, 2011, **23**, 1700.
28. C. A. Trickett, K. J. Gagnon, S. Lee, F. Gándara, H.-B. Bürgi and O. M. Yaghi, *Angew. Chem., Int. Ed.*, 2015, **54**, 11162.
29. G. C. Shearer, S. Chavan, S. Bordiga, S. Svelle, U. Olsbye and K. P. Lillerud, *Chem. Mater.*, 2016, **28**, 3749.
30. W. Zhang, M. Kauer, P. Guo, S. Kunze, S. Cwik, M. Muhler, Y. Wang, K. Epp, G. Kieslich and R. A. Fischer, *Eur. J. Inorg. Chem.*, 2017, **2017**, 925.
31. O. Kozachuk, M. Meilikhov, K. Yusenko, A. Schneemann, B. Jee, A. V. Kuttatheyll, M. Bertmer, C. Sternemann, A. Pöppl and R. A. Fischer, *Eur. J. Inorg. Chem.*, 2013, **2013**, 4546.
32. D. N. Johnstone, F. C. N. Firth, C. P. Grey, P. A. Midgley, M. J. Cliffe and S. M. Collins, *J. Am. Chem. Soc.*, 2020, **142**, 13081.
33. S. Diring, S. Furukawa, Y. Takashima, T. Tsuruoka and S. Kitagawa, *Chem. Mater.*, 2010, **22**, 4531.
34. Z. Fang, J. P. Dürholt, M. Kauer, W. Zhang, C. Lochenie, B. Jee, B. Albada, N. Metzler-Nolte, A. Pöppl, B. Weber, M. Muhler, Y. Wang, R. Schmid and R. A. Fischer, *J. Am. Chem. Soc.*, 2014, **136**, 9627.
35. T. D. Bennett, T. K. Todorova, E. F. Baxter, D. G. Reid, C. Gervais, B. Bueken, B. Van de Voorde, D. De Vos, D. A. Keen and C. Mellot-Draznieks, *Phys. Chem. Chem. Phys.*, 2016, **18**, 2192.

36. K. W. Chapman, G. J. Halder and P. J. Chupas, *J. Am. Chem. Soc.*, 2009, **131**, 17546.
37. T. D. Bennett and A. K. Cheetham, *Acc. Chem. Res.*, 2014, **47**, 1555.
38. R. Gaillac, P. Pullumbu, K. A. Beyer, K. W. Chapman, D. A. Keen, T. D. Bennett and F.-X. Coudert, *Nat. Mater.*, 2017, **16**, 1149.
39. J. M. Tuffnell, C. A. Ashling, J. Hou, S. Li, L. Longley, M. L. Ríos Gómez and T. D. Bennett, *Chem. Commun.*, 2019, **55**, 8705.
40. L. Frentzel-Beyme, M. Kloß, P. Kolodzeiski, R. Pallach and S. Henke, *J. Am. Chem. Soc.*, 2019, **141**, 12362.
41. S. Horike, S. S. Nagarkar, T. Ogawa and S. Kitagawa, *Angew. Chem., Int. Ed.*, 2020, **59**, 6652.
42. J. D. Evans, V. Bon, I. Senkovska, H.-C. Lee and S. Kaskel, *Nat. Commun.*, 2020, **11**, 2690.
43. S. Borgmans, S. M. J. Rogge, J. S. De Vos, C. V. Stevens, P. Van Der Voort and V. Van Speybroeck, *Angew. Chem., Int. Ed.*, 2021, **60**, 8913.
44. S. Ehrling, E. M. Reynolds, V. Bon, I. Senkosvka, T. E. Gorelik, J. D. Evans, M. Rauche, M. Mendt, M. S. Weiss, A. Pöppl, E. Brunner, U. Kaiser, A. L. Goodwin and S. Kaskel, *Nat. Chem.*, 2021, **13**, 568.
45. J. H. Cavka, S. Jakobsen, U. Olsbye, N. Guillou, C. Lamberti, S. Bordiga and K. P. Lillerud, *J. Am. Chem. Soc.*, 2008, **42**, 13850.
46. K. Leus, T. Bogaerts, J. De Decker, H. Depauw, K. Hendrickx, H. Vrielinck, V. Van Speybroeck and P. Van Der Voort, *Microporous Mesoporous Mater.*, 2016, **226**, 110.
47. M. Kandiah, M. H. Nilsen, S. Usseglio, S. Jakobsen, U. Olsbye, M. Tilset, C. Larabi, E. A. Quadrelli, F. Bonino and K. P. Lillerud, *Chem. Mater.*, 2010, **22**, 6632.
48. A. W. Thornton, R. Babarao, F. Trousselet and F.-X. Coudert, *Dalton Trans.*, 2016, **45**, 4352.
49. S. M. J. Rogge, J. Wieme, L. Vanduyfhuys, S. Vandenbrande, G. Maurin, T. Verstraelen, M. Waroquier and V. Van Speybroeck, *Chem. Mater.*, 2016, **28**, 5721.
50. P. G. Yot, K. Yang, F. Ragon, V. Dmitriev, T. Devic, P. Horcajada, C. Serre and G. Maurin, *Dalton Trans.*, 2016, **45**, 4283.
51. A. Simonov and A. L. Goodwin, *Nat. Rev. Chem.*, 2020, **65**, 657.
52. S. Horike, S. Shimomura and S. Kitagawa, *Nat. Chem.*, 2009, **1**, 695.
53. S. Kenji, T. Satoshi and M. Wasuke, *Chem. Lett.*, 2001, **30**, 332.
54. D. N. Dybtsev, H. Chun and K. Kim, *Angew. Chem., Int. Ed.*, 2004, **43**, 5033.
55. A. M. Walker, B. Civalleri, B. Slater, C. Mellot-Draznieks, F. Corà, C. M. Zicovich-Wilson, G. Román-Pérez, J. M. Soler and J. D. Gale, *Angew. Chem., Int. Ed.*, 2010, **49**, 7501.
56. J. S. Grosch and F. Paesani, *J. Am. Chem. Soc.*, 2012, **134**, 4207.
57. N. Klein, C. Herzog, M. Sabo, I. Senkovska, J. Getzschmann, S. Paasch, M. R. Lohe, E. Brunner and S. Kaskel, *Phys. Chem. Chem. Phys.*, 2010, **12**, 11778.

58. A. Krylov, I. Senkovska, S. Ehrling, M. Maliuta, S. Krylova, E. Slyusareva, A. Vtyurin and S. Kaskel, *Chem. Commun.*, 2020, **56**, 8269.
59. R. Semino, J. P. Dürholt, R. Schmid and G. Maurin, *J. Phys. Chem. C*, 2017, **121**, 21491.
60. S. M. J. Rogge, *Faraday Discuss.*, 2021, **225**, 271.
61. J. D. Evans and F.-X. Coudert, *J. Phys. Chem. Lett.*, 2017, **8**, 1578.
62. Z. Wang, K. M. Schmalbach, R. L. Combs, Y. Chen, R. L. Penn, N. A. Mara and A. Stein, *ACS Appl. Mater. Interfaces*, 2020, **12**, 49971.
63. F.-X. Coudert and A. H. Fuchs, *Coord. Chem. Rev.*, 2016, **307**, 211.
64. E. Schrödinger, *Ann. Phys.*, 1926, **384**, 361.
65. M. Born and R. Oppenheimer, *Ann. Phys.*, 1927, **389**, 457.
66. S. O. Odoh, C. J. Cramer, D. G. Truhlar and L. Gagliardi, *Chem. Rev.*, 2015, **115**, 6051.
67. D. S. Sholl and J. A. Steckel, *Density Functional Theory: A Practical Introduction*, John Wiley & Sons, Inc., Hoboken, 2009.
68. P. Hohenberg and W. Kohn, *Phys. Rev. B*, 1964, **136**, 864.
69. W. Kohn and L. J. Sham, *Phys. Rev. A*, 1965, **140**, 1133.
70. J. L. Mancuso, A. M. Mroz, K. N. Le and C. H. Hendon, *Chem. Rev.*, 2020, **120**, 8641.
71. J. A. Greathouse and M. D. Allendorf, *J. Am. Chem. Soc.*, 2006, **128**, 10678.
72. S. Bureekaew, S. Amirjalayer, M. Tafipolsky, C. Spickermann, T. K. Roy and R. Schmid, *Phys. Status Solidi B*, 2013, **250**, 1128.
73. J. P. Dürholt, G. Fraux, F.-X. Coudert and R. Schmid, *J. Chem. Theory Comput.*, 2019, **15**, 2420.
74. J. K. Bristow, D. Tiana and A. Walsh, *J. Chem. Theory Comput.*, 2014, **10**, 4644.
75. L. Vanduyfhuys, S. Vandenbrande, T. Verstraelen, R. Schmid, M. Waroquier and V. Van Speybroeck, *J. Comput. Chem.*, 2015, **36**, 1015.
76. L. Vanduyfhuys, S. Vandenbrande, J. Wieme, M. Waroquier, T. Verstraelen and V. Van Speybroeck, *J. Comput. Chem.*, 2018, **39**, 999.
77. J. K. Bristow, J. M. Skelton, K. L. Svane, A. Walsh and J. D. Gale, *Phys. Chem. Chem. Phys.*, 2016, **18**, 29316.
78. J. Heinen, N. C. Burtch, K. S. Walton and D. Dubbeldam, *J. Chem. Theory Comput.*, 2017, **13**, 3722.
79. J. Heinen and D. Dubbeldam, *Wiley Interdiscip. Rev. Comput. Mol. Sci.*, 2018, **8**, e1363.
80. D. Frenkel and B. Smit, *Understanding Molecular Simulation: From Algorithms to Applications*, Elsevier, London, 2012.
81. S. Nosé and M. L. Klein, *Mol. Phys.*, 1983, **50**, 1055.
82. J. R. Ray, *Comput. Phys. Rep.*, 1988, **8**, 109.
83. S. M. J. Rogge, L. Vanduyfhuys, A. Ghysels, M. Waroquier, T. Verstraelen, G. Maurin and V. Van Speybroeck, *J. Chem. Theory Comput.*, 2015, **11**, 5583.
84. H. C. Andersen, *J. Chem. Phys.*, 1980, **72**, 2384.

85. M. Parrinello and A. Rahman, *Phys. Rev. Lett.*, 1980, **45**, 1196.
86. M. Parrinello and A. Rahman, *J. Appl. Phys.*, 1981, **52**, 7182.
87. J. R. Ray, *J. Chem. Phys.*, 1983, **79**, 5128.
88. J. R. Ray and A. Rahman, *J. Chem. Phys.*, 1985, **82**, 4243.
89. C. L. Cleveland, *J. Chem. Phys.*, 1988, **89**, 4987.
90. R. M. Wentzcovitch, *Phys. Rev. B*, 1991, **44**, 2358.
91. J. V. Lill and J. Q. Broughton, *Phys. Rev. B*, 1992, **46**, 12068.
92. R. E. Miller, E. B. Tadmor, J. S. Gibson, N. Bernstein and F. Pavia, *J. Chem. Phys.*, 2016, **144**, 184107.
93. H. J. C. Berendsen, J. P. M. Postma, W. F. van Gunsteren, A. DiNola and J. R. Haak, *J. Chem. Phys.*, 1984, **81**, 3684.
94. W. G. Hoover, *Phys. Rev. A*, 1986, **34**, 2499.
95. S. Melchionna, G. Ciccotti and B. L. Holian, *Mol. Phys.*, 1993, **78**, 533.
96. G. J. Martyna, D. J. Tobias and M. L. Klein, *J. Chem. Phys.*, 1994, **101**, 4177.
97. D. Quigley and M. I. J. Probert, *J. Chem. Phys.*, 2004, **120**, 11432.
98. N. C. Burtch, J. Heinen, T. D. Bennett, D. Dubbeldam and M. D. Allendorf, *Adv. Mater.*, 2018, **30**, 1704124.
99. J. F. Nye, *Physical Properties of Crystals: Their Representation by Tensors and Matrices*, University Press, Oxford, 2006.
100. W. Voigt, *Lehrbuch der Kristallphysik*, B. G. Teubner, Leipzig, 1910.
101. A. Marmier, Z. A. D. Lethbridge, R. I. Walton, C. W. Smith, S. C. Parker and K. E. Evans, *Comput. Phys. Commun.*, 2010, **181**, 2102.
102. R. Gaillac, P. Pullumbi and F.-X. Coudert, *J. Phys.: Condens. Matter*, 2016, **28**, 275201.
103. A. Reuss, *Z. Angew. Math. Mech.*, 1929, **9**, 49.
104. R. Hill, *Proc. Phys. Soc., London, Sect. A*, 1952, **65**, 349.
105. Y. Le Page and P. Saxe, *Phys. Rev. B*, 2001, **63**, 174103.
106. F. D. Murnaghan, *Proc. Natl. Acad. Sci. U. S. A.*, 1944, **30**, 244.
107. F. Birch, *Phys. Rev.*, 1947, **71**, 809.
108. P. Vinet, J. H. Rose, J. Ferrante and J. R. Smith, *J. Phys.: Condens. Matter*, 1989, **1**, 1941.
109. D. E. P. Vanpoucke, K. Lejaeghere, V. Van Speybroeck, M. Waroquier and A. Ghysels, *J. Phys. Chem. C*, 2015, **119**, 23752.
110. X. Wu, D. Vanderbilt and D. R. Hamann, *Phys. Rev. B*, 2005, **72**, 035105.
111. J. F. Lutsko, *J. Appl. Phys.*, 1989, **65**, 2991.
112. J. Maul, M. R. Ryder, M. T. Ruggiero and A. Erba, *Phys. Rev. B*, 2019, **99**, 014102.
113. H. Li, M. Eddaoudi, M. O'Keeffe and O. M. Yaghi, *Nature*, 1999, **402**, 276.
114. N. L. Rosi, J. Eckert, M. Eddaoudi, D. T. Vodak, J. Kim, M. O'Keeffe and O. M. Yaghi, *Science*, 2003, **300**, 1127.
115. M. J. Mehl, *Phys. Rev. B*, 1993, **47**, 2493.
116. M. Mattesini, J. M. Soler and F. Ynduráin, *Phys. Rev. B*, 2006, **73**, 094111.
117. A. Samanta, T. Furuta and J. Li, *J. Chem. Phys.*, 2006, **125**, 084714.
118. W. Zhou and T. Yildirim, *Phys. Rev. B*, 2006, **74**, 180301.

119. D. F. Bahr, J. A. Reid, W. M. Mook, C. A. Bauer, R. Stumpf, A. J. Skulan, N. R. Moody, B. A. Simmons, M. M. Shindel and M. D. Allendorf, *Phys. Rev. B*, 2007, **76**, 184106.
120. K. Banlusan and A. Strachan, *J. Chem. Phys.*, 2017, **146**, 184705.
121. D. Nazarian, P. Ganesh and D. S. Sholl, *J. Mater. Chem. A*, 2015, **3**, 22432.
122. J. P. Perdew, K. Burke and M. Ernzerhof, *Phys. Rev. Lett.*, 1996, **77**, 3865.
123. S. Grimme, J. Antony, S. Ehrlich and H. Krieg, *J. Chem. Phys.*, 2010, **132**, 154104.
124. J. L. C. Rowsell, E. C. Spencer, J. Eckert, J. A. K. Howard and O. M. Yaghi, *Science*, 2005, **309**, 1350.
125. S. S. Han and W. A. Goddard III, *J. Phys. Chem. C*, 2007, **111**, 15185.
126. J. A. Greathouse and M. D. Allendorf, *J. Phys. Chem. C*, 2008, **112**, 5795.
127. M. Tafipolsky and R. Schmid, *J. Phys. Chem. B*, 2009, **113**, 1341.
128. M. M. Biswas and T. Cagin, *Mater. Chem. Phys.*, 2011, **131**, 44.
129. D. Dubbeldam, R. Krishna and R. Q. Snurr, *J. Phys. Chem. C*, 2009, **113**, 19317.
130. S. L. Mayo, B. D. Olafson and W. A. Goddard, *J. Phys. Chem.*, 1990, **94**, 8897.
131. P. Dauber-Osguthorpe, V. A. Roberts, D. J. Osguthorpe, J. Wolff, M. Genest and A. T. Hagler, *Proteins*, 1988, **4**, 31.
132. P. G. Boyd, S. M. Moosavi, M. Witman and B. Smit, *J. Phys. Chem. Lett.*, 2017, **8**, 357.
133. A. K. Rappe, C. J. Casewit, K. S. Colwell, W. A. Goddard III and W. M. Skiff, *J. Am. Chem. Soc.*, 1992, **114**, 10024.
134. M. A. Addicoat, N. Vankova, I. F. Akter and T. Heine, *J. Chem. Theory Comput.*, 2014, **10**, 880.
135. D. Dubbeldam, K. S. Walton, D. E. Ellis and R. Q. Snurr, *Angew. Chem., Int. Ed.*, 2007, **46**, 4496.
136. S. M. J. Rogge, M. Waroquier and V. Van Speybroeck, *Acc. Chem. Res.*, 2018, **51**, 138.
137. S. S. Kaye, A. Dailly, O. M. Yaghi and J. R. Long, *J. Am. Chem. Soc.*, 2007, **129**, 14176.
138. Y. Ming, J. Purewal, J. Yang, C. Xu, R. Soltis, J. Warner, M. Veenstra, M. Gaab, U. Müller and D. J. Siegel, *Langmuir*, 2015, **31**, 4988.
139. J. C. Tan and A. K. Cheetham, *Chem. Soc. Rev.*, 2011, **40**, 1059.
140. A. Kuc, A. Enyashin and G. Seifert, *J. Phys. Chem. B*, 2007, **111**, 8179.
141. P. Z. Moghadam, S. M. J. Rogge, A. Li, C.-M. Chow, J. Wieme, N. Moharrami, M. Aragones-Anglada, G. Conduit, D. A. Gomez-Gualdron, V. Van Speybroeck and D. Fairen-Jimenez, *Matter*, 2019, **1**, 219.
142. B. Lukose, B. Supronowicz, S. P. P. J. Frenzel, A. B. Kuc, G. Seifert, G. N. Vayssilov and T. Heine, *Phys. Status Solidi B*, 2012, **249**, 335.
143. L.-M. Yang, P. Vajeeston, P. Ravindran, H. Fjellvåg and M. Tilset, *Inorg. Chem.*, 2010, **49**, 10283.
144. J. D. Evans and F.-X. Coudert, *J. Am. Chem. Soc.*, 2016, **138**, 6131.
145. M. Fuentes-Cabrera, D. M. Nicholson and B. G. Sumpter, *J. Chem. Phys.*, 2005, **123**, 124713.

146. L.-M. Yang, P. Vajeeston, P. Ravindran, H. Fjellvåg and M. Tilset, *Phys. Chem. Chem. Phys.*, 2011, **13**, 10191.
147. L.-M. Yang, P. Ravindran, P. Vajeeston and M. Tilset, *RSC Adv.*, 2012, **2**, 1618.
148. L.-M. Yang, P. Ravindran, P. Vajeeston and M. Tilset, *Phys. Chem. Chem. Phys.*, 2012, **14**, 4713.
149. L.-M. Yang, P. Ravindran, P. Vajeeston and M. Tilset, *J. Mater. Chem.*, 2012, **22**, 16324.
150. L. Yang, M. P. Ravindran and M. Tilset, *Inorg. Chem.*, 2013, **52**, 4217.
151. L.-M. Yang, P. Ravindran, P. Vajeeston, S. Svelle and M. Tilset, *Microporous Mesoporous Mater.*, 2013, **175**, 50.
152. L.-M. Yang, *Microporous Mesoporous Mater.*, 2014, **183**, 218.
153. L.-M. Yang, G.-Y. Fang, J. Ma, E. Ganz and S. S. Han, *Cryst. Growth Des.*, 2014, **14**, 2532.
154. L.-M. Yang, G.-Y. Fang, J. Ma, R. Pushpa and E. Ganz, *Phys. Chem. Chem. Phys.*, 2016, **18**, 32319.
155. A. J. Graham, D. R. Allan, A. Muszkiewicz, C. A. Morrison and S. A. Moggach, *Angew. Chem., Int. Ed.*, 2011, **50**, 11138.
156. J. Joo, H. Kim and S. S. Han, *Phys. Chem. Chem. Phys.*, 2013, **15**, 18822.
157. M. R. Ryder, J. Maul, B. Civalleri and A. Erba, *Adv. Theory Simul.*, 2019, **2**, 1900093.
158. J. P. Perdew, A. Ruzsinszky, G. I. Csonka, O. A. Vydrov, G. E. Scuseria, L. A. Constantin, X. Zhou and K. Burke, *Phys. Rev. Lett.*, 2008, **100**, 136406.
159. R. Dovesi, R. Orlando, A. Erba, C. M. Zicovich-Wilson, B. Civalleri, S. Casassa, L. Maschio, M. Ferrabone, M. De La Pierre, P. D'Arco, Y. Noël, M. Causà, M. Rérat and B. Kirtman, *Int. J. Quantum Chem.*, 2014, **114**, 1287.
160. R. E. Allen and F. W. De Wette, *Phys. Rev.*, 1969, **179**, 873.
161. L. Wang, C. Wang, Y. Sun, K. Shi, S. Deng and H. Lu, *Mater. Chem. Phys.*, 2016, **175**, 138.
162. Y.-Q. Tian, C.-X. Cai, X.-M. Ren, C.-Y. Duan, Y. Xu, S. Gao and X.-Z. You, *Chem. – Eur. J.*, 2003, **9**, 5673.
163. K. S. Park, Z. Ni, A. P. Côté, J. Y. Choi, R. Huang, F. J. Uribe-Romo, H. K. Chae, M. O'Keeffe and O. M. Yaghi, *Proc. Natl. Acad. Sci. U. S. A.*, 2006, **103**, 10186.
164. T. D. Bennett, J.-C. Tan, S. A. Moggach, R. Galvelis, C. Mellot-Draznieks, B. A. Reisner, A. Thirumurugan, D. R. Allan and A. K. Cheetham, *Chem. Eur. J.*, 2010, **16**, 10684.
165. J.-C. Tan, B. Civalleri, C.-C. Lin, L. Valenzano, R. Galvelis, P.-F. Chen, T. D. Bennett, C. Mellot-Draznieks, C. M. Zicovich-Wilson and A. K. Cheetham, *Phys. Rev. Lett.*, 2012, **108**, 095502.
166. A. D. Becke, *J. Chem. Phys.*, 1993, **98**, 1372.
167. R. Dovesi, R. Orlando, B. Civalleri, C. Roetti, V. R. Saunders and C. M. Zicovich-Wilson, *Z. Kristallogr. Cryst. Mater.*, 2005, **220**, 571.
168. T. Weng and J. R. Schmidt, *J. Phys. Chem. A*, 2019, **123**, 3000.

169. W. Zhang, J. Maul, D. Vulpe, P. Z. Moghadam, D. Fairen-Jimenez, D. M. Mittleman, J. A. Zeitler, A. Erba and M. T. Ruggiero, *J. Phys. Chem. C*, 2018, **122**, 27442.
170. Y. Zhao and D. G. Truhlar, *Theor. Chem. Acc.*, 2008, **120**, 215.
171. H. Gao, W. Wei, L. Dong, G. Feng, X. Jiang, R. Wu, Z. Lin and W. Li, *Crystals*, 2017, **7**, 99.
172. J.-C. Tan, B. Civalleri, A. Erba and E. Albanese, *CrystEngComm*, 2015, **17**, 375.
173. M. R. Ryder and J.-C. Tan, *Dalton Trans.*, 2016, **45**, 4154.
174. B. Zheng, Y. Zhu, F. Fu, L. L. Wang, J. Wang and H. Du, *RSC Adv.*, 2017, **66**, 41499.
175. S. M. Moosavi, P. G. Boyd, L. Sarkisov and B. Smit, *ACS Cent. Sci.*, 2018, **4**, 832.
176. L. Zhang, Z. Hu and J. Jiang, *J. Phys. Chem. C*, 2012, **116**, 19268.
177. H. Wu, T. Yildirim and W. Zhou, *J. Phys. Chem. Lett.*, 2013, **4**, 925.
178. C. L. Hobday, R. J. Marshall, C. F. Murphie, J. Sotelo, T. Richards, D. R. Allan, T. Düren, F.-X. Coudert, R. S. Forgan, C. A. Morrison, S. A. Moggach and T. D. Bennett, *Angew. Chem., Int. Ed.*, 2016, **55**, 2401.
179. L.-M. Yang, E. Ganz, S. Svelle and M. Tilset, *J. Mater. Chem. C*, 2014, **2**, 7111.
180. L. R. Redfern, M. Ducamp, M. C. Wasson, L. Robison, F. A. Son, F.-X. Coudert and O. K. Farha, *Chem. Mater.*, 2020, **32**, 5864.
181. M. Vandichel, J. Hajek, A. Ghysels, A. De Vos, M. Waroquier and V. Van Speybroeck, *CrystEngComm*, 2016, **18**, 7056.
182. S. M. J. Rogge, P. G. Yot, J. Jacobsen, F. Muniz-Miranda, S. Vandenbrande, J. Gosch, V. Ortiz, I. E. Collings, S. Devautour-Vinot, G. Maurin, N. Stock and V. Van Speybroeck, *ACS Mater. Lett.*, 2020, **2**, 438.
183. S. S.-Y. Chui, S. M.-F. Lo, J. P. H. Charmant, A. G. Orpen and I. D. Williams, *Science*, 1999, **283**, 1148.
184. J. P. Perdew and Y. Wang, *Phys. Rev. B*, 1992, **23**, 13244.
185. T. Watanabe and D. S. Sholl, *J. Chem. Phys.*, 2010, **133**, 094509.
186. M. Tafipolsky, S. Amirjalayer and R. Schmid, *J. Phys. Chem. C*, 2010, **114**, 14402.
187. L. Zhao, Q. Yang, Q. Ma, C. Zhong, J. Mi and D. Liu, *J. Mol. Model.*, 2011, **17**, 227.
188. M. R. Ryder, B. Civalleri, G. Cinque and J.-C. Tan, *CrystEngComm*, 2016, **18**, 4303.
189. K. Barthelet, J. Marrot, D. Riou and G. Férey, *Angew. Chem., Int. Ed.*, 2002, **41**, 281.
190. F. Millange, C. Serre and G. Férey, *Chem. Commun.*, 2002, **8**, 822.
191. P. G. Yot, Q. Ma, J. Haines, Q. Yang, A. Ghoufi, T. Devic, C. Serre, V. Dmitriev, G. Férey, C. Zhong and G. Maurin, *Chem. Sci.*, 2012, **3**, 1100.
192. I. Beurroies, M. Boulhout, P. L. Llewellyn, B. Kuchta, G. Férey, C. Serre and R. Denoyel, *Angew. Chem., Int. Ed.*, 2010, **49**, 7526.
193. G. Férey and C. Serre, *Chem. Soc. Rev.*, 2009, **38**, 1380.

194. R. Caruana-Gauci, E. P. Degabriele, D. Attard and J. N. Grima, *J. Mater. Sci.*, 2018, **53**, 5079.
195. J. M. Ogborn, I. E. Collings, S. A. Moggach, A. L. Thompson and A. L. Goodwin, *Chem. Sci.*, 2012, **3**, 3011.
196. A. U. Ortiz, A. Boutin, A. H. Fuchs and F.-X. Coudert, *Phys. Rev. Lett.*, 2012, **109**, 195502.
197. A. U. Ortiz, A. Boutin, A. H. Fuchs and F.-X. Coudert, *J. Chem. Phys.*, 2013, **138**, 174703.
198. J. Heinen and D. Dubbeldam, *Dalton Trans.*, 2016, **45**, 4309.
199. P. Ramaswamy, J. Wieme, E. Alvarez, L. Vanduyfhuys, J.-P. Itié, P. Fabry, V. Van Speybroeck, C. Serre, P. G. Yot and G. Maurin, *J. Mater. Chem. A*, 2017, **5**, 11047.
200. M. Wang, X. Zhang, Y. Chen and D. Li, *J. Phys. Chem. C*, 2016, **120**, 5059.
201. F. Mouhat, D. Bousquet, A. Boutin, L. Bouëssel du Bourg, F.-X. Coudert and A. H. Fuchs, *J. Phys. Chem. Lett.*, 2015, **6**, 4265.
202. Q. Ma, Q. Yang, A. Ghoufi, G. Férey, C. Zhong and G. Maurin, *Dalton Trans.*, 2012, **41**, 3915.
203. Y.-Y. Liu, S. Couck, M. Vandichel, M. Grzywa, K. Leus, S. Biswas, D. Volkmer, J. Gascon, F. Kapteijn, J. F. M. Denayer, M. Waroquier, V. Van Speybroeck and P. Van Der Voort, *Inorg. Chem.*, 2013, **52**, 113.
204. J. Wieme, L. Vanduyfhuys, S. M. J. Rogge, M. Waroquier and V. Van Speybroeck, *J. Phys. Chem. C*, 2016, **120**, 14934.
205. D. E. P. Vanpoucke, J. W. Jaeken, S. De Baerdemacker, K. Lejaeghere and V. Van Speybroeck, *Beilstein J. Nanotechnol.*, 2014, **5**, 1738.
206. A. E. J. Hoffman, J. Wieme, S. M. J. Rogge, L. Vanduyfhuys and V. Van Speybroeck, *Z. Kristallogr.*, 2019, **234**, 529.
207. C. Volkringer, T. Loiseau, N. Guillou, G. Férey and E. Elkaïm, *Solid State Sci.*, 2009, **11**, 1507.
208. V. Guillerm, F. Ragon, M. Dan-Hardi, T. Devic, M. Vishnuvarthan, B. Campo, A. Vimont, G. Clet, Q. Yang, G. Maurin, G. Férey, A. Vittadini, S. Gross and C. Serre, *Angew. Chem., Int. Ed.*, 2012, **51**, 9267.
209. M. R. Ryder, B. Civalleri and J.-C. Tan, *Phys. Chem. Chem. Phys.*, 2016, **18**, 9079.
210. H. C. Dong, H. L. Nguyen, H. M. Le, N. Thoai, Y. Kawazoe and D. Nguyen-Manh, *Sci. Rep.*, 2018, **8**, 16651.
211. N. Klein, I. Senkovska, I. A. Baburin, R. Grünker, U. Stoeck, M. Schlichtenmayer, B. Streppel, U. Mueller, S. Leoni, M. Hirscher and S. Kaskel, *Chem. – Eur. J.*, 2011, **17**, 13007.
212. Z. Wang, J. Liu, B. Lukose, Z. Gu, P. G. Weidler, H. Gliemann, T. Heine and C. Wöll, *Nano Lett.*, 2014, **14**, 1526.
213. N. Li, K. Blankson, Y. Yang, P. Zhang and X. Zhao, *APL Mater.*, 2020, **8**, 111101.
214. S. Krause, V. Bon, I. Senkovska, U. Stoeck, D. Wallacher, D. M. Többens, S. Zander, R. S. Pillai, G. Maurin, F.-X. Coudert and S. Kaskel, *Nature*, 2016, **532**, 348.

215. J. Wieme, S. M. J. Rogge, P. G. Yot, L. Vanduyfhuys, S.-K. Lee, J.-S. Chang, M. Waroquier, G. Maurin and V. Van Speybroeck, *J. Mater. Chem. A*, 2019, **7**, 22663.
216. A. U. Ortiz, A. Boutin, K. J. Gagnon, A. Clearfield and F.-X. Coudert, *J. Am. Chem. Soc.*, 2014, **136**, 11540.
217. X. Yang, L. Si, G. Xie, L. Zhang, D. Guo and J. Luo, *Comput. Mater. Sci.*, 2020, **177**, 109543.
218. Z. Zheng, X. Jiang and J. Zhao, *Chem. Phys. Lett.*, 2015, **628**, 76.
219. E. V. Alexandrov, A. V. Goltsev, R. A. Eremin and V. A. Blatov, *J. Phys. Chem. C*, 2019, **123**, 24651.
220. V. A. Saleev and A. V. Shipilova, *Russ. J. Phys. Chem. A*, 2018, **92**, 1940.
221. A. Gładysiak, K. S. Deeg, I. Dovgaliuk, A. Chidambaram, K. Ordiz, P. G. Boyd, S. M. Moosavi, D. Ongari, J. A. R. Navarro, B. Smit and K. C. Stylianou, *ACS Appl. Mater. Interfaces*, 2018, **10**, 36144.
222. P. Canepa, K. Tan, Y. Du, H. Lu, Y. J. Chabal and T. Thonhauser, *J. Mater. Chem. A*, 2015, **3**, 986.
223. M. Wittman, S. Ling, A. Gladysiak, K. C. Stylianou, B. Smit, B. Slater and M. Haranczyk, *J. Phys. Chem. C*, 2017, **121**, 1171.
224. A. U. Ortiz, A. Boutin and F.-X. Coudert, *Chem. Commun.*, 2014, **50**, 5867.
225. F. Niekiel, J. Lannoeye, H. Reinsch, A. S. Munn, A. Heerwig, I. Zizak, S. Kaskel, R. I. Walton, D. de Vos, P. Llewellyn, A. Lieb, G. Maurin and N. Stock, *Inorg. Chem.*, 2014, **53**, 4610.
226. R. Anderson and D. A. Gómez-Gualdrón, *CrystEngComm*, 2019, **21**, 1653.
227. G. Feng, X. Jiang, W. Wei, P. Gong, L. Kang, Z. Li, Y. Li, X. Li, X. Wu, Z. Lin, W. Li and P. Lu, *Dalton Trans.*, 2016, **45**, 4303.
228. I. M. Hönicke, I. Senkovska, V. Bon, I. A. Baburin, N. Bönisch, S. Raschke, J. D. Evans and S. Kaskel, *Angew. Chem., Int. Ed.*, 2018, **57**, 13780.
229. M. Parrinello and A. Rahman, *J. Chem. Phys.*, 1982, **76**, 2662.
230. J. R. Ray, *J. Appl. Phys.*, 1982, **53**, 6441.
231. J. R. Ray, M. C. Moody and A. Rahman, *Phys. Rev. B*, 1985, **32**, 733.
232. D. R. Squire, A. C. Holt and W. G. Hoover, *Physica*, 1969, **42**, 388.
233. K. Van Workum, K. Yoshimoto, J. J. de Pablo and J. F. Douglas, *Phys. Rev. E*, 2005, **71**, 061102.
234. K. Van Workum, G. Gao, J. D. Schall and J. A. Harrison, *J. Chem. Phys.*, 2006, **125**, 144506.
235. A. U. Ortiz, A. Boutin, A. H. Fuchs and F.-X. Coudert, *J. Phys. Chem. Lett.*, 2013, **4**, 1861.
236. P. Ying, J. Zhang, X. Zhang and Z. Zhong, *J. Phys. Chem. C*, 2020, **124**, 6274.
237. P. Ying, J. Zhang and Z. Zhong, *Microporous Mesoporous Mater.*, 2021, **312**, 110765.
238. J. Heinen, A. D. Ready, T. D. Bennett, D. Dubbeldam, R. W. Friddle and N. C. Burtch, *ACS Appl. Mater. Interfaces*, 2018, **10**, 21079.

239. P. Ying, J. Zhang and Z. Zhong, *J. Phys. Chem. C*, 2021, **125**, 12991.
240. F. Trousselet, A. Boutin and F.-X. Coudert, *Chem. Mater.*, 2015, **27**, 4422.
241. C. Zener, *Elasticity and Anelasticity of Metals*, University of Chicago Press, Chicago, 1948.
242. A. Schmitz, M. Chandrasekaran, G. GHosh and L. Delaey, *Acta Metall.*, 1989, **37**, 3151.
243. C.-S. Man, *J. Elastoplast.*, 1995, **39**, 165.
244. L. Sarkisov, R. L. Martin, M. Haranczyk and B. Smit, *J. Am. Chem. Soc.*, 2014, **136**, 2228.
245. P. M. Marcus, H. Ma and S. L. Qiu, *J. Phys.: Condens. Matter*, 2002, **14**, 525.
246. D. C. Wallace, *Phys. Rev.*, 1967, **162**, 776.
247. T. H. K. Barron and M. L. Klein, *Proc. Phys. Soc., London*, 1965, **85**, 523.
248. P. M. Marcus and S. L. Qiu, *J. Phys.: Condens. Matter*, 2009, **21**, 115401.
249. Z. Zhou and B. Joós, *Phys. Rev. B*, 2002, **66**, 054101.
250. Z. Zhou, *Chin. J. Phys.*, 2004, **42**, 21.
251. M. Born, *Math. Proc. Cambridge Philos. Soc.*, 1940, **36**, 160.
252. F. Mouhat and F.-X. Coudert, *Phys. Rev. B*, 2014, **90**, 224104.
253. J. Wang, S. Yip, S. R. Phillpot and D. Wolf, *Phys. Rev. Lett.*, 1993, **71**, 4182.
254. J. Wang, J. Li, S. P. S. Yip and D. Wolf, *Phys. Rev. B*, 1995, **52**, 12627.
255. Z. Zhou and B. Joós, *Phys. Rev. B*, 1996, **54**, 3841.
256. M. R. Ryder, B. Civalleri, T. D. Bennett, S. Henke, S. Rudić, G. Cinque, F. Fernandez-Alonso and J.-C. Tan, *Phys. Rev. Lett.*, 2014, **113**, 215502.
257. P. Zhao, G. I. Lampronti, G. O. Lloyd, M. T. Wharmby, S. Facq, A. K. Cheetham and S. A. T. Redfern, *Chem. Mater.*, 2014, **26**, 1767.
258. S. A. Moggach, T. D. Bennett and A. K. Cheetham, *Angew. Chem., Int. Ed.*, 2009, **48**, 7087.
259. H. Fang, M. T. Dove, L. H. N. Rimmer and A. J. Misquitta, *Phys. Rev. B*, 2013, **88**, 104306.
260. S. Krause, N. Hosono and S. Kitagawa, *Angew. Chem., Int. Ed.*, 2020, **59**, 15325.
261. A. Ghoufi, A. Subercaze, Q. Ma, P. G. Yot, Y. Ke, I. Puente-Orench, T. Devic, V. Guillerm, C. Zhong, C. Serre, G. Férey and G. Maurin, *J. Phys. Chem. C*, 2012, **116**, 13289.
262. Q. Ma, Q. Yang, A. Ghoufi, K. Yang, M. Lei, G. Férey, C. Zhong and G. Maurin, *J. Mater. Chem. A*, 2014, **2**, 9691.
263. A. V. Neimark, F. X. Coudert, A. Boutin and A. H. Fuchs, *J. Phys. Chem. Lett.*, 2010, **1**, 445.
264. C. Serre, S. Bourrelly, A. Vimont, N. A. Ramsahye, G. Maurin, P. L. Llewellyn, M. Daturi, Y. Filinchuk, O. Leynaud, P. Barnes and G. Férey, *Adv. Mater.*, 2007, **19**, 2246.
265. P. G. Yot, Z. Boudene, J. Macia, D. Granier, L. Vanduyfhuys, T. Verstraelen, V. Van Speybroeck, T. Devic, C. Serre, G. Férey, N. Stock and G. Maurin, *Chem. Commun.*, 2014, **50**, 9462.

266. V. Haigis, Y. Belkhodja, F.-X. Coudert, R. Vuilleumier and A. Boutin, *J. Chem. Phys.*, 2014, **141**, 064703.
267. L. D. Landau and E. M. Lifshitz, Course of Theoretical Physics, *Statistic Physics, Part 1*, Elsevier, Oxford, 2011, vol. 5.
268. E. Cockayne, *J. Phys. Chem. C*, 2017, **121**, 4312.
269. J. Wieme, K. Lejaeghere, G. Kresse and V. Van Speybroeck, *Nat. Commun.*, 2018, **9**, 4899.
270. P. G. Yot, L. Vanduyfhuys, E. Alvarez, J. Rodriguez, J.-P. Itié, P. Fabry, N. Guillou, T. Devic, I. Beurroies, P. L. Llewellyn, V. Van Speybroeck, C. Serre and G. Maurin, *Chem. Sci.*, 2016, **7**, 446.
271. R. Demuynck, S. M. J. Rogge, L. Vanduyfhuys, J. Wieme, M. Waroquier and V. Van Speybroeck, *J. Chem. Theory Comput.*, 2017, **13**, 5861.
272. P. Iacomi, J. S. Lee, L. Vanduyfhuys, K. H. Cho, P. Fertey, J. Wieme, D. Granier, G. Maurin, V. Van Speybroeck, J.-S. Chang and P. G. Yot, *Chem. Sci.*, 2021, **12**, 5682.
273. C. L. Hobday and G. Kieslich, *Dalton Trans.*, 2021, **50**, 3759.
274. L. Vanduyfhuys, S. M. J. Rogge, J. Wieme, S. Vandenbrande, G. Maurin, M. Waroquier and V. Van Speybroeck, *Nat. Commun.*, 2018, **9**, 204.
275. G. Bussi and A. Laio, *Nat. Rev. Phys.*, 2020, **2**, 200.
276. A. Laio and M. Parrinello, *Proc. Natl. Acad. Sci. U. S. A.*, 2002, **99**, 12562.
277. G. M. Torrie and J. P. Valleau, *J. Comput. Phys.*, 1977, **23**, 187.
278. M. R. Shirts and J. D. Chodera, *J. Chem. Phys.*, 2008, **129**, 124105.
279. J. G. Kirkwood, *J. Chem. Phys.*, 1935, **3**, 300.
280. R. W. Zwanzig, *J. Chem. Phys.*, 1954, **22**, 1420.
281. S. M. J. Rogge, S. Caroes, R. Demuynck, M. Waroquier, V. Van Speybroeck and A. Ghysels, *J. Chem. Theory Comput.*, 2018, **14**, 1186.
282. R. Demuynck, J. Wieme, S. M. J. Rogge, K. D. Dedecker, L. Vanduyfhuys, M. Waroquier and V. Van Speybroeck, *J. Chem. Theory Comput.*, 2018, **14**, 5511.
283. P. St. Petkov, V. Bon, C. L. Hobday, A. B. Kuc, P. Melix, S. Kaskel, T. Düren and T. Heine, *Phys. Chem. Chem. Phys.*, 2019, **21**, 674.
284. S. Henke, A. Schneemann, A. Wütscher and R. A. Fischer, *J. Am. Chem. Soc.*, 2012, **134**, 9464.
285. J. Keupp, J. P. Dürholt and R. Schmid, *Faraday Discuss.*, 2021, **225**, 324.
286. P. Vervoorts, J. Keupp, A. Schneemann, C. L. Hobday, D. Daisenberger, R. A. Fischer, R. Schmid and G. Kieslich, *Angew. Chem. Int. Ed.*, 2021, **60**, 787.
287. S. Krause, J. D. Evans, V. Bon, P. Senkovska, P. Iacomi, F. Kolbe, S. Ehrling, E. Troschke, J. Getzschmann, D. M. Többens, A. Franz, D. Wallacher, P. G. Yot, G. Maurin, E. Brunner, P. L. Llewellyn, F.-X. Coudert and S. Kaskel, *Nat. Commun.*, 2019, **10**, 3632.

288. S. Krause, J. D. Evans, V. Bon, I. Senkovska, S. Ehrling, P. Iacomi, D. M. Többens, D. Wallacher, M. S. Weiss, B. Zheng, P. G. Yot, G. Maurin, P. L. Llewellyn, F.-X. Coudert and S. Kaskel, *Chem. Sci.*, 2020, **11**, 9468.
289. C. Triguero, F.-X. Coudert, A. Boutin, A. H. Fuchs and A. V. Neimark, *J. Phys. Chem. Lett.*, 2011, **2**, 2033.
290. L. Schaper, J. Keupp and R. Schmid, *Front. Chem.*, 2021, **9**, 757680.
291. F.-X. Coudert, M. Jeffroy, A. H. Fuchs, A. Boutin and C. Mellot-Draznieks, *J. Am. Chem. Soc.*, 2008, **130**, 14294.
292. S. M. J. Rogge, R. Goeminne, R. Demuynck, J. J. Gutiérrez-Sevillano, S. Vandenbrande, L. Vanduyfhuys, M. Waroquier, T. Verstraelen and V. Van Speybroeck, *Adv. Theory Simul.*, 2019, **2**, 1800177.
293. R. Goeminne, S. Krause, S. Kaskel, T. Verstraelen and J. D. Evans, *J. Am. Chem. Soc.*, 2021, **143**, 4143.
294. T. D. Bennett and S. Horike, *Nat. Rev. Mater.*, 2018, **3**, 431.
295. M. Erkartal and M. Durandurdu, *ChemistrySelect*, 2018, **3**, 8056.
296. K. Banlusan, E. Antillon and A. Strachan, *J. Phys. Chem. C*, 2015, **119**, 25845.
297. A. C. T. van Duyn, S. Dasgupta, F. Lorant and W. A. Goddard, *J. Phys. Chem. A*, 2001, **105**, 9396.
298. B. Zheng, F. Fu, L. L. Wang, J. Wang, L. Du and H. Du, *J. Phys. Chem. C*, 2018, **122**, 4300.
299. K. Banlusan and A. Strachan, *J. Phys. Chem. C*, 2016, **120**, 12463.
300. R. Pallach, J. Keupp, K. Terlinden, L. Frentzel-Beyme, M. Kloß, A. Machalica, J. Kotschy, S. K. Vasa, P. A. Chater, C. Sternemann, M. T. Wharmby, R. Linser, R. Schmid and S. Henke, *Nat. Commun.*, 2021, **12**, 409.
301. V. I. Hegde, J.-C. Tan, U. V. Waghmare and A. K. Cheetham, *J. Phys. Chem. Lett.*, 2013, **4**, 3377.
302. L. Bouëssel du Bourg, A. U. Ortiz, A. Boutin and F.-X. Coudert, *APL Mater.*, 2014, **2**, 124110.
303. R. N. Widmer, G. I. Lampronti, S. Anzellini, R. Gaillac, S. Farsang, C. Zhou, A. M. Belenguer, C. W. Wilson, H. Palmer, A. K. Kleppe, M. T. Wharmby, X. Yu, S. M. Cohen, S. G. Telfer, S. A. T. Redfern, F.-X. Coudert, S. G. MacLeod and T. D. Bennett, *Nat. Mater.*, 2019, **18**, 370.
304. E. M. Reynolds, E. H. Wolpert, A. R. Overy, L. Mizzi, A. Simonov, J. N. Grima, S. Kaskel and A. L. Goodwin, *Faraday Discuss.*, 2021, **225**, 241.
305. B. B. Shah, T. Kundu and D. Zhao, *Top. Curr. Chem.*, 2019, **377**, 25.
306. F.-X. Coudert, A. H. Fuchs and A. V. Neimark, *Dalton Trans.*, 2016, **10**, 4136.
307. F.-X. Coudert, A. Boutin, A. H. Fuchs and A. V. Neimark, *J. Phys. Chem. Lett.*, 2013, **4**, 3198.
308. J. Wieme and V. Van Speybroeck, *J. Mater. Chem. A*, 2021, **9**, 4898.
309. D. Dubbeldam, A. Torres-Knoop and K. S. Walton, *Mol. Simul.*, 2013, **39**, 1253.
310. G. Steinle-Neumann and R. E. Cohen, *J. Phys.: Condens. Matter*, 2004, **16**, 8783.

311. P. M. Marcus and S. L. Qiu, *J. Phys.: Condens. Matter*, 2004, **16**, 8787.
312. I. T. Todorov, W. Smith, K. Trachenko and M. T. Dove, *J. Mater. Chem.*, 2006, **16**, 1911.
313. S. Plimpton, *J. Comput. Phys.*, 1995, **117**, 1.
314. J. VandeVondele, M. Krack, F. Mohamed, M. Parrinello, T. Chassaing and J. Hutter, *Comput. Phys. Commun.*, 2005, **167**, 103.